Atmospheric neutrino@INO

By

Anushree Ghosh

Enrolment Number : PHYS01200804029

Bhabha Atomic Research Centre, Mumbai

A thesis submitted to the

Board of Studies in Physical Sciences

In partial fulfillment of requirements

For the degree of

DOCTOR OF PHILOSOPHY

of

HOMI BHABHA NATIONAL INSTITUTE

September, 2014

STATEMENT BY AUTHOR

This dissertation has been submitted in partial fulfillment of requirements for an advanced degree at Homi Bhabha National Institute (HBNI) and is deposited in the Library to be made available to borrowers under rules of the HBNI.

Brief quotations from this dissertation are allowable without special permission, provided that accurate acknowledgement of source is made. Requests for permission for extended quotation from or reproduction of this manuscript in whole or in part may be granted by the Competent Authority of HBNI when in his or her judgement the proposed use of the material is in the interests of scholarship. In all other instances, however, permission must be obtained from the author.

Anushree Ghosh

Declaration

I, hereby declare that the investigation presented in the thesis has been carried out by me. The work is original and has not been submitted earlier as a whole or in part for a degree/diploma at this or any other Institution/University.

Anushree Ghosh

List of publication arising from thesis

journal

1. M. M. Devi, A. Ghosh, D. Kaur, L. S. Mohan, S. Choubey, A. Dighe, D. Indumathi, S. Kumar, M. V. N. Murthy, Md. Naimuddin, *Hadron energy response of the ICAL detector at INO,* JINST 8 (2013) **P11003**

2. Anushree Ghosh, Tarak Thakore, Sandhya Choubey, *Determining the Neutrino Mass Hierarchy with INO, T2K, NOvA and Reactor Experiments,* JHEP **1304**, (2013), 009

3. Anushree Ghosh, Sandhya Choubey, *Measuring the Mass Hierarchy with Muon and Hadron Events in Atmospheric Neutrino Experiments,* JHEP **1310, (2013), 174**

4. Tarak Thakore, Anushree Ghosh, Sandhya Choubey, Amol Dighe, *The Reach of INO for Atmospheric Neutrino Oscillation Parameters,* JHEP **1305**, (2013), 058

List of other publications of candidate not related to this thesis

1. Sandhya Choubey, Anushree Ghosh, *Determining the Octant of* θ_{23} *with PINGU, T2K, NOvA and Reactor Data,* JHEP **1311, (2013), 166**

2. Moon Moon Devi, Anushree Ghosh, Daljit Kaur, Laksmi Mohan, *Hadron energy resolution as a function of iron plate thickness at ICAL*, (arXiv:1401.2779 [physics.ins-det])(accepted in JINST)

Anushree Ghosh

Dedicated to

My Family

ACKNOWLEDGEMENTS

During the writing of this thesis, I realized more and more that nothing could have been done if not for the assistance, patience, and support of many wonderful people around me. This page is meant for them. Firstly, I would like to thank my supervisor, Dr. Sandhya Choubey: thanks a lot Sandhyadi for your continuous support and patience towards me throughout my PhD life. Working with you has been a great pleasure really. I would like to express my deepest gratitude to Amol Dighe and Prof. Murthy, Prof. Raj Gandhi, Prof. Indumathi, Prof Gobinda Majumdar, Prof. Vivek Datar.,Prof. Sreerup Roy Choudhuri, Dr. Satyanarayana, Prof. Vandana Nanal and Prof. Pilley. for their contribution in my journey till now starting from the graduate training period at TIFR. I would like to express my gratitude to Prof. Naba Kumar Mondal, the spokesperson of the India-Based Neutrino Observatory who gave me the opportunity to work here. I would also like to thank my other collaborators Thanks to Tarak Thakore, Moon Moon, Lakshmi and Daljit for sharing many ideas and the workloads. Also, a big thanks to all of you, who made the two INO weekly meetings a big successful one by your enthusiastic participation. I would like to thank all my friends who make my PhD life so much enjoyble. I am really grateful to all of you: Sudeshna, Sumanta, Vivek, Samuel, Nitali, Sanmoy, Mintu, Akansha, Shrobona, Archana, Manimaladi, Niyogi, Bhuru, Hochi, Rambha, Jonthu, Tarat, Paramita, Anirban da, Atri da, Animesh, Shankha, Deepak, Sudipto, Arnab, Ushoshi, Monalisa for making that time a wonderful and memorable one. Thanks to all the non-academic staff of HRI, TIFR, INO, who are giving their best. I thank my parents, didi and dada for their faith in me and allowing me to be as ambitious as I wanted. Last but not least, I would like to convey my heartfelt gratitude and love to my husband Manoj for putting up with me all the time. Thanks Monjo, for your immense love and support.

CONTENTS

CHAPTER 1

SYNOPSIS

Neutrino physics is a powerful tool for digging out the physics beyond the standard model (BSM) as neutrino oscillation is a strong proof of neutrino having mass which is a hint of BSM. The neutrino mixing matrix, can be parameterized in term of three mixing angles θ_{12}, θ_{23} and θ_{13} and charge parity violating phase δ_{cp}. The frequency of the neutrino oscillation is governed by two mass square differences Δm^2_{21} and Δm^2_{31}. Among the six oscillation parameters the solar experiments have already identified the value of θ_{12} and Δm^2_{21} with a very good accuracy. Super Kamiokande and other accelerator based neutrino experiments have measured $|\Delta m^2_{31}|$ and $\sin^2 2\theta_{23}$ with good certainty. The reactor experiments DayaBay, RENO, DoubleChooz recently published their result in measuring the third mixing angle θ_{13} and confirmed the non-zero value of θ_{13} which was earlier indicated by accelerator based experiment T2K and MINOS. There are another two parameters which are still unknown and their discovery are the prime concern of the ongoing and future experiments. These two are the CP violating phase δ_{CP} and sign of Δm^2_{31}. Determining the sign of Δm^2_{31} is crucially important for reconstructing the correct mass ordering of neutrino. The current discovery of non-zero θ_{13} strengthens the possibility of discovering the true hierarchy of neutrino masses via matter effect. It has also opened up the possibility of probing the CP violation in the neutrino sector using electron appearance channel.

I have done my research work under India-based Neutrino Observatory (INO) graduate training programme. INO is a future neutrino experiment which will use atmospheric neutrino as source. The proposed detector ICAL, having 50 kton mass, will consist of a stack of 150 horizontal layers of 5.6 cm thick magnetized iron plates interleaved with 2.5 cm gaps to house the Resistive plate chambers (RPC) as active detector. The readout of the RPCs will be performed by external orthogonal pickup strips (X and Y strips). Being magnetized , ICAL will have charge identification capability and it will be very helpful in determining the true mass ordering of neutrino using the earth matter effect. Apart from determining the true mass hierarchy, INO has set the precise measurement of $|\Delta m^2_{31}|$ and $\sin^2 2\theta_{23}$ and the determination of true octant of θ_{23} as its major goal.

Atmospheric muon neutrinos (antineutrinos) interact with the iron target in the detector through quasi-elastic (QE), resonance (RS) and deep inelastic scattering (DIS) processes. In case of charged current interaction, muon is produced associated with hadrons. Muon gives clear track inside the detector as muon interacts with matter very little. Hadrons interact with the matter via strong force and produce a shower. Muon momentum can be reconstructed either from the tracklength of the muon or from the curvature of the muon track, as the detector is magnetized. Sizable amount of hadron energy is absorbed into the iron plates and rest of the energy is deposited as visible energy to RPCs in form of the hits. We calibrate the energy of the hadrons from the hit distribution of hadrons in the detector. The reconstructed neutrino energy is given by the sum of the muon and hadron shower energy measurements.

My works was focused on finding out the energy resolution of hadrons shower of ICAL as well as the physics reach of ICAL detector.

We investigated the behaviour of hadrons inside ICAL in a collaborative work where I was involved in finding the hadron energy resolution for ICAL. Geant4 is used as simulation tool and ROOT is used for analyzing the results. Sizable amount of hadron energy is absorbed into the iron plates and rest of the energy deposited as visible energy to RPCs in form of hits. Geant4 gives the raw hit information of hadron shower which are digitized in terms of hits in x strips and hits in y strips of the RPC. π^+, π^-, π^0, K^+, K^-, K^0 are thrown individually in ICAL detector with certain energy and it is found that ICAL can not distinguish among the different type of hadrons. I did the Geant4 Monte Carlo simulation using π^+ and π^- only. I fitted The hit distribution for each energy with Gaussian distribution and hit versus energy calibration curve is obtained. Using the hit vs energy calibration curve, the energy resolution of ICAL for π^+ and for π^- is calculated.

We analyzed mainly the potential of ICAL for probing the true mass hierarchy of neutrino and the ways to improve the mass hierarchy sensitivity of any atmospheric experiment.

ICAL having the charge identification capability and using atmospheric neutrino as a source has potential to determine the true mass hierarchy depending on the fact that the event rate will be different for neutrinos and antineutrinos due to the matter effect. I studied the mass hierarchy sensitivity in great detail using final state muon events. We also studied the capability of ICAL to determine precisely the oscillation parameters as well as the true octant of θ_{23}. A code is developed written in C++ for the physics analysis of ICAL which takes the unoscillated events generated by any neutrino generator as input and calculates the χ^2 which is the measure of the sensitivity of the detector taking care of the realistic detector response. NUANCE, duly modified for INO, has been used as Monte Carlo generator for generating atmospheric neutrino events and HONDA atmospheric flux is used as input to the generator. In order to reduce the Monte Carlo fluctuations in event sample, events were generated corresponding to 50×1000 kton-years exposure. Since, it takes fairly long to run the Nuance code to generate such a large event sample, running it over and over again for each set of oscillation parameter is practically impossible. Therefore, we ran the event generator only once for no oscillations and thereafter impose the reweighting algorithm to generate the event sample for any set of oscillation parameters. The data sample, after incorporating the oscillations, folded with detector efficiencies and resolution functions, given by INO collaboration, to simulate the reconstructed muon events in ICAL. The events are finally normalized to a realistic number of years of running of ICAL using which the spectral analysis of the χ^2 was performed taking care of both statistical errors and systematic errors. In order to perform the statistical analysis for mass hierarchy measurement, we generated the data at the benchmark true values for oscillation parameters, and assuming a certain neutrino mass hierarchy. we fitted this simulated data with the wrong mass hierarchy to check the statistical significance with which this wrong hierarchy can be disfavoured. We assumed Poissonian distribution for the errors in this definition of χ^2. We showed the mass hierarchy sensitivity results with only ICAL data for the analysis with fixed values of the oscillation parameters in the fit, as well as that obtained after marginalization over the oscillation parameters $|\delta m^2_{eff}|$, $\sin^2\theta_{23}$ and $\sin^2 2\theta_{13}$ in their current 3σ ranges. We showed these results as a function of the exposure in ICAL. From comparison of two results, we showed that the mass hierarchy sensitivity with ICAL data deteriorates with the uncertainty in the measured value the $|\delta m^2_{eff}|$, $\sin^2\theta_{23}$ and $\sin^2 2\theta_{13}$. These parameters will be very accurately determined by the T2K, NOνA Double Chooz, RENO and Daya Bay experiments. Since INO is expected to start operation after each one of these have finished their full projected run, it is meaningful to include the effect of these experiments in a combined statistical analysis for the neutrino mass hierarchy. In order to take that into account, we simulated the data for these experiments using GLoBES with the experimental specifications mentioned in their respective letter of intent and/or DPR. The results on mass hierarchy sensitivity from the combined analysis of data from ICAL@INO along with that from T2K, NOνA, Double Chooz, RENO and Daya Bay was shown for benchmark values of the oscillation parameters and full marginalization over all oscillation parameters in the fit for the wrong mass hierarchy. We showed that marginalization over δ_{CP} is practically unessential for the ICAL@INO data. However, for the accelerator data it is absolutely crucial to marginalize over δ_{CP} due to the very strong dependence of the hierarchy dependence on this parameter in these experiments. We then generated the data at all values of δ_{CP}(true) and showed that the mass hierarchy sensitivity of ICAL@INO was independent of δ_{CP}(true), however, the sensitivity of the combined NOνA, T2K and the reactor experiments depends very strongly on what δ_{CP}(true) has been chosen by Nature. For $\sin^2\theta_{23}$(true) $= 0.5$ and $\sin^2 2\theta_{13} = 0.1$ the combined data of 10 years exposure in ICAL@INO along with T2K, NOνA and reactor experiments could rule out the wrong hierarchy with a statistical significance of 3σ to 4.2σ, depending on the chosen value of δ_{CP}(true). We also studied the effect of $\sin^2 2\theta_{13}$(true) and $\sin^2\theta_{23}$(true) on the reach of these combined projected data sets to determining the neutrino mass hierarchy. For δ_{CP}(true) $= 0$, we showed that the statistical significance with which the wrong hierarchy could be ruled out by the global data set of 10 years exposure in ICAL@INO along with T2K, NOνA and reactor experiments, could be anywhere between 2.13σ to 4.5σ depending on $\sin^2\theta_{23}$(true) and $\sin^2 2\theta_{13}$, where we allowed $\sin^2\theta_{23}$(true) to vary between $[0.4-0.6]$ and $\sin^2 2\theta_{13}$(true) between $[0.08-0.12]$. For the most conducive choice of δ_{CP}(true) $\simeq 270^\circ$ the sensitivity could go up to greater than 5σ with 10 years of ICAL@INO combined with data from T2K, NOνA and reactor experiments.

Next, we concentrated on improving the potential of atmospheric experiment in mass hierarchy measurement. At first we investigated the factors, due to which the mass hierarchy sensitivity goes down, such as (i) due to the inclusion of appearance channel (ii) due to the averaging effect of the charge current interaction which produces muons with any energy and angle allowed by the process, and (iii) with the inclusion of detector resolutions. We showed how the mass hierarchy effect in muon events sample, hadron event sample as well as the neutrino event sample decreases for inclusion of these factors one by one. In case of the muon and hadron event spectrum, the major smearing of the earth matter effects come from the cross section effect. The energy resolution brings about a further reduction in the signal, however the effect is mild. We showed that Despite this reduction in the earth matter effects, both the muons as well as the hadrons event spectra have mass hierarchy sensitivity, which survives even after including all the resolution functions. The neutrino analysis is affected only due to the appearance channel and the detector resolutions. It was shown that the hierarchy effects reduce sharply as the neutrino energy and angular resolution are switched on, such that the net earth matter effect present in the neutrino spectrum becomes comparable to that in the muon spectrum.

We performed a χ^2 analysis to quantify the reach of the experiment to measuring the neutrino mass hierarchy. We showed results for three different analysis. First, we did the analysis using only muon events.Since the zenith angle resolution given by INO collaboration is already very good, we fixed the zenith angle resolution for the muons at $\sigma_{\Theta_\mu} = 0.01$ in $\cos\Theta_\mu$ and showed how the mass hierarchy sensitivity could be improved by improving the energy resolution and reconstruction efficiency of muon. If the muon energy resolution could be improved to 2%, we could get a more than 4σ measurement of the mass hierarchy from the 50×10 kton-year of muon data alone. Next, we included the hadron events as additional input in the analysis along with muon data. Since the detector is not expected to measure the hadron energy and angle as well as it can do fro muon and since we wanted to keep track of the particles coming from a given neutrino and zenith angle, we the tagged hadron with their corresponding muon produced in the charge current interaction of the neutrino. We collected all the hadrons in a given zenith angle bin and then binned in their energy and hadron angle. We defined a χ^2 function for the combined analysis of the hadron and muon events with the binned including muon and hadron data. The results showed that the hadron events bring in a noticeable improvement in the final sensitivity of the experiment to the neutrino mass hierarchy by increasing the $\Delta\chi^2$ by upto 5. The combined muon and hadron analysis is projected to give a 4.5σ from a 50×10 kton-year exposure, if one could achieve 2% energy resolution and 80% reconstruction efficiency in the muons. Finally I showed the mass hierarchy sensitivity expected from the analysis of the data in terms of the neutrino energy and angle.

We also found out the potential of ICAL in measuring the $|\Delta m^2_{31}|$ and $\sin^2 2\theta_{23}$ precisely and also determining the true octant of θ_{23}. We presented uncorrelated as well as correlated constraints on the value of $\sin^2 2\theta_{23}$ and Δm^2_{32} expected to be obtained after 10 years of running of the 50 kton ICAL. We found that the values of $\sin^2 2\theta_{23}$ and Δm^2_{32} may be determined at an accuracy of 17% and 5.1% respectively. The sensitivities with the data at ICAL only are not expected to be better than what we already have, indeed some of the other experiments in the next decade may do much better. However the measurement at ICAL will be complementary and may be expected to contribute significantly towards the precision of parameters in a global fit. As far as the sensitivity to the θ_{23} octant and its deviation from maximality is concerned, we found that 10 years of ICAL can exclude maximal mixing or the θ_{23} value in the other octant to ¡ 95% C.L. only if the actual θ_{23} is in the first octant and close to the current 3σ lower bound to 99% C.L.. Indeed, the octant identification seem to be beyond the reach of any single experiment in the next decade.

LIST OF FIGURES

LIST OF TABLES

CHAPTER 1

INTRODUCTION

Neutrinos are one of the most abundant particles in the Universe. They, however, are very difficult to observe. They have no electric charge and interact only via the weak force thereby rarely interacting with matter. The consequence is significant. If a neutrino is produced, it travels straight through any matter as if it is travelling in the vacuum.

The concept of neutrino was first postulated in 1930 by Wolfgang Pauli to explain the apparent violation of conservation of energy and momentum in beta decay which was most easily avoided by postulating another particle. Enrico Fermi called the particle a neutrino and developed a theory of beta decay based on it, but it was not experimentally observed until 1956. In 1956, two American scientists, Frederick Reines and Clyde Cowan, reported the first evidence of electron neutrinos using a fission reactor as a source of neutrinos and a well-shielded scintillator detector nearby to detect them. The next discovery was of muon neutrino which was found by Leon Lederman, Mel Schwartz, and Jack Steinberger, scientists at CERN by firing a GeV proton beam through a target thus producing pions, muons, and muon neutrinos. The existence of the third flavour of neutrino, the tau neutrino, was first inferred in 1978 with the discovery of the tau particle at SLAC, the Stanford Linear Accelerator Center. They realized that the tau particle was just a heavier version of the electron and muon and therefore should have a corresponding neutrino as well. In 2000, the scientists at FNAL on the DONUT detector were finally able observe a tau neutrino.

It has been a long standing mystery whether neutrinos have exactly vanishing masses, or only very small, but finite, masses. In standard model, neutrino is defined as massless particle. However, there is strong evidence which suggest that neutrinos undergo transformations between flavours, a quantum mechanical phenomenon known as ”neutrino oscillations” which require neutrinos to be massive. The first idea of neutrino oscillations was put forward by B. Pontecorvo in 1957-58 [1, 2]. The first indication of neutrino oscillation came from solar neutrino experiments [3, 4, 5] which observed ν_e flux quite below the expected value. Finally, in 1998 the Super-Kamiokande (SK) [6] experiment in Japan observed oscillations of atmospheric neutrinos, and later in 2000, Sudbury Neutrino Observatory (SNO) [7] in Canada showed that the missing solar ν_e have indeed oscillated into other flavours. Also, a series of outstanding results from other oscillation experiments e.g., reactor [9, 10, 11, 12] and accelerator [13, 15, 16] along with solar and atmospheric experiments, have established Neutrino flavour oscillations beyond any doubt. Since, neutrino flavour oscillations require neutrinos to be massive and mixed, they have thus provided the first unambiguous hint for physics beyond the standard model of elementary particles.

1.1 Source of neutrinos

To observe neutrino oscillation one needs copious amount of neutrinos as a source and large neutrino detectors for their detection. In this section, different sources of neutrinos are described which are used or are going to be used in future for studying neutrino oscillation:

- ***Atmospheric neutrinos:*** Atmospheric neutrinos are created by the interactions of primary cosmic rays with the nuclei in the atmosphere. The primary cosmic rays are mainly composed of protons, with a small component of heavier nuclei. The interactions of these primary cosmic rays with the nuclei in the atmosphere generate secondary cosmic rays, which include all the hadrons and their decay products, with an energy spectrum extended to higher energy with an approximate power law. In particular, many secondary pions are produced. these pions decay mainly into muons and muon neutrinos:

$$\pi^+ \to \mu^+ + \nu_\mu; \qquad \pi^- \to \mu^- + \bar{\nu}_\mu \tag{1.1}$$

At high energies, also kaons contribute to the production of neutrinos and muons. The muons which decay before hitting the ground generate electrons, electron neutrinos, and muon neutrinos through the processes

$$\mu^+ \to e^+ + \nu_e + \bar{\nu}_\mu; \qquad \mu^- \to e^- + \bar{\nu}_e + \nu_\mu \tag{1.2}$$

The neutrinos generated in these reactions are called atmospheric neutrinos. From the above equation, it is evident that, roughly twice as many muon-type neutrinos (and anti-neutrinos) are produced as electron type ones.

Atmospheric neutrino flux peaks at zenith angles $\Theta_z \sim \pm 90^0$, i.e., near the horizon, due to the larger length of atmosphere available in this direction. While the low energy (E $\leq$ 1 GeV) neutrinos have a complicated (Θ_z,ϕ) dependence due to various causes including the Earth's magnetic field, they are roughly ϕ-independent at higher energies. The atmospheric neutrino flux peaks just below a GeV and falls thereafter steeply as $E^{-2.7}$.

Atmospheric neutrinos can be detected in underground laboratories through scattering on nuclei. The detectors must be underground in order to provide good shielding from the flux of secondary cosmic ray muons, whose frequent interactions would otherwise overwhelm the detector.

- ***Solar neutrinos:*** Solar neutrinos are electron neutrinos produced in the sun via the thermonuclear reactions which generate the solar energy. The Sun is powered by the fusion of four protons into a 4-Helium nucleus, with the production of two neutrinos. The pp chain and the CNO cycle are the two main mechanisms for this process. The pp chain accounts for $\sim 99\%$ of the energy production in the sun and, therefore, produces the largest flux of neutrinos.

- ***Astrophysical source of neutrinos:*** Neutrinos of very high energies are produced by astrophysical sources like gamma ray bursts (GRB) and active galactic nuclei (AGN) jets. Charged pions, generated by reaction with ambient photons (pγ reactions) and protons within the source, (pp reactions) decay to give muons and muon neutrinos. The muons further decay to give electron and muon neutrinos. In most models, the ratio of electron neutrinos to muon neutrinos is 1:2 and that of muon anti-neutrinos to muon neutrinos is 1:1, while the electron anti-neutrino to electron neutrino ratio is 0 for pγ reactions and 1:1 for pp reactions. These neutrinos can have energies upto the order of PeV (10^6 TeV), and are thus known as ultra high-energy (UHE) neutrinos. Also, neutrinos may be produced in neutrino bursts in supernovae.

- ***Accelerator Neutrino beams:*** Accelerator based neutrino beams are essentially beams of ν_μ with small (less than 1 %) contamination of other flavours. To produce accelerator based neutrino beams, a beam of high energy protons is directed to a thick nuclear target, producing secondaries such as positively charged pions and kaons which are collected, focussed and allowed to decay in a long decay pipe. After this decay, a reasonably collimated muon neutrino beam is obtained. A muon anti-neutrino beam can be obtained by collecting negatively charged mesons rather than positively charged mesons. Fluxes of neutrino beams are parametrized in terms of number of protons on target (POT) per year.

- ***β beams:*** β beams is the ν_e or $\bar{\nu}_e$ beam. The concept of β beams involves producing a large number of β-unstable ions, accelerating them to some reference energy, and allowing them to decay in the straight section of a storage ring, resulting in a very intense and pure ν_e or $\bar{\nu}_e$ beam.

- ***Neutrino factories:*** These are based on muon storage rings where it will be possible to capture roughly 10^{21} muons (of either sign) per year. A muon storage ring has a racing track design with long, parallel, straight sections connected at the end by semi-circular sections. Beams of high energy accelerated muons (E $>$ 20 GeV) circulate in the storage ring and can be made to decay in the straight sections. These decays produce a well collimated and intense neutrino beam. The composition and spectra of intense neutrino beams will be determined by the charge, momentum and polarization of the stored muons. The beam consists of ν_μ and $\bar{\nu_e}$ if the ring contains μ^-, and it consists of $\bar{\nu_\mu}$ and ν_e if the ring contains μ^+.

- ***Reactor Neutrinos:*** Neutrinos may also be produced by nuclear reactors. Fission reactors are prodigious producers of neutrinos (about 10^{20} ν_e s^{-1} per nuclear core). The fissioning of ^{235}U produces elements which must shed neutrons to approach the line of stability. The beta decays of this excess produce approximately six electron antineutrinos per fission with the energies $\sim$ MeV.

1.2 Neutrino oscillation experiments

A range of neutrino experiments are currently ongoing to study the neutrino oscillations. There are also a certain number of potential future experiments which will be functional in the coming years. Some of them are discussed below:

- ***Super-KamioKande:*** The Super-Kamiokande (SK) experiment [17] is a large ring imaging Cherenkov detector, located 1,000 m (2,700 mwe) underground, inside an old zinc mine in Mount Ikenoyama in Kamioka, Japan. SK has performed analyses on atmospheric, solar and accelerator neutrinos, as well as searches for supernova neutrinos, proton decay and other exotic particles. The construction of SK was started in 1991 and the observation began on April 1, 1996.

- ***SNO:*** The Sudbury Neutrino Observatory (SNO) [7] was a heavy-water Cherenkov detector designed to detect solar neutrinos, and to study neutrino oscillations. The SNO detector was located 6,800 feet (about 2 km) underground in Vales Creighton mine near Sudbury, Ontario, Canada. The detector was turned on in May 1999, and was turned off on 28 November 2006.

- ***MINOS:*** The Main Injector Neutrino Oscillation Search (MINOS) [18] is a long-baseline neutrino oscillation experiment which uses two functionally identical neutrino detectors. MINOS near detector is located at Fermilab, $\sim$ 1km away from the source of the neutrinos, and the MINOS far detector is located 735 km away at the Soudan Underground Laboratory in Soudan, Minnesota. The neutrinos at the Main Injector (NuMI) facility at Fermi National Accelerator Laboratory (FNAL, Fermilab) supplies a beam of neutrinos to the MINOS experiment. The MINOS experiment has started detecting neutrinos from the NuMI beam in February 2005.

- ***T2K:*** The T2K experiment [19] is the first off-axis long-baseline neutrino oscillation experiment. In the T2K experiment a 2.5° off-axis neutrino beam is sent from the J-PARC accelerator facility at Tokai to the Super-Kamiokande detector at Kamioka at a distance of 295 km. The fiducial mass of Super-Kamiokande is 22.5 kton and there is a near detector ND280 at a distance of 280 m from the beam target.

- ***NOνA:*** NuMI Off-Axis ν_e Appearance Experiment (NOνA) [20] is a two-detector neutrino oscillation experiment which is optimized for ν_e identification. The NOνA experiment will shoot a 3.3° off-axis (anti)neutrino beam from NuMI at Fermilab to the 14 kton totally Active Scintillator Detector (TASD) located in Northern Minnesota at a distance of 810 km. The near detector at Fermilab is a 200 ton detector similar to the far detector.

- ***Double Chooz:*** The Double Chooz reactor experiment [21] has a liquid scintillator detector with fiducial mass of 8.3 tons placed at a distance of 1 km and 1.1 km from the two reactor cores of the Chooz reactor power plant, each with 4.27 GW$_{th}$ thermal power. Double Chooz has been taking data with just this far detector. In addition to the far detector, this experiment will also have a near detector which will be identical to the far detector and will be placed at a distance of 470 m and 350 m respectively from the two reactor cores.

- ***RENO:*** The RENO (Reactor Experiment for Neutrino Oscillations) is short baseline reactor antineutrino experiment [22], powered by the Yonggwang reactor plant in South Korea, with a total reactor power of 16.4 GW$_{th}$, making it currently the most powerful reactor in the world behind the Kashiwazaki-Kariwa power plant in Japan (which is currently shut down). This reactor complex has six reactor cores with first two having power 2.6 GW$_{th}$ while the last four with power 2.8 GW$_{th}$, respectively. These reactor cores are arranged along a 1.5 km straight line separated from each other by equal distances. The near detector of this experiment has a fiducial mass of 15 ton and is situated at a distance of 669 m, 453 m, 307 m, 338 m, 515 m and 74 m respectively from the reactor cores. The far detector also has a fiducial mass of 15 tons and is placed in the opposite direction at a distance of 1.557 km, 1.457 km, 1.396 km, 1.382 km, 1.414 km and 1.491 km respectively from the reactor cores.

- ***DayaBay:*** The Daya Bay reactor experiment [23] observes antineutrinos from the Daya Bay and Ling Ao I and Ling Ao II reactors. Each of them have two reactor cores with a total combined power of 17.4 GW$_{th}$. This experiment, after fully constructed, will have 4 near detectors each with 20 ton fiducial mass and 4 far detectors also with fiducial mass 20 ton each. The far detectors will be at a distance of 1.985 km, 1.613 km and 1.618 km from Daya Bay, Ling Ao and Ling Ao II reactors respectively. The distance of the near detectors from each of the reactor cores are more complicated, and can be found in [23]. The experiment has been running with 6 detectors.

1.3 Neutrino oscillation

Neutrino oscillation arises from a mixture between the flavour and mass eigenstates of neutrinos. The neutrino flavour eigen states $|\nu_\alpha\rangle(\alpha = e, \mu, \tau)$ that couple to the weak force, can be expressed as a linear combination of the mass eigenstate $|\nu_j\rangle(j = 1,2,3)$:

$$|\nu_\alpha\rangle = \sum_{j=1,2,3} U^*_{\alpha j}|\nu_j\rangle\,, \tag{1.3}$$

where U is a 3×3 unitary mixing matrix known as the PMNS matrix [24, 25]. Thus $U^\dagger = U^{-1}$. Assuming that at a time t = 0, the flavour eigenstate $|\nu_\alpha\rangle$ was produced, the initial state at t=0 can be written as

$$|\nu(0)\rangle = |\nu_\alpha\rangle = \sum_j U^*_{\alpha j}|\nu_j\rangle \tag{1.4}$$

and then the neutrino state at time t is given by

$$|\nu(t)\rangle = |\nu_\alpha\rangle = \sum_j U^*_{\alpha j} e^{-iE_j t}|\nu_j\rangle\,. \tag{1.5}$$

Then, the probability amplitude to find the neutrino in a state $|\nu_\beta\rangle$ at a later time t can be calculated as:

$$\begin{aligned} A(\nu_\alpha \nu_\beta;t) = \langle \nu_\beta | \nu(t) \rangle = \sum_j U^*_{\alpha j} e^{-iE_j t} \langle \nu_\beta | \nu_j \rangle \\ = \sum_j \sum_i U_{\beta i} U_{\alpha j} e^{-iE_j t} \langle \nu_i | \nu_j \rangle = \sum_j U_{\beta j} e^{-iE_j t} U^*_{\alpha j}. \end{aligned} \tag{1.6}$$

The neutrino oscillation probability, i.e., the probability of the transformation of a flavour eigenstate neutrino ν_α into another one ν_β , is then

$$P(\nu_\alpha \to \nu_\beta;t) = |A(\nu_\alpha \to \nu_\beta;t)|^2 = |U_{\beta j} e^{-iE_j t} U_{\alpha j}|^2 \tag{1.7}$$

The above discussion is based on assumption that neutrinos are Dirac particle. However, neutrino oscillation can not distinguish between Dirac and Majorana neutrinos simply because total lepton number is not violated here. The oscillation probabilities of the channels with $\alpha \neq \beta$ are usually called transition probabilities, whereas the oscillation probabilities of the channels with $\alpha = \beta$ are usually called survival probabilities.

1.3.1 Neutrino Oscillation in vacuum

Two flavour case

At first we consider the two flavour mixing case which is more simple than the full three generation. Let ν_α, ν_β be the flavour eigenstates and ν_1 , ν_2 be the mass eigenstates with masses m_1 and m_2, respectively. In the two flavour scenario, the mixing matrix U assumes the form of an orthogonal transformation in two dimensions :

$$U = \begin{pmatrix} \cos\theta & \sin\theta \\ -\sin\theta & \cos\theta \end{pmatrix}, \tag{1.8}$$

where θ is the mixing angle.

It should be noted that in an interaction, neutrinos are always produced as flavour eigenstates, but the evolution is in terms of their mass eigenstates. The standard evolution equation in vacuum is given by

$$i\frac{d}{dt}\begin{pmatrix}\nu_1(t)\\ \nu_2(t)\end{pmatrix} = H_0\begin{pmatrix}\nu_1(t)\\ \nu_2(t)\end{pmatrix}, \tag{1.9}$$

where H_0 is the free particle Hamiltonian:

$$H_0 = \begin{pmatrix}E_1 & 0\\ 0 & E_2\end{pmatrix}. \tag{1.10}$$

E_1 and E_2 are the energies corresponding to the two mass states m_1 and m_2. Assuming neutrino masses to be small compared to the neutrino energy, we have E_i as:

$$E_i = \sqrt{p_i^2 + m_i^2} \simeq p + \frac{m_i^2}{2E}, \tag{1.11}$$

where p is the neutrino momentum. Then Eq. 1.10 becomes:

$$H_0 = \begin{pmatrix}\frac{m_1^2}{2E} & 0\\ 0 & \frac{m_2^2}{2E}\end{pmatrix}. \tag{1.12}$$

Using the relation between flavour and mass eigenstates, the evolution equation in flavour basis is:

$$i\frac{d}{dt}\begin{pmatrix}\nu_\alpha(t)\\ \nu_\beta(t)\end{pmatrix} = H_f\begin{pmatrix}\nu_\alpha(t)\\ \nu_\beta(t)\end{pmatrix}, \tag{1.13}$$

The Hamiltonian H_f in flavour basis can be computed to be:

$$H_f = UH_0U^\dagger = \begin{pmatrix} (E+\frac{m_1^2+m_2^2}{4E}) - \frac{\Delta m^2}{4E}\cos 2\theta & \frac{\Delta m^2}{4E}\sin 2\theta \\ \frac{\Delta m^2}{4E}\sin 2\theta & (E+\frac{m_1^2+m_2^2}{4E}) + \frac{\Delta m^2}{4E}\cos 2\theta \end{pmatrix}, \tag{1.14}$$

where $\Delta m^2 = m_2^2 - m_1^2$. The expressions in the brackets in the diagonal elements of the effective Hamiltonian in Eq. (1.14) coincide and they can only modify the common phase of the neutrino states and therefore have no effect on neutrino oscillations which depend on the phase differences. So, these terms can be omitted. Then Eq. (1.14 then takes the form:

$$H_f = UH_0U^\dagger = \frac{\Delta m^2}{4E}\begin{pmatrix} -\cos 2\theta & \sin 2\theta \\ \sin 2\theta & \cos 2\theta \end{pmatrix}, \tag{1.15}$$

Thus, using the Eq. (1.35), the probability of finding the other flavour, referred as appearance probability, in two flavour oscillation in vacuum, is:

$$P(\nu_\alpha \to \nu_\beta) = \sin^2 2\theta \sin^2 \frac{\Delta m^2 L}{4E} \tag{1.16}$$

where time t $\simeq$ L, neutrino flight length and the probability of finding the original flavour, referred as survival probability, in two flavour oscillation in vacuum, is:

$$P(\nu_\alpha \to \nu_\alpha) = 1 - \sin^2 2\theta \sin^2 \frac{\Delta m^2 L}{4E} \tag{1.17}$$

$$= 1 - \sin^2 2\theta \sin^2 \frac{1.27\Delta m^2(eV^2)L(\mathrm{Km})}{E(\mathrm{GeV})}. \tag{1.18}$$

Equation Eq. (1.18) and Eq. (1.16), clearly shows that the oscillation probability is characterized by the mixing angle, the mass squared difference Δm^2_{ij}, the neutrino flight length L and the neutrino energy E. The first term in Eq. (1.16) ($\sin^2 2\theta$) describes the amplitude (or depth) of the neutrino oscillations. The second term oscillates with time or distance L, travelled by neutrinos. The phase of the sine (the oscillation phase) is proportional to the energy difference of the mass eigenstates $\frac{\Delta m^2}{E}$ and to the distance L.

Three flavour case

In a system with three neutrino flavours, mixing becomes more complicated. A general unitary n × n mixing matrix of Dirac particles can be parametrized by n(n -1)/2 rotation angles and n(n + 1)/2 complex phase factors, of which (2n -1) can be absorbed into a redefinition of the particle fields. For the 3 × 3 case, we thus have three mixing angles θ_{23}, θ_{13}, θ_{12} and one complex phase δ which is responsible for CP violation in the neutrino sector. Hence, the three flavour PMNS matrix U can be parameterized as follows:

$$U = \begin{pmatrix} 1 & 0 & 0 \\ 0 & c_{23} & s_{23} \\ 0 & -s_{23} & c_{23} \end{pmatrix} \begin{pmatrix} c_{13} & 0 & s_{13}e^{-i\delta} \\ 0 & 1 & 0 \\ -s_{13}e^{i\delta} & 0 & c_{13} \end{pmatrix} \begin{pmatrix} c_{12} & s_{12} & 0 \\ -s_{12} & c_{12} & 0 \\ 0 & 0 & 1 \end{pmatrix} \tag{1.19}$$

$$= \begin{pmatrix} c_{12}c_{13} & s_{12}c_{13} & s_{13}e^{-i\delta} \\ -s_{12}c_{23} - c_{12}s_{23}s_{13}e^{i\delta} & c_{12}c_{23} - s_{12}s_{23}s_{13}e^{i\delta} & s_{23}c_{13} \\ s_{12}s_{23} - c_{12}c_{23}s_{13}e^{i\delta} & -c_{12}s_{23} - s_{12}c_{23}s_{13}e^{i\delta} & c_{23}c_{13} \end{pmatrix}, \tag{1.20}$$

where $c_{ij} \equiv \cos\theta_{ij}$, $s_{ij} \equiv \sin\theta_{ij}$. The oscillation probability can be calculated using Eq. (1.35) and may be written in the form:

$$\begin{aligned} P(\nu_\alpha \rightarrow \nu_\beta) = \delta_{\alpha\beta} - 4\sum_{i>j} Re[U^*_{\alpha i}U_{\beta i}U_{\alpha j}U^*_{\beta j}] \sin^2\left(\frac{\Delta m^2_{ij}L}{4E}\right) \\ +2\sum_{i>j} Im[U^*_{\alpha i}U_{\beta i}U_{\alpha j}U^*_{\beta j}] \sin\left(\frac{\Delta m^2_{ij}L}{2E}\right) \end{aligned} \tag{1.21}$$

. Unlike in the two-flavour case, they in general do not have a simple form. There are, however, several practically important limiting cases in which one can obtain very simple approximate expressions for the oscillation probabilities in terms of the two flavour ones.

1.3.2 Matter effects in neutrino oscillation

Matter effects play a very important role in neutrino oscillations. Neutrino oscillations in matter may differ from the oscillations in vacuum significantly. The most salient feature of the matter effects on neutrino oscillations is the resonance enhancement of the oscillation probability – the Mikheyev - Smirnov - Wolfenstein (MSW) effect [26]. In vacuum, the flavour oscillation can not exceed $\sin^2 2\theta_{ij}$, where θ_{ij} is the mixing angle, and for small mixing angles it is always small. However, matter can enhance neutrino mixing, and the probabilities of neutrino oscillations in matter can be large even if the mixing angle in vacuum is very small. Neutrinos of all three flavours - ν_e, ν_μ and ν_τ – interact with the electrons, protons and neutrons of matter through neutral current (NC) interaction mediated by Z^0 bosons. Electron neutrinos in addition have charged current (CC) interactions with the electrons of the medium, which are mediated by the $W^\pm$ boson exchange. For neutrino traversing the Earth, oscillation probability is calculated taking into account Earth's matter potential due to the forward scattering amplitude of charged current ν_e interactions with electrons. Neutral current interactions are neglected here because they lead to flavour-independent terms which are irrelevant for the oscillation probabilities.

The CC interactions are described by the effective Hamiltonian:

$$H_{CC} = \frac{G_F}{\sqrt{2}}[\bar{e}\gamma_\mu(1-\gamma_5)\nu_e][\bar{\nu}_e\gamma^\mu(1-\gamma_5)e] = \frac{G_F}{\sqrt{2}}[\bar{e}\gamma_\mu(1-\gamma_5)e][\bar{\nu}_e\gamma^\mu(1-\gamma_5)\nu_e] \tag{1.22}$$

where the Fierz transformation is used. In order to obtain the coherent forward scattering contribution to the energy of ν_e in matter (i.e. the matter-induced potential for ν_e), we fix the variables corresponding to ν_e and integrate over all the variables that correspond to the electron:

$$H_{eff}(\nu_e) = \langle H_{CC} \rangle_{electron} \equiv \bar{\nu}_e V_e \nu_e\,. \tag{1.23}$$

Furthermore, we have:

$$\langle \bar{e}\gamma_0 e\rangle = \langle e^\dagger e\rangle = N_e\,, \qquad \langle \bar{e}\gamma e\rangle = \langle \mathbf{v}_e\rangle\,, \quad \langle \bar{e}\gamma_0\gamma_5 e\rangle = \langle \frac{\sigma_e \mathbf{p}_e}{E_e}\rangle\,, \quad \langle \bar{e}\gamma\gamma_5 e\rangle = \langle \sigma_e\rangle\,, \tag{1.24}$$

where N_e is the electron number density. If the matter is unpolarized and at rest, only N_e is non-zero. Thus, we obtain:

$$V_{CC} = \sqrt{2}\,G_F N_e\,. \tag{1.25}$$

This is also known as the MSW matter potential.

Similarly, one can find the NC contributions V_{NC} to the matter-induced neutrino potentials. Since NC interaction are flavour independent, these contributions are the same for neutrinos of all three flavours. In an electrically neutral medium, the number densities of protons and electrons coincide and the corresponding contributions to V_{NC} cancel. Hence, the net effective potential for neutral current interaction of neutrinos of all three flavours with electrons, protons and neutrons in matter can be computed to be

$$V_{NC} = G_F \left(\frac{N_n}{\sqrt{2}}\right)\,. \tag{1.26}$$

where N_n is the neutron number density. The number density of electrons is given by $N_e = N_A\, Y_e\, \rho$, where N_A is Avogadros number, Y_e is the electron fraction per nucleon and ρ is the matter density. For practical calculations, it is sometimes convenient to express V_{CC} in terms of the matter density ρ and the number of electrons per nucleon Y_e :

$$V_{CC} = \pm 7.56 \times 10^{-14} \left(\frac{\rho}{g/cm^3}\right) Y_e\, eV \tag{1.27}$$

$Y_e \approx 0.5$ for earth matter.

For antineutrinos, the particle number is negative, and the potential terms V_{CC} and V_{NC} will be modified by:

$$V_{CC} \to -V_{CC} \quad \text{and} \quad V_{NC} \to -V_{NC}$$

Two flavour case

In the presence of matter, the evolution equation in flavour basis in the case of 2 neutrino flavours gets modified to:

$$i\frac{d}{dt}|\nu_f\rangle = \tilde{H_f}|\nu_f\rangle = UH_0U\dagger|\nu_f\rangle\,, \tag{1.28}$$

where:

$$\tilde{H_f} = E + \frac{m_1^2 + m_2^2}{4E} - \frac{G_F N_n}{\sqrt{2}} + \frac{\Delta m^2}{4E}\begin{pmatrix} -\cos 2\theta + \frac{2A}{\Delta m^2} & \sin 2\theta \\ \sin 2\theta & \cos 2\theta\,, \end{pmatrix} \tag{1.29}$$

where $A = 2EV_{CC} = 2\sqrt{2}G_F N_e e$ is the effective potential derived above. Following the same argument discussed for Eq. (1.15), we can omit the common terms in diagonal element, thus $\tilde{H_f}$ takes the form:

$$\tilde{H_f} = \frac{\Delta m^2}{4E}\begin{pmatrix} -\cos 2\theta + \frac{2A}{\Delta m^2} & \sin 2\theta \\ \sin 2\theta & \cos 2\theta \end{pmatrix}, \tag{1.30}$$

In order to calculate the oscillation probability, we diagonalize $\tilde{H_f}$ to obtain the effective mass eigenvalues $(m_{1m})^2$ and $(m_{m2})^2$ and the effective mixing angle θ_m.

The mass eigenvalues in matter are given by:

$$(m_{1m,2m})^2 = \frac{A}{2} \pm \frac{A}{2}\sqrt{(A - \Delta m^2\cos\theta)^2 + (\Delta m^2 \sin\theta)^2}\,, \tag{1.31}$$

with a mass splitting of

$$\Delta m_m^2 = \frac{A}{2}\sqrt{(A-\Delta m^2\cos\theta)^2+(\Delta m^2\sin\theta)^2}, \tag{1.32}$$

The effective mixing angle is given by

$$\sin\theta_m = \frac{\sin 2\theta}{\sqrt{(A-\Delta m^2\cos\theta)^2+(\Delta m^2\sin\theta)^2}} \tag{1.33}$$

$$\cos\theta_m = \frac{\Delta m^2\cos 2\theta - A}{\sqrt{(A-\Delta m^2\cos\theta)^2+(\Delta m^2\sin\theta)^2}}. \tag{1.34}$$

The oscillation probabilities still have the same form as the standard two flavour mixing, but are now expressed in terms of the mass eigenstates in matter and the matter modified mixing angle :

$$P_m(\nu_\alpha \to \nu_\beta) = \sin^2 2\theta_m \sin^2\frac{\Delta m_m^2 L}{4E}. \tag{1.35}$$

When $A = \Delta m^2\cos 2\theta$, ν_α and ν_β mix maximally, i.e., $\theta_m = \pi/4$ even if the vacuum mixing angle is small. This is known as maximal mixing and marks the onset of the MSW matter resonance. The resonance enhancement of oscillation of neutrinos in matter to be possible, $\Delta m^2\cos 2\theta$ must be positive. If one chooses the convention $\cos 2\theta > 0$, (as is usually done), then the condition reduces to $\Delta m^2 > 0$. The resonance condition for antineutrinos is then $\Delta m^2 < 0$. Therefore, for a given sign of Δm^2, either neutrinos or antineutrinos (but not both) can experience the resonantly enhanced oscillations in matter.

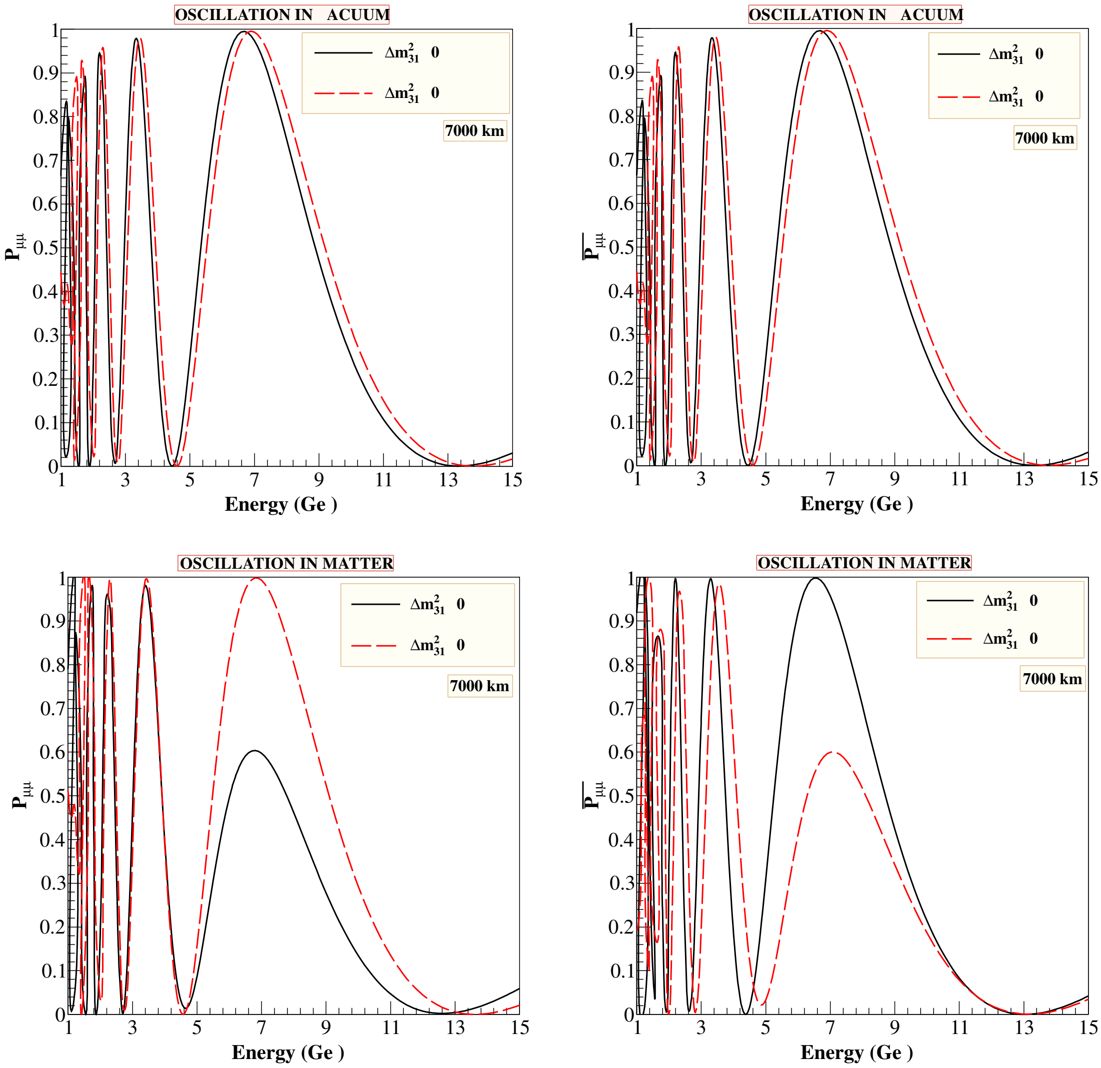

Figure 1.1: ν_μ survival probability vs energy for 7000 km baseline. Above panel: Oscillation in vacuum, lower panel: oscillation in matter. The solid black lines correspond to $\Delta m^2_{31} > 0$ while red-dashed lines are for $\Delta m^2_{31} < 0$.

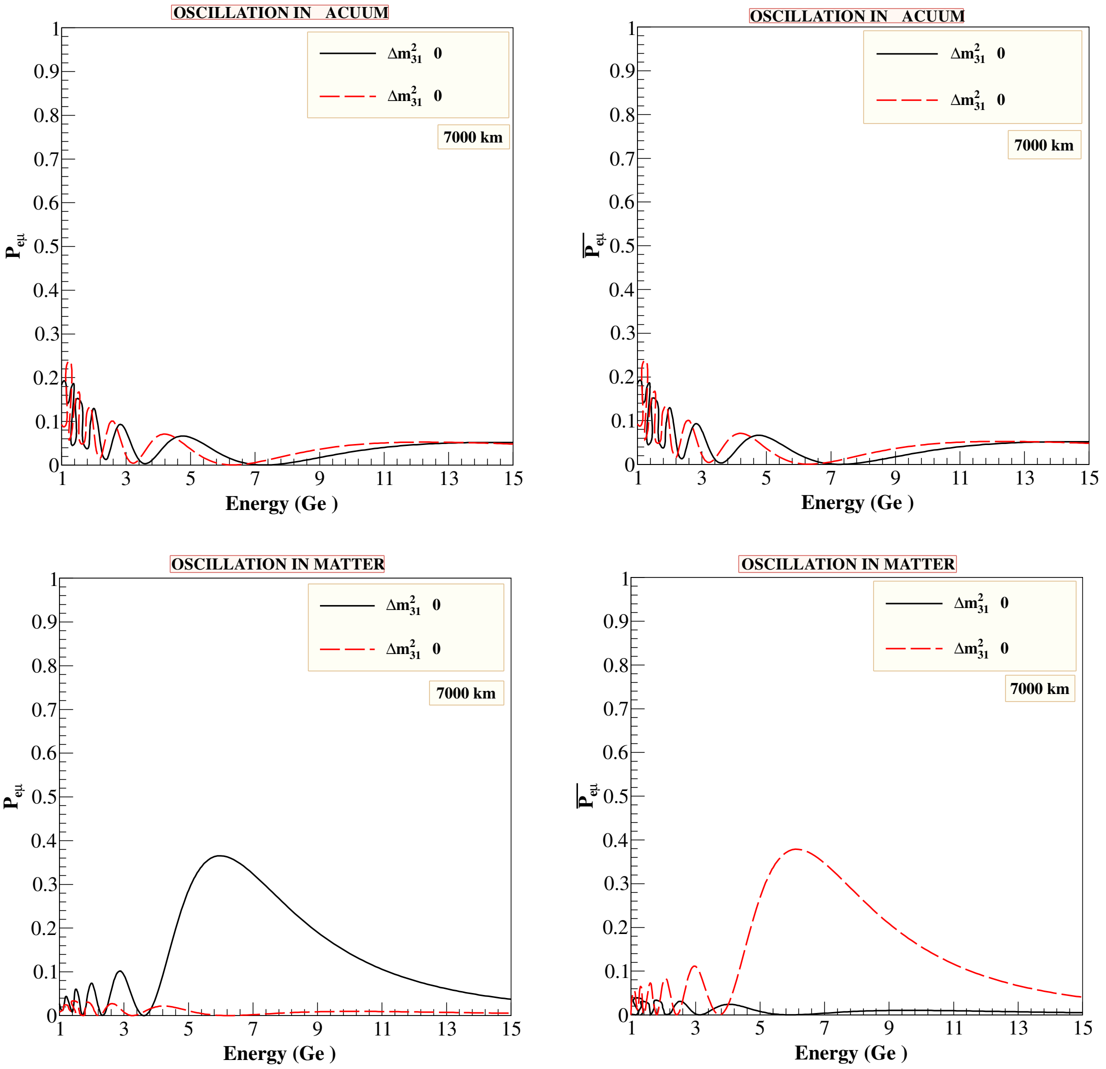

Figure 1.2: ν_e appearance probability vs energy for 7000 km baseline. Above panel: Oscillation in vacuum, lower panel: oscillation in matter. The solid black lines correspond to $\Delta m^2_{31} > 0$ while red-dashed lines are for $\Delta m^2_{31} < 0$.

Three flavour case

The evolution equation describing neutrino oscillations in matter in the case of three neutrino flavours ν_e, ν_μ and ν_τ is

$$i\frac{d}{dt}\begin{pmatrix}\nu_e\\ \nu_\mu\\ \nu_\tau\end{pmatrix} = \left[\frac{1}{2E}U\begin{pmatrix}m_1^2 & 0 & 0\\ 0 & m_2^2 & 0\\ 0 & 0 & m_3^2\end{pmatrix}U^\dagger + \begin{pmatrix}V_{CC} & 0 & 0\\ 0 & 0 & 0\\ 0 & 0 & 0\end{pmatrix}\right]\begin{pmatrix}\nu_e\\ \nu_\mu\\ \nu_\tau\end{pmatrix}. \quad (1.36)$$

Here U is the three flavour vacuum mixing matrix defined in Eq. **??**. In general, it is difficult to study this equation analytically. However, This can be solved exactly by a numerical solution of the evolution equation in matter. For example, we have plotted the oscillation probability $\nu_\mu \to \nu_\mu$ and $\nu_\mu \to \nu_e$ as a function of energy for the baseline 7000 km, where all the plots are obtained by numerically solving the full three flavour neutrino propagation equation assuming the Preliminary Reference Earth Model (PREM) [27] density profile for the earth. In all the panels, black solid line corresponds to $\Delta m^2_{31} > 0$ and red-dashed lines are for $\Delta m^2_{31} < 0$. The resonance enhancement can be seen in the range 2-10 GeV energy. It is evident from the plots that the enhancement occurs when Δm^2_{31} is positive (negative) for the neutrinos (anti-neutrinos).

1.4 Current status of neutrino oscillation

As evident from section 1.1, the neutrino mixing matrix, or U_{PMNS} can be parametrized in terms of three mixing angles θ_{12}, θ_{13}, θ_{23}, and a charge-parity violating (CP) phase δ_{CP}. In addition, the frequencies of neutrino oscillations are governed by two mass squared differences, Δm^2_{21} and Δm^2_{31} The so-called solar neutrino oscillation parameters θ_{12} and Δm^2_{21} have been measured from the combined analysis of the KamLAND reactor $\overline{\nu}_e$ data and the solar neutrino data. The so-called atmospheric neutrino oscillation parameters θ_{23}

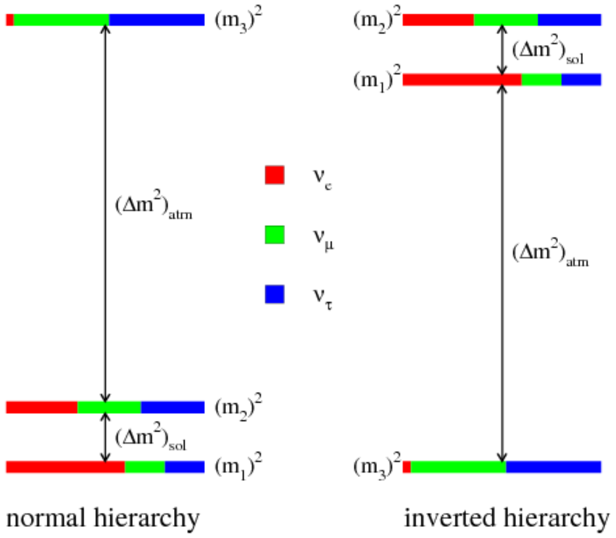

Figure 1.3: The two possible hierarchies of neutrino mass eigenstates, normal hierarchy (left) and inverted hierarchy (right).

and $|\Delta m^2_{31}|$ are mostly constrained by the Super-Kamiokande (SK) atmospheric, and MINOS as well as T2K ν_μ disappearance data. The third and the last mixing angle θ_{13} is the latest to be measured by a series of accelerator and reactor experiments. After decades of speculation on whether θ_{13} was zero, data from these experiments have revealed that the value of θ_{13} is not only non-zero, it is in fact just below the previous upper bound [8] from the Chooz experiment. Accelerator-based neutrino experiments T2K and MINOS have both observed ν_e appearance events from a beam of ν_μ that indicates a non-zero value of θ_{13}. The short baseline reactor neutrino experiments Daya Bay, RENO and Double Chooz have excluded $\theta_{13} = 0$ at 5.2σ, 4.9σ and 3.1σ respectively from $\overline{\nu}_e$ disappearance. Their best fit values are $\sin^2 2\theta_{13} = 0.092 \pm 0.016(\text{stat}) \pm 0.005(\text{syst})$ [10], $\sin^2 2\theta_{13} = 0.113 \pm 0.013(\text{stat}) \pm 0.019(\text{syst})$ [11] and $\sin^2 2\theta_{13} = 0.109 \pm 0.030(\text{stat}) \pm 0.025(\text{syst})$ [12], respectively. We summarize our current understanding of the neutrino oscillation parameters in Table 1.1. While the above experiments continue to improve the precision on the mixing angle θ_{13}, the focus has now shifted to the determination of the other unknown parameters in the neutrino sector. Survival and oscillation probabilities depend on the above four mixing parameters as well as on the two independent mass-squared differ-

Parameter	Best Fit Value	3σ Ranges
$\sin^2\theta_{12}$	0.307	0.259-0.359
$\sin^2\theta_{23}$	0.386 0.392	0.331-0.637 (NH) 0.335-0.663 (IH)
$\sin^2\theta_{13}$	0.0241 0.0244	0.0169-0.0313 (NH) 0.0171-0.0315 (IH)
Δm^2_{21} (eV^2)	7.54×10^{-5}	6.99-8.18 $\times10^{-5}$
$\lvert\Delta m^2_{31}\rvert$ (eV^2)	2.43×10^{-3} 2.42×10^{-3}	2.19-2.62 $\times10^{-3}$ (NH) 2.17-2.61 $\times10^{-3}$ (IH)

Table 1.1: A summary of the current values of the neutrino oscillation parameters
A summary of the current values of the neutrino oscillation parameters. The values are taken from [28]. NH and IH indicate the limits applicable if the mass hierarchy is normal and inverted, respectively.

ences Δm^2_{21}(known as the solar mass-squared difference, since it governs the oscillations of solar neutrinos) and Δm^2_{31} (known as the atmospheric mass-squared difference, since it governs the oscillations of atmospheric neutrinos). Solar neutrino data require Δm^2_{21} to be positive. However, data from atmospheric neutrinos as well as accelerator neutrino experiments (K2K and MINOS) constrain only the magnitude of Δm^2_{31} but not its sign. Determining the sign of Δm^2_{31} is also of crucial importance, since its knowledge is essential for constructing the mass spectrum of neutrinos. If the sign of Δm^2_{31} is positive, then we have the following mass pattern $m_3 \gg m_2 \gg m_1$ This is referred to as normal hierarchy (NH).If the sign of Δm^2_{31} is negative, then the mass pattern is $m_2 \geq m_1 \gg m_3$. This is referred to as inverted hierarchy (IH). In Fig. 1.3 shows the conceptual diagram for two types of the mass order.

The CP violating phase δ_{CP} is another unknown quantity. Though the current global analyses [28, 29] have started to provide some hints about the value of δ_{CP}, these are still early days, and better data from dedicated experiments would probably be required before one could make any definitive statement on whether CP is violated in the lepton sector as well. The answer to this question would have far reaching implications, as a positive answer would lend support to the idea of baryogenesis via leptogenesis during the early universe.

The issue regarding the value of $\sin^2\theta_{23}$ and its correct octant is not yet settled. The Super-Kamiokande collaboration get the best-fit to their atmospheric zenith angle data at $\sin^2 2\theta_{23} = 0.98$ [14]. The MINOS collaboration best-fit $\sin^2 2\theta_{23} = 0.96$ [15], where they included in their analysis the full MINOS data with 10.71×10^{20} POT for ν_μ-beam, 3.36×10^{20} POT for $\bar{\nu}_\mu$-beams, as well as their 37.9 kton-years data from atmospheric neutrinos. It is worth pointing out here that the Super-Kamiokande best-fit is close to maximal and even the MINOS collaboration results allow maximal mixing at 1σ C.L. [15]. However, results from global analyses performed by groups outside the experimental collaborations have now started to show deviation from maximal mixing and prefer $\sin^2\theta_{23}$ in the first octant [30, 31]. These results though should be taken only as a possible ”hint” as they require further investigation by the analysis using the full detector Monte Carlo of the experimental collaborations. a large number of neutrino experiments are already under way or being planned to work towards achieving these aims. This thesis aims to show the physics potential of future neutrino experiment ICAL@INO in determining the mass hierarchy and precision measurement of atmospheric parameters. The thesis is organized is as follows: chapter 2 describes the ICAL detector. In Chapter 3 we discuss the ICAL detector simulation for hadrons shower reconstruction which is crucial for neutrino energy reconstruction. Chapter 4 contains the detail description of the simulation framework used for studying the physics potential of ICAL@INO. Next, in chapter 5 we give the simulation result for mass hierarchy sensitivity of ICAL@INO using final state muon events. In chapter 6 we discuss how to improve the mass hierarchy sensitivity by improving detector response of ICAL and also by inclusion of hadron events along with the muon events. Here we also do a comparative study between neutrino analysis and muon analysis for mass hierarchy sensitivity. Chapter 7 contains the result for precision measurement of mixing angle θ_{23} and atmospheric mass square difference Δm^2 at ICAL@INO. The thesis is winded up by summarizing the results in chapter 8.

CHAPTER 2

IRON CALORIMETER DETECTOR@INO

India based Neutrino Observatory (INO) is a proposed underground high energy physics laboratory whose major activity will be in neutrino physics. The proposed detector is the magnetized Iron CALorimeter aka ICAL with the target mass of about 50 kton. The ICAL detector is envisaged as a detector for atmospheric neutrinos. It will use magnetized iron as the target mass and Resistive Plate Chambers (RPCs) as the active detector medium. The main physics goals of ICAL@INO are:

- Re-confirmation of the occurrence of oscillation in atmospheric muon neutrinos through the explicit observation of the first oscillation swing in ν_μ disappearance as a function of L/E where L is the neutrino flight length and E is the neutrino energy.
- Search for potential matter effects in neutrino oscillations.
- Determining the sign of Δm^2_{31} and hence the neutrino mass hierarchy using matter

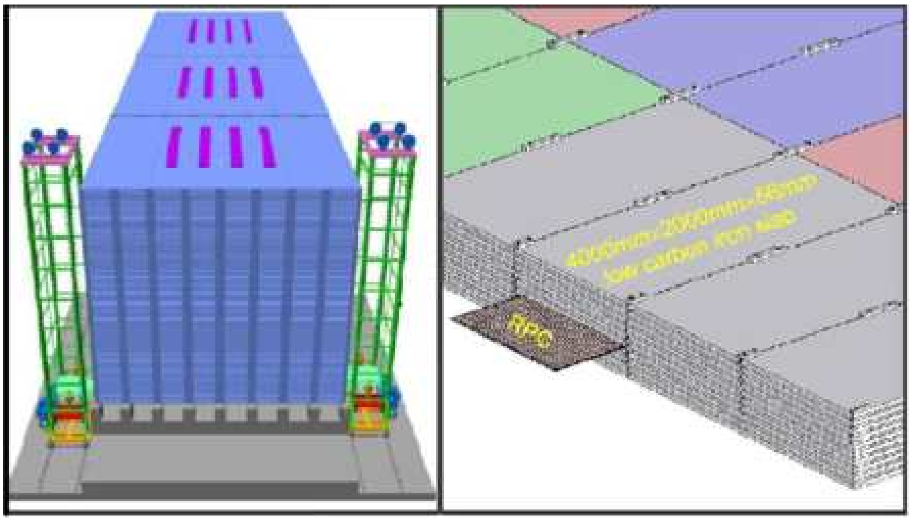

Figure 2.1: Left: Schematic of ICAL detector. Right: a close up view of the stack and RPC insertion method is shown.

effect.

- Precise measurement of $|\Delta m^2_{31}|$ and $\sin^2 2\theta_{23}$.
- Measure the deviation of θ_{23} from maximality, and resolve the octant ambiguity.

Apart from these, ICAL@INO will also look for new physics e.g.,:

- Probing CPT violation in the neutrino sector using atmospheric neutrinos.
- Looking for signature of non-standard interaction in neutrino oscillation.
- Being a large neutrino detector, ICAL@INO will look for indirect search of dark matter.
- Constraining long range leptonic forces.

2.1 The ICAL detector

A schematic illustration of the ICAL detector is shown in Fig. 2.1. The proposed detector will have a modular structure of total lateral size 48 m × 16 m and the height of the

ICAL	
No. of modules	3
Module dimension	16 m × 16 m × 14.5 m
Detector Dimension	49 m × 16 m × 14.5 m
No. of RPC layers	150
Iron plate thickness	5.6 cm
Gap of RPC trays	4 cm
Magnetic filed	1.3 Tesla

RPC	
RPC unit dimension	1.84 m × 1.84 m× 24 mm
Readout strip width	3 cm
No. of RPC units/Road/Layer	8
No. of Roads/Layer/Module	8
No. of RPC units/Layer	192
Total no. of RPC units	28800
No.of electronic readout channels	3.7×10^6

Table 2.1: ICAL detector specifications.

detector will be 14.5 m. The detector will be comprised of three modules of size 16 m × 16 m whereas each module will consist of a stack of 151 horizontal layers of 5.6 cm thick low carbon iron plates interleaved with 40 mm gaps to house the active detector layers–Resistive Plate chambers(RPC). Salient features of the ICAL detector and its active detector elements are summarized in Table 2.1. The iron structure for this detector will be self supporting with the layer above resting on the layer immediately below using iron spacers located every 2 m along the X-direction. This will create 2 m wide roads along the Y-direction for the insertion of RPC trays. There will be a total of 8 roads per module in a layer. The iron plates will be magnetized with a field of about $\sim$ 1.3 Tesla.

This chapter is organized as follows: in sec 2.2, we briefly describe the schematic diagram and working principle of the active element of ICAL detector, RPC. In the next section 2.3 we shortly describe the readout system of RPC. Section 2.4 and section 2.5 contain a short discussion about the electronics and gas system of the RPC respectively.

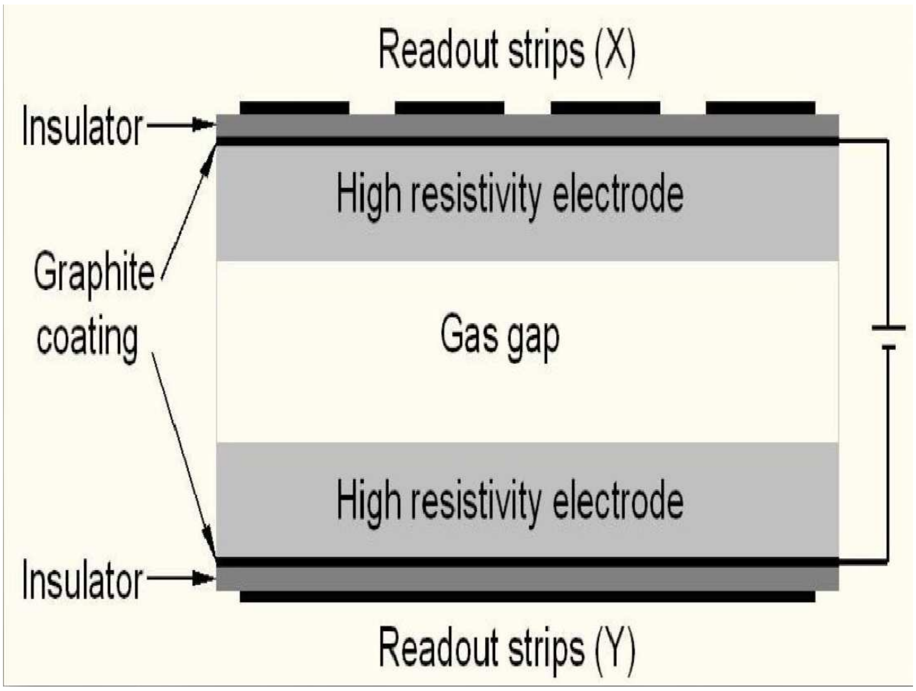

Figure 2.2: Schematic diagram of RPC.

2.2 Resistive Place Chamber (RPC) – the active part of the detector

Resistive Plate Chambers (RPCs) are gaseous parallel plate detectors made of electrodes of high volume resistivity such as glass or bakelite. The main features of these detectors are large signal output, excellent time resolution as well as position resolution and low cost per unit area of coverage.

A simple schematic diagram of the RPC detector is shown in Fig. 2.2. Two planar electrodes made from a resistive material (typically glass or bakelite) with a bulk resistivity of $10^{10}10^{12}$ Ω-cm are spaced by a few mm. The electrodes are kept apart by means of small polycarbonate cylindrical spacers having a diameter of $\approx$ 10 mm and a bulk resistivity greater than 10^{13} Ω-cm, epoxied to both electrodes at regular intervals in such a way that they channel the gas flow through the chamber uniformly. Additional T-shaped spacers are epoxied at the edges of the glass plates to make the whole module gas tight. In order to create a uniform and intense electric field (about 5 kV/mm) in the gap, The electrodes are connected to a high voltage power supply. A thin layer of graphite is also coated over the external surface of the electrodes to distribute the high voltage uniformly.

2.2.1 Working principle of RPC

A gas mixture with a high absorption coefficient for ultraviolet light is flown through the gap between the electrodes. When the gas is ionized by a charged particle crossing the chamber, free charge carriers that are deposited in the gas gap trigger avalanches of electrons in the externally applied electric field and originate a discharge. Due to the high resistivity of the electrodes, the electric field is suddenly dropped down in a limited area around the point where the discharge occurred. Thus the discharge is prevented from propagating through the whole gas volume. The sensitivity of the counter remains unaffected outside this small area. On the other hand, due to the ultra-violet absorbing component of the gas mixture, the photons produced by the discharge are not allowed to propagate in the gas. This prevents secondary discharges from originating at other points of the detector. The propagation of the growing number of electrons induces a current on external strip electrodes.

The RPCs may be operated either in the avalanche mode or streamer discharge mode. The avalanche mode corresponds to the generation of a Townsend avalanche following the release of primary charge due to the passage of an ionizing radiation through the gas volume. In the streamer mode the avalanche is followed by a ’streamer’ discharge. The RPCs working in the avalanche mode mostly use mixtures of tetrafluoroethane ($C_2H_2F_4$ - also known as R134a) with 2-5% of isobutane (iso-C_4H_{10}). In the streamer mode, mixtures of argon with isobutane and tetrafluoroethane in widely varying proportions are used.

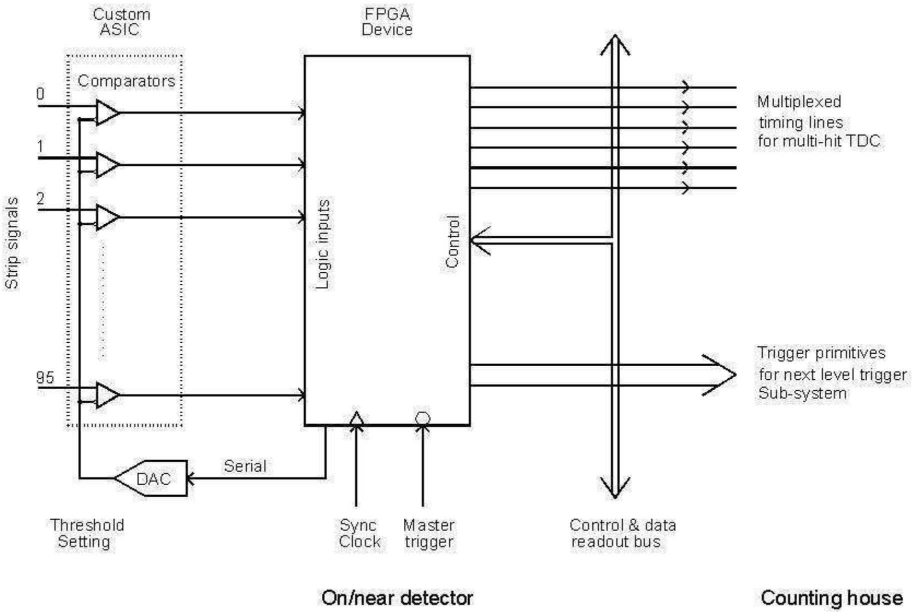

Figure 2.3: Proposed readout scheme for the ICAL detector.

2.3 The readout schemes

The readout of the RPCs will be performed by external orthogonal pickup strips (X and Y strips). A localized discharge due to the passage of charged particles will induce pulses on the appropriate strips. These will go to front end ASICs located near the strip ends which will have fast discriminators that will provide a fast timing signal. Presently the proposed strips are 3 cm wide. However this can be optimized through simulation studies which are currently ongoing. Thus in the current plan each road of RPCs will be read out by 64 strips along the X-direction (2 m) and 512 strips along the Ydirection (16 m).

2.4 The readout electronics

The conceptual readout scheme is illustrated in Fig 2.3. The incoming detector signals are passed through programmable threshold comparators for producing digital logic signals. These signals are used for recording Boolean hit information, for generating trigger primitives as well by time multiplexing blocks for generating timing signals. Signals from only one coordinate will be used for generating the trigger. Processing of only one coordinate signals for generating trigger primitives and using time multiplexing techniques for recording timing information will reduce the DAQ channel count and hence the cost. Similar techniques are already being used in other experiments such as the Belle experiment [32] in Japan and have been proposed by the Monolith Collaboration [33] in Italy. The time multiplexing scheme combines hit information from a block of strip channels into a single data stream which can be passed on to multi-hit TDCs at the back end. In this scheme, the front-end processing will be achieved by a custom ASIC chip whereas the hit recording and time multiplexing is done by a commercial FPGA device.

The trigger generator is an independent sub-system which uses the same hit signals to look for required patterns of hits in the detector and initiate data recording if any of the interesting predefined hit patterns occur inside the detector. For instance, a trigger may be generated when certain hit patterns such as 2 or 3 hit layers out of 5 consecutive layers occur. This will ensure the trigger generation of nearly all the relevant atmospheric neutrino events. Programmability is the key requirement of this sub-system so that different physics motivated data recording plans may be supported during the course of experiment. A commercial FPGA device based design is best suited for this purpose. We plan to use the VME standard for the DAQ system and hosts will be based on Linux PC boxes.

2.5 Gas System

The total volume of the active detector elements of ICAL will be $\sim 216m^3$. The gas distribution system for such a big detector will be a recycling system with approximately one volume change per day. The whole detector will be divided into several zones. Each zone will have a gas supply from a separate gas mixing system. The three gases (argon, isobutane and R-134a) will be sent to mass flow controllers for mixing in appropriate ratios. The gas distribution system will be designed to provide independent gas supply to each road (8 RPC modules). Mixed gas will be distributed to 24×140 roads through a series of manifolds. Uniform distribution in each road will be maintained by flow resistors. Active control of the exhaust pressure and relief bubblers will be introduced to avoid an over pressure situation.

In next chapter, we discuss about the detector simulation and hadron shower reconstruction of ICAL.

CHAPTER 3

DETECTOR SIMULATION OF ICAL FOR HADRON SHOWER RECONSTRUCTION

ICAL will use atmospheric neutrino as source. Atmospheric neutrino interacts with ICAL via charge current (CC) and neutral current (NC) interaction. The main CC interactions of the neutrinos in the detector are quasi-elastic (QE) and resonance (RS) interactions at low energies (up to a few GeV) and deep-inelastic scattering (DIS) at higher energies. All CC neutrino interaction events produce the associated lepton. The DIS events usually produce a large number of accompanying hadrons (mostly pions) while resonance interactions produce at most one pion along with the lepton. Among the leptons , electron (associated with electron neutrino) mostly absorbs inside the thick (5.6 cm) iron plate whereas, tau (associated with tau neutrino which are produced via appearance channel) decays to muon because of its short life time. Only muon (associated with muon neutrino) gives a clean track inside

ICAL. Muon momentum can be reconstructed from the tracklength of the muon. As, ICAL is magnetized, muon momentum can also be reconstructed from the bending of the track. ICAL has very good energy and excellent direction resolution for muon.
Hadron interacts via strong force and produces shower instead of tracks because of which a bunch of hits are created near the vertex. hadron energy are calibrated using those hit informations. For CC interactions, the neutrino can be reconstructed by reconstructing the final state muon and hadron. This chapter is organized as follows: in section 3.1, we briefly discuss how the ICAL detector simulated. In section 3.2, we described the hadron shower reconstruction which is simulated using single pion events.

3.1 Detector simulation

The CERN-library-provided detector description and simulation tool, GEANT4 [37, 38, 39], has been used both to define the detector geometry as well as simulate the detector response for the neutrino event, that is, propagate muons and hadrons, produced by neutrino interactions in the detector, through the simulated detector volume. The detector design, as mentioned in chapter 2, has been implemented in the simulated detector geometry where the details such as spacers within the RPC, dead-spaces due to insertion of copper coils for magnetization, alterations due to support structures – all are taken into account. Detailed simulations of the magnetic field for proposed coil configurations has been done and also has been incorporated in the simulation code.

Particles such as muons are tracked through the ICAL by determining the number of RPC's that the particle has passed through. The charged particle triggers the RPC by the energy it loses inside the medium and registers a hit [40]. All secondaries that may be produced by passage of the primary particle through the detector medium are tracked as well. While there are very few secondaries generated by minimum-ionizing particles such as muons, hadrons generate secondaries copiously due to their strong interactions with the medium. Many of these secondary showers are absorbed by the iron layer, and some of the remaining produce hits inside the detector. The digitization of hits is done by determining the coordinates of x and y strips of the hit and determining the z coordinate from the layer number.

The RPCs are assumed to give nano-second timing (for up/down discrimination). While it may not be possible to have sufficiently good time-resolution between successive hits, the requirement of minimum number of hits for reconstruction ensures that the over-all timing efficiency and hence up/down discrimination is 100%. In this analysis, we have not used any energy information which may be obtained from the pulse height; all calibration is done by calibrating the track length (for muons) and number of hits (for hadrons).

3.2 Hadron shower Reconstruction

The hadrons consist mainly of pions (about 85% of events on the average), kaons, and also nucleons, including the recoil nucleon which cannot be distinguished from the remaining hadronic final state. Both neutral and charged pions may be produced. The neutral pion decays immediately, giving rise to two photons, while the charged pions propagate and develop into a cascade due to strong interactions. The main uncertainty in determining the incident neutrino energy comes from the uncertainty in estimating the energy of these hadrons. Typically a muon leaves a distinct track whereas the hadrons leave a shower of hits close to the vertex. For the interaction $\nu_\mu N \to \mu X$, the incident neutrino energy is given by

$$\mathrm{E}_\nu = \mathrm{E}_\mu + \mathrm{E}'_{\mathrm{had}}, \tag{3.1}$$

where $E'_{\rm had}$ is the difference in the total energy of the final state hadrons (including the recoil nucleon) and the energy of the initial state nucleon — including the rest mass, Fermi momentum and binding energy. We use $E'_{\rm had}$ as an observable for hadron energy since it would enable us to reconstruct the neutrino energy in a straightforward manner.

The analysis is done with Mono-energetic charged pions are propagated through the detector and their characteristics studied. In general the energy resolution of hadrons is affected by various factors like shower energy fluctuation, leakage of energy and invisible energy loss mechanisms.

In this analysis, we use a full simulation of the event propagation in ICAL to assess the detector's capability to estimate hadron energy. We first discuss the hit distributions of hadrons in the detector. This is done by a Monte-Carlo (MC) generator that generates hadrons at fixed energies up to 15 GeV. The hits are are estimated using the hit multiplicity information of events generated with appropriate position and angle smearing. We then specifically discuss the pion energy (E_π) resolution by propagating pions with fixed energies through the simulated detector.

3.2.1 Energy resolution with fixed energy pions

As discussed in section 3.1 when a charged particle propagates through the ICAL detector, hits in the X and Y strips of the RPC layers are recorded. The layer number provides the z-coordinate. Thus the full position information is available. A muon usually leaves one or two hits per layer and so the hits from both X and Y strips can easily be combined to obtain the number of hits and their position coordinates (x, y) in a given layer. However, in the case of hadron shower there are multiple hits per layer, and combining X and Y strip hits leads to some false count of hits (ghost hits). To avoid the ghost hit counts, the energy calibration may be done with counts from either X or Y strips. The variables x-hits and y-hits store the number of hits in the X and Y strips of the RPC, respectively. The maximum

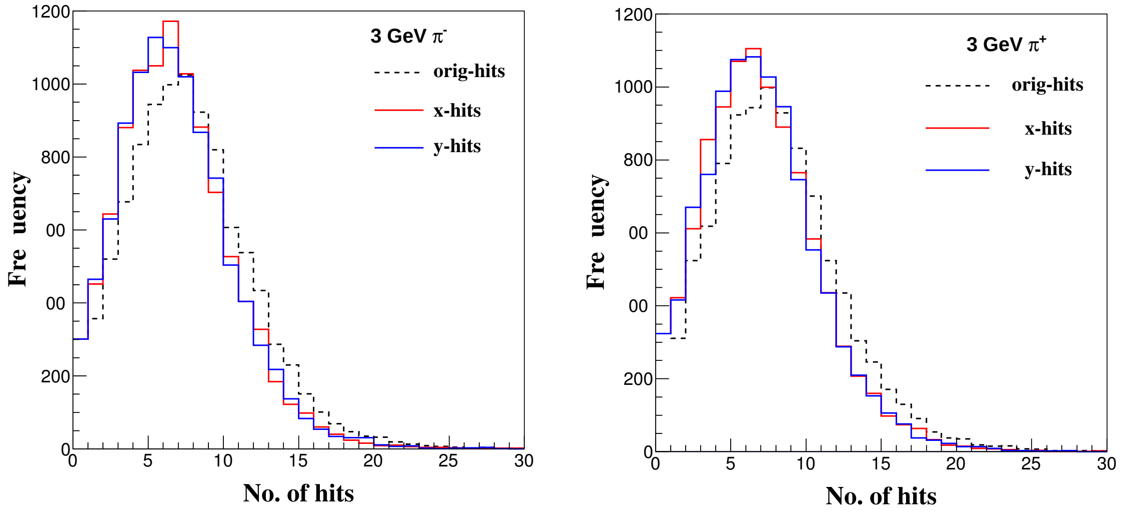

Figure 3.1: The comparison of the distributions of x-hits, y-hits and orig-hits for (left) π^- and (right) π^+ of energy 3 GeV.

of x-hits or y-hits is stored as the variable orig-hits. In Fig. 3.1, the comparison of these three types of hit variables are shown for $\pi^\pm$ of energy 3 GeV. As is clear from Fig. 3.1, we could have used any of the x-, y-or orig-hits in the analysis; we choose to use orig-hits as the unbiased parameter.

The total number of events generated for each input energy value is 10000. Each event is randomly generated over a volume 200 cm × 200 cm × 200 cm in the central region of the ICAL detector. In addition, since there is very little impact of the magnetic field on the showers produced by hadrons, the hadron direction is uniformly smeared over zenith angle $0 \leq \theta \leq \pi$ and azimuth of $0 \leq \phi \leq 2\pi$. The angles are denoted with respect to a reference frame, where the origin is taken to be the center of the detector, the z-axis points vertically up, while the plates are horizontal in the x-y plane. This serves to smear out any angle-dependent bias in the energy resolution of the detector by virtue of its geometry which makes it the least (most) sensitive to particles propagating in the horizontal (vertical) direction.

In Fig. 3.2 the hit distributions in the detector for pions, kaons, and protons at various energies in the range of 1 to 15 GeV are shown. We observe that for all these hadrons the hit patterns are similar, though the peak position and spread are somewhat dependent on the particle. The detector cannot distinguish the specific hadron that has generated the shower. Since hadrons produced in neutrino interactions with ICAL are primarily charged pions, we focus our attention on the detector response to pions. However, since the energy response of all hadrons appears to be rather similar, there should be no significant information loss even when we cannot identify the final state hadrons.

We will therefore use the hit distribution of charged pions at various energies to determine the detector response. In particular we determine the mean and variance of the distribution and their energy dependence. This information is required in order to determine the energy calibration for use in physics studies with ICAL.

3.2.2 Analysis of the pion ($\pi^{\pm}$) hit pattern

The pion hit distributions at sample values of $\mathrm{E} = 3, 8$ GeV are shown in Fig. 3.3, where the arithmetic mean and rms value obtained from the histogram are also listed. Typical patterns show a mean of roughly 2 hits per GeV as seen from the figure, but with long tails, so the distribution is not symmetric. In addition, several events yield zero hits in the detector at lower energies, such events are virtually absent at higher energies.

Fig. 3.3 also shows the fits to the Gaussian distribution. As can be seen from the figure, the quality of the fit at the lower energy ($\mathrm{E} = 3$ GeV) is poor, with a χ^2 per degree of freedom, $\chi^2/\mathrm{ndf} \approx 5.2$. This improves to $\chi^2/\mathrm{ndf} \approx 2.3$ for $\mathrm{E} = 8$ GeV. This clearly indicates that the hit pattern is non-Gaussian for lower energy pions. This is also easily understood because of the long non-Gaussian tails. However, at high energies the hit distribution is well approximated by a Gaussian.

The mean $\bar{n}(\mathrm{E})$ of the number of hits from Gaussian fit at various energies is shown in the Fig. 3.4. It increases with increasing pion energy, and saturates at higher energies. It

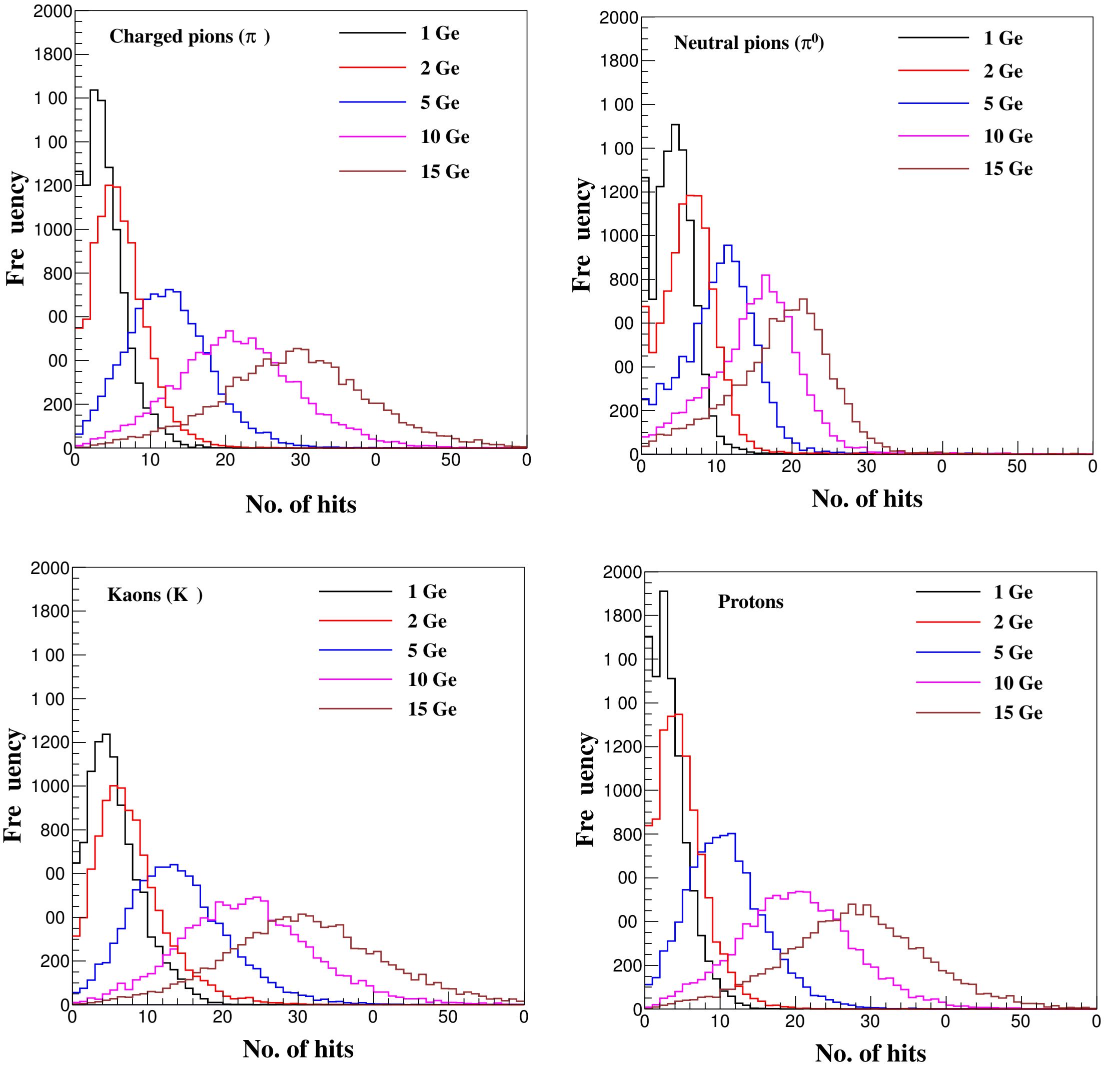

Figure 3.2: The hit distributions at various energies (angle averaged) for $\pi^{\pm}$, π^0, $K^{\pm}$ and protons propagated from vertices smeared over the chosen volume.

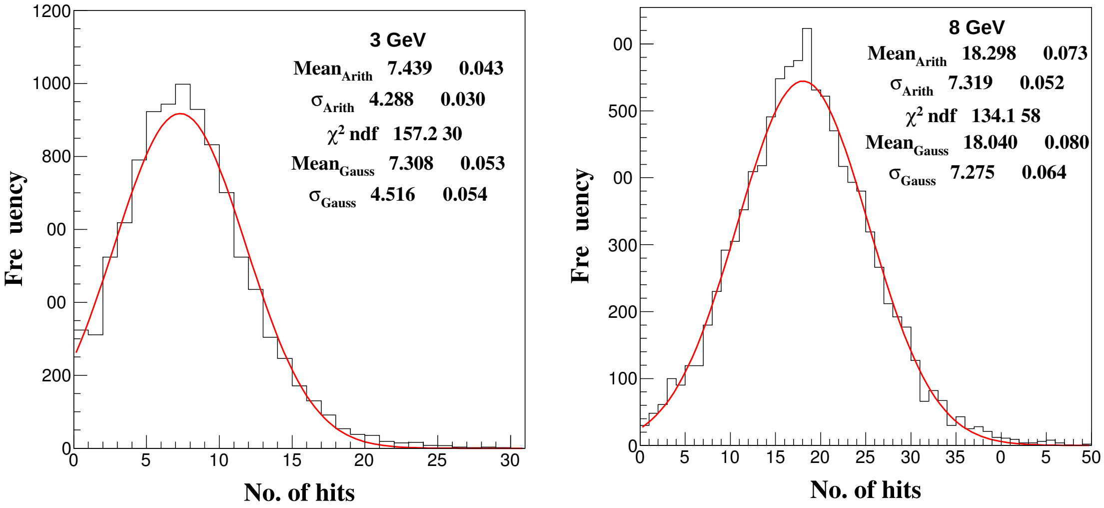

Figure 3.3: The hit distributions at 3 GeV (left) and 8 GeV (right), for pions propagated from randomized vertices over a volume of 200 cm × 200 cm × 200 cm in the detector. A Gaussian fit to the histogram is included for later convenience.

may be approximated by

$$\bar{n}(\mathrm{E}) = \mathrm{n}_0[1 - \exp(-\mathrm{E}/\mathrm{E}_0)], \tag{3.2}$$

where n_0 and E_0 are constants. This fit has to be used with some care, since n_0 and E_0 are sensitive to the energy ranges of the fit. In Fig. 3.4, we compare the means of the hit distributions for π^- and π^+ events in the detector, in the energy range 1 – 15 GeV. We also show the fits to Eq. (3.2). As expected, the mean number of hits for π^- and π^+ are identical within expected statistical fluctuations. The value of E_0 is found to be $\sim$ 30 GeV. Since the energies of interest for atmospheric neutrinos are much less than E_0, we may use Eq. (3.2) in its approximate linear form $\bar{\mathrm{n}}(\mathrm{E}) = \mathrm{n}_0\mathrm{E}/\mathrm{E}_0$. Fig. 3.4 also shows a fit to this linear form.

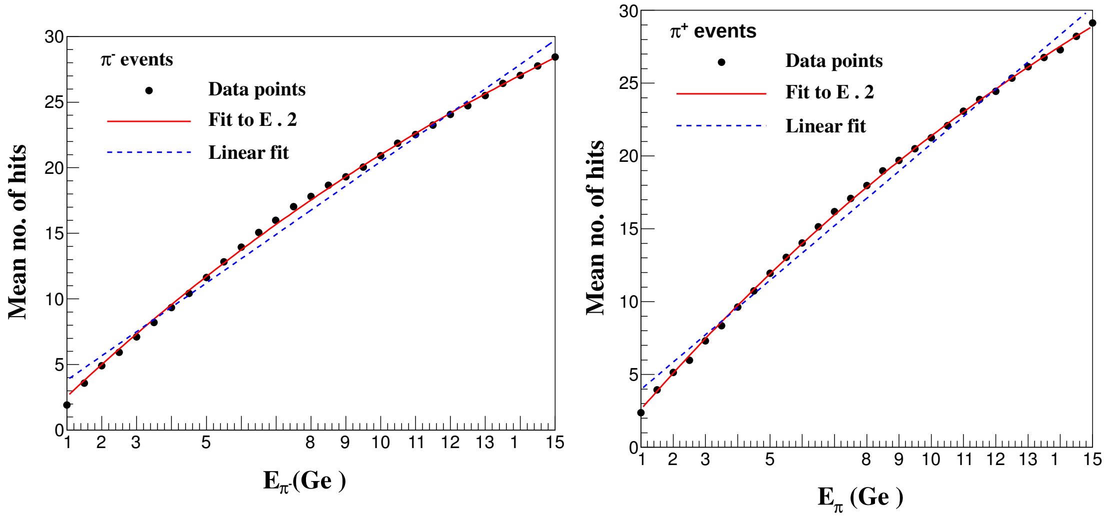

Figure 3.4: Mean hit distribution as a function of pion energy with 5.6 cm iron plates. Left (right) panel shows the mean hit for π^- (π^+). Black dots are the results of simulation while the curves are fits to this simulated data.

3.2.3 Energy Resolution of pion

In the linear regime ($\mathrm{E} \ll \mathrm{E}_0$), we have

$$\frac{\bar{\mathrm{n}}(\mathrm{E})}{\mathrm{n}_0} = \frac{\mathrm{E}}{\mathrm{E}_0}, \tag{3.3}$$

and therefore the energy resolution may be written as

$$\frac{\sigma}{\mathrm{E}} = \frac{\Delta n(\mathrm{E})}{\bar{n}(\mathrm{E})}, \tag{3.4}$$

where $(\Delta n)^2$ is the variance of the distribution. We shall use the notation σ/E for energy resolution.

The energy resolution of pions may be parameterized by

$$\frac{\sigma}{\mathrm{E}} = \sqrt{\left(\frac{a}{\sqrt{\mathrm{E}}}\right)^2 + b^2}\,, \tag{3.5}$$

where a and b are constants. In the literature a is often referred to as the stochastic coefficient which incorporates both statistical and systematic uncertainties. In Fig. 3.5, we show the π^- and π^+ energy resolutions as functions of pion energy, and extract the parameters a and b by a fit to Eq. (3.5) over the energy range 1–15 GeV. It is seen that the fits to both π^- and π^+ yield virtually identical values for a and b.

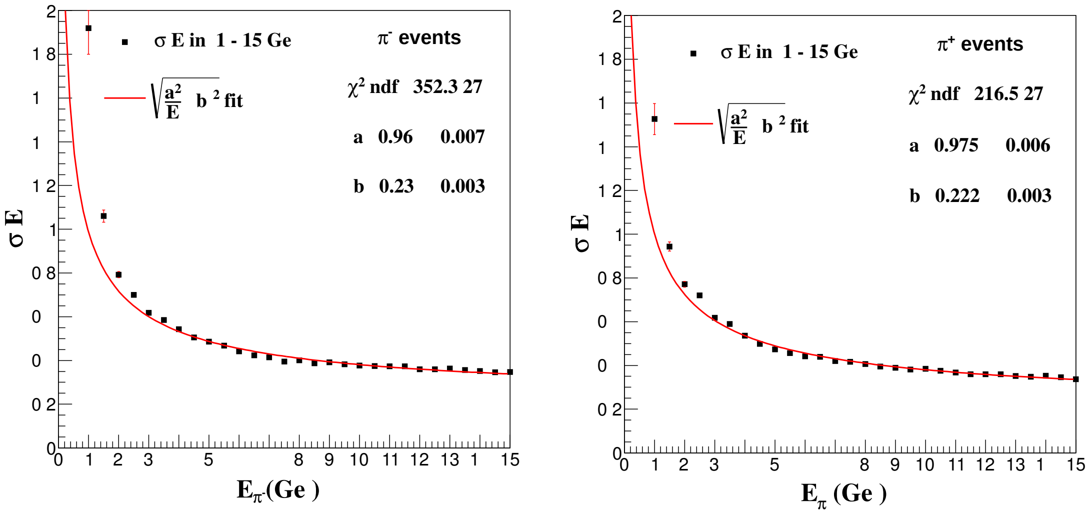

Figure 3.5: Energy resolutions for π^- (left) and π^+ (right) for different energies shown as a function of pion energy. Also shown is the fit to this resolution according to Eq. (3.5).

As observed in this chapter, the Gaussian distribution is not a good approximation at low energies, while, it approximates the hit distribution well at higher energies. It is desirable to find a suitable fit function that correctly reproduces the mean and variance at all energies, and is well-approximated by a Gaussian distribution at higher energies. We have done so in our paper [41].

The next chapter contains the details of the numerical code written for studying the physics potential of ICAL@INO.

CHAPTER 4

SIMULATION FRAMEWORK FOR PHYSICS STUDIES OF ICAL@INO

In this chapter, we describe the numerical procedure used by us for simulating the atmospheric neutrino events to study the physics potential of ICAL@INO. The analysis is based only on the energy, direction, and charge of the muon, for the charged-current (CC) ν_μ events.

The detector response to muons used in this work comes from the first set of simulations done with the ICAL simulation code. These simulations are ongoing and are being fine-tuned. Hence the values of the resolution functions and efficiencies are likely to evolve along with the simulations.

The physics analysis of atmospheric neutrino events requires simulations which can be broadly classified into four steps : (i) neutrino event generation, (ii) inclusion of the oscillation effects, (iii) incorporating detector response, and (iv) the statistical analysis. These steps are described in detail in the following subsections.

4.1 Neutrino event generation

Atmospheric neutrinos have been simulated using the NUANCE neutrino generator [42, 43] adapted for ICAL@INO. The generator provides a choice of neutrino fluxes and also allows 3-flavour mixing to be turned on from source to detection point, apart from providing the relevant interaction cross sections. The HONDA flux [44] [1] for atmospheric neutrinos has been used in the simulations.

For the atmospheric neutrino analysis presented in this thesis, we have generated the unoscillated μ^- and μ^+ events using the NUANCE. In order to reduce the Monte Carlo fluctuations in the event sample, we generate events corresponding to 50×1000 kton-years exposure, which corresponds to 1000 years of running of ICAL@INO. This event sample is finally normalized to a realistic number of years of running of ICAL@INO, when we statistically analyze the data. Since it takes fairly long to run the NUANCE code to generate such a large event sample, running it over and over again for each set of oscillation parameter is practically impossible. Therefore, we run the event generator only once for no oscillations and thereafter impose the reweighting algorithm to generate the event sample for any set of oscillation parameters.

4.2 Inclusion of the oscillation effects

As mentioned above, reweghting algorithm is used to make the unoscillated events oscillated for any set of oscillation parameters. Every ν_μ event given by the event generator is characterized by a certain muon energy and muon zenith angle, as well as a certain neutrino energy and neutrino zenith angle. For this neutrino energy and neutrino zenith angle, the probabilities are calculated numerically for any given set of oscillation parameters. After that, for a given set of oscillation parameters, the reweighting algorithm can be imposed for

---

[1] We use the Honda et. al atmospheric neutrino fluxes calculated for Kamioka [44]. While the atmospheric neutrino fluxes for Theni have been made available recently [45], they are yet to be fully implemented in the ICAL@INO event generator.

two generation or three generation oscillation. The method is described below:

4.2.1 Reweighting algorithm for two generation

Following steps have been taken for two flavour oscillation:

1. For given zenith angle and energy of ν_μ, the survival probability $P_{\nu_\mu \nu_\mu}$ is calculated numerically for two generation.
2. A random number using a uniform distribution in $[0,1]$ is generated (say R).
3. If $R < P_{\nu_\mu \nu_\mu}$ that event is considered as oscillated. Other events are thrown away.

4.2.2 Reweighting algorithm for two generation

Following are general description of reweighting algorithm for three flavours.

1. For given zenith angle and energy of ν_μ, $P_{\nu_\mu \nu_\mu}$ and $P_{\nu_\mu \nu_e}$, $P_{\nu_\mu \nu_\tau}$, are calculated numerically using three generation oscillation.
2. A random number using a uniform distribution in $[0,1]$ is generated (say R).
3. If $R < P_{\nu_\mu \nu_e}$, this event is put in ν_e bin. If $R > (P_{\nu_\mu \nu_e} + P_{\nu_\mu \nu_\mu})$, the event is classified as ν_τ events. If $P_{\nu_\mu \nu_e} \leq R \leq (P_{\nu_\mu \nu_e} + P_{\nu_\mu \nu_\mu})$, the event is classified as ν_μ events. then it means that this event has come from an atmospheric ν_μ which has survived as a ν_μ and is hence selected as muon neutrino event. Since we do this for a statistically large event sample, we get a ν_μ "survived" event spectrum that follows the survival probability to a high precision.

One could also get muon events in the detector from oscillation of atmospheric ν_e into ν_μ. To find these events we generate events from NUANCE using atmospheric ν_e fluxes but ν_μ charged current interactions in the detector, with the oscillation probability

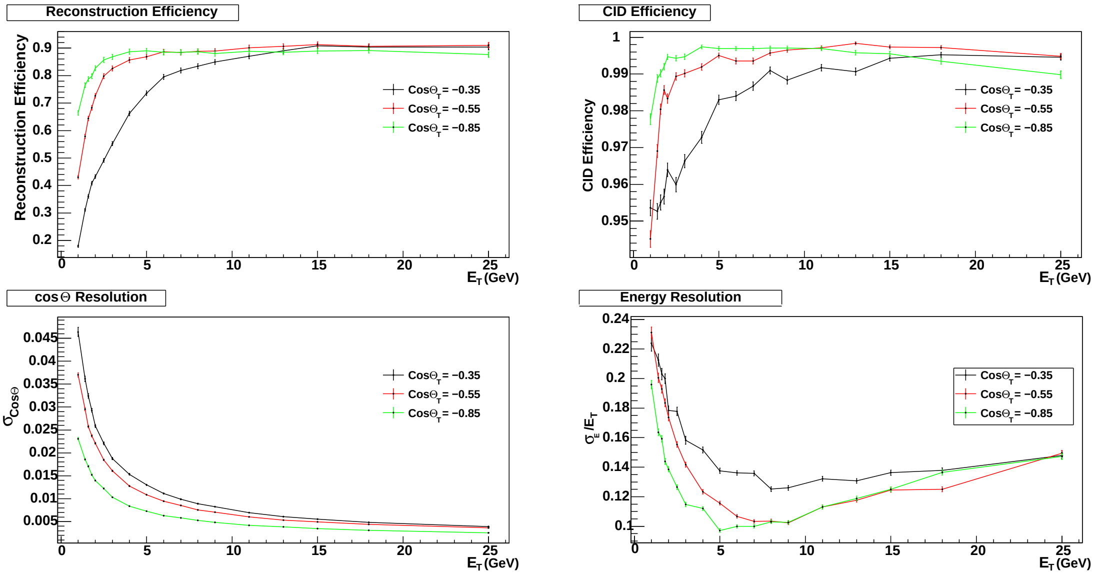

Figure 4.1: The efficiencies and resolutions for muons in ICAL@INO as a function of the true muon energy. The top left panel shows the reconstruction efficiency of muons, the top right panel shows the charge identification efficiency. The bottom left panel shows the zenith angle resolution in $\cos\Theta$ while the bottom right panel shows the energy resolution of the muons. The lines in three colors correspond to three different benchmark zenith angles for the muons.

part of the code switched off. In order to get the oscillated muon event from in this sample we take a random number S and use a similar procedure for classifying the events. That is, if $S < P_{\nu_e\nu_\mu}$, then the event is taken as an "oscillated" ν_μ event. The net number of μ^- events are obtained by adding the "survived" and the "oscillated" ν_μ events. The same exercise is performed for generating the μ^+ events in the detector.

4.3 Incorporating Detector response

The data sample after incorporating oscillations is then distributed in very fine muon energy and zenith angle bins. This raw binned data is then folded with detector efficiencies and resolution functions to simulate the reconstructed muon events in ICAL. In our work we have used (i) the muon reconstruction efficiency, (ii) the muon charge identification efficiency, (iii) the muon zenith angle resolution and (iv) the muon energy resolution, which have been

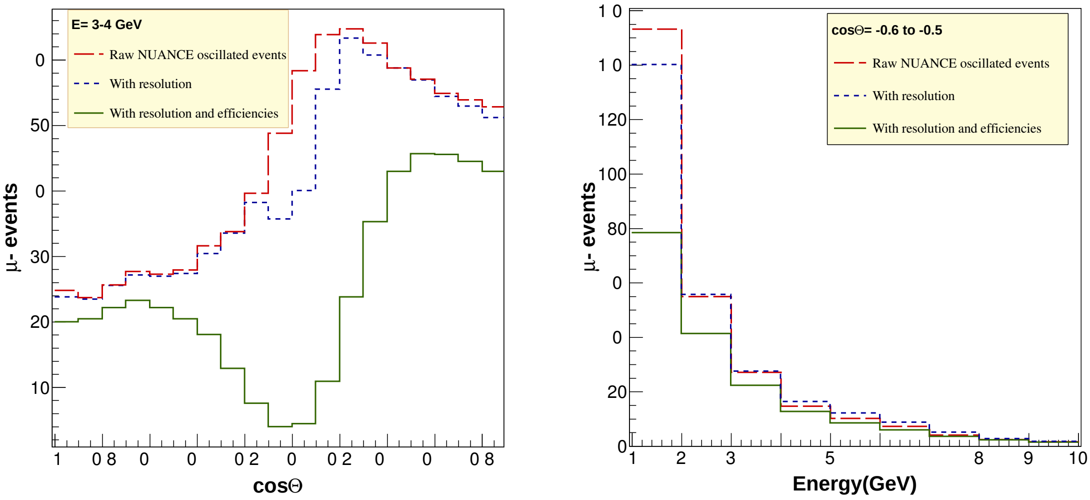

Figure 4.2: The number of μ^- events for 10 years of running of ICAL@INO. The left panel shows the events in zenith angle bins for muon energy range $3-4$ GeV. The right panel shows the energy event spectrum in the zenith bin -0.6 to -0.5. The long-dashed (red) lines are the distribution of μ^- events for NUANCE events on which only the oscillations are imposed. The short-dashed (blue) lines give the zenith angle distribution when we fold the energy and angle resolution on the earlier event spectrum. The solid (green) lines are obtained when in addition to the resolutions we also fold in the efficiencies for muons in ICAL@INO.

obtained by the INO collaboration. The energy and zenith angle resolutions for the muons are in the form of a two-dimensional table. This means that the muon energy resolution is a function of both the muon energy as well as the muon zenith angle. Likewise the muon zenith angle resolution depends on both the muon energy as well as muon zenith angle. The muon detection efficiencies are also dependent on both the energy and zenith angle of the muon. Similarly the charge identification efficiency depends on both the energy and angle of the muon. In Fig. 4.1 we show a snapshot of the efficiencies and resolutions for the μ^- events in ICAL@INO[2]. They are shown as a function of the muon energy for three specific muon zenith angle bins of width 0.1 at $\cos\Theta_T = -0.85$, -0.55 and -0.35. The top-left panel shows the reconstruction efficiency of muons as a function of the muon energy. The top-right panel shows the charge identification efficiency. The bottom-left panel gives the muon zenith angle resolution, while the bottom-right panel shows the muon energy resolution. One can notice that there is a rather strong dependence of all the four quantities on the muon energy as well zenith angle. The reconstruction efficiency, charge identification efficiency and the zenith angle resolution are seen to improve with muon energy. The muon energy resolution on the other hand shows a more complex behavior. While for energies $1-5$ GeV the σ_E/E_T is seen to decrease as energy is increased, thereafter it increases with energy. In the figure the detector performance is seen to be best for $\cos\Theta_T = -0.85$ and worst for $\cos\Theta_T = -0.35$. This is related to the geometry of the ICAL detector wherein there are horizontal slabs of iron and RPCs. As a result, the more horizontal muons travel longer in iron and hit a lesser number of RPCs. Therefore, the detector performs worse for more horizontal bins. In fact, for zenith bins $-0.1 \lesssim \cos\Theta_T \lesssim 0.1$ it becomes extremely difficult to reconstruct the muon tracks and hence for these range of zenith angles the reconstruction efficiency is effectively zero. The efficiencies and resolutions for μ^- and μ^+

---

[2] The detector response to muons used in this work comes from the first set of simulations done with the ICAL code. These simulations are on-going and are being improved. Hence the values of the resolution functions and efficiencies are likely to evolve along with the simulations. More details on this will appear shortly in a separate paper on the detector response to muons from the INO collaboration on the ICAL Geant based simulations.

events in ICAL@INO have been obtained separately from simulations and are found to be similar. We use the separate μ^- and μ^+ efficiencies and resolutions in our simulations and results.

The number of μ^- events in the ij^{th} bin after implementing the efficiencies and resolutions are given

$$N'^{th}_{ij}(\mu^-) = \mathscr{N} \sum_k \sum_l K_i^k(E_T^k)\, M_j^l(\cos\Theta_T^l) \left(\mathscr{E}_{kl}\mathscr{C}_{kl}\, n_{kl}(\mu^-) + \overline{\mathscr{E}}_{kl}(1-\overline{\mathscr{C}_{kl}})\, n_{kl}(\mu^+) \right), \quad (4.1)$$

where $\mathscr{N}$ is the normalization required for a specific exposure in ICAL@INO, E_T and $\cos\Theta_T$ are the true (kinetic) energy and true zenith angle of the muon, while E and $\cos\Theta$ are the corresponding (kinetic) energy and zenith angle reconstructed from the observation of the muon track in the detector. The indices i and j correspond to the measured energy and zenith angle bins while k and l run over the true energy and zenith angle of the muons. The quantities $n_{kl}(\mu^-)$ and $n_{kl}(\mu^+)$ are the number of μ^- and μ^+ events in the k^{th} true energy and l^{th} true zenith angle bin respectively, obtained by folding the raw events from NUANCE with the three-generation oscillation probabilities using the reweighting algorithm and subsequently binning the data as described earlier. The summation is over k and l where k and l scan all true energy and true zenith angle bins respectively. In Eq. (4.1), $\mathscr{E}_{kl}$ and $\overline{\mathscr{E}_{kl}}$ are the reconstruction efficiencies of μ^- and μ^+ respectively, while $\mathscr{C}_{kl}$ and $\overline{\mathscr{C}_{kl}}$ are the corresponding charge identification efficiencies for μ^- and μ^+ respectively, in the k^{th} energy and l^{th} zenith angle bin. Both the reconstruction efficiencies as well as charge identification efficiencies are functions of the true muon energy E_T and true muon zenith angle $\cos\Theta_T$. The quantities K_i^k and M_j^l carry the information regarding the resolution functions of the detector and are seen to be

$$K_i^k(E_T^k) = \int_{E_{L_i}}^{E_{H_i}} dE\, \frac{1}{\sqrt{2\pi}\sigma_E} \exp\left(-\frac{(E_T^k - E)^2}{2\sigma_E^2} \right), \quad (4.2)$$

and

$$M_j^l(\cos\Theta_T^l) = \int_{\cos\Theta_{L_j}}^{\cos\Theta_{H_j}} d\cos\Theta \, \frac{1}{\sqrt{2\pi}\sigma_{\cos\Theta}} \exp\left(-\frac{(\cos\Theta_T^l - \cos\Theta)^2}{2\sigma_{\cos\Theta}^2}\right), \tag{4.3}$$

respectively. The resolution functions are seen to be Gaussian from ICAL simulations above 1 GeV. The resolution functions σ_E and $\sigma_{\cos\Theta}$ are obtained from ICAL simulations and depend on both E_T and $\cos\Theta_T$. A snapshot of these were shown in the lower panels of Fig. 4.1. An expression similar to Eq. (4.1) can we written for the μ^+ events $N_{ij}^{\prime th}(\mu^+)$.

In Fig. 4.2 we show the μ^- event distribution expected in ICAL@INO with 10 years of exposure. In the left panel the events are shown for the energy bin $3-4$ GeV and in $\cos\Theta$ bins of width 0.1. The right panel shows events in the zenith range $\cos\Theta = -0.6$ to -0.5 and in energy bins of width 1 GeV. The red long-dashed lines shows the NUANCE events obtained after including the effect of oscillations according to the reweighting algorithm described above. The oscillation parameters used are given in Table 6.1, with $\sin^2\theta_{23} = 0.5$, $\sin^2 2\theta_{13} = 0.1$ and assuming normal hierarchy. The blue short-dashed lines in the figure are obtained once the oscillated events (red long-dashed lines) in ICAL@INO are folded with the energy and zenith angle resolutions. A comparison of the red long-dashed and blue short-dashed lines in the right panel of the figure reveals that the effect of the energy resolution is to flatten the shape of the energy spectrum. We notice that the blue short-dashed line falls below the red long-dashed line for lower energy bins, while the trend is reversed for the the higher energy bins. On the other hand, the impact of the angle resolution is seen to be negligible for most of the zenith angle bins, as can be seen from from left panel of the figure. The reason for these features can be found in the size of the 1σ width of the resolution functions shown in Fig. 4.1. The energy resolution is seen to be $\sigma_E \simeq 0.15E$ and hence for E between $1-11$ GeV we do expect some spill-over between bins leading to a smearing of the energy spectrum. On the other hand, the bottom right panel of Fig. 4.1 reveals that the $\cos\Theta$ resolution for most of the zenith angle bins are seen to be better than $\cos\Theta \sim 0.01 - 0.02$, while the zenith bins that we have used in the figure are $\Delta\cos\Theta = 0.1$ in width. This is why the smearing due to angle resolution is essentially inconsequential for this choice of zenith angle binning. In chapter 5 we will discuss in detail the impact of bin size on the mass hierarchy sensitivity of ICAL@INO. From a careful and detailed analysis, we will choose an optimal bin size both in energy as well as zenith angle.

The green solid lines in Fig. 4.2 show the realistic events in ICAL@INO where we have taken into account oscillations, detector resolutions as well as reconstruction and charge identification efficiencies. Meaning, these lines are obtained by imposing the reconstruction and charge identification efficiencies on the red short-dashed lines. The left panel shows that once the detector efficiencies are folded, the number of events go to almost zero for the horizontal bins. This happens because of difficulty in reconstructing the muon tracks along the nearly horizontal directions as discussed before.

Fig. 4.3 shows the ICAL@INO μ^- event spectrum in zenith angle bins for four specific muon energy bins of $E = 4-5$ GeV (top left panel), $E = 5-6$ GeV (top right panel), $E = 6-7$ GeV (bottom left panel), and $E = 7-8$ GeV (bottom right panel) and for 10 years exposure. The solid blue lines correspond to $N_i^{\prime th}(\mu^-)$ for the normal hierarchy while red-dashed lines are for the inverted hierarchy. Events were generated at the benchmark oscillation point given in Table 6.1, with $\sin^2\theta_{23} = 0.5$ and $\sin^2 2\theta_{13} = 0.1$. We can see that for normal hierarchy there are earth matter effects in the μ^- channel leading to suppression of the event spectrum. The extent of the suppression is seen to depend on both energy as well as zenith angle bin of the μ^-. The good energy and angle resolution of the detector is crucial here for fine enough binning of the events to extract maximum effect of the earth matter effects. For inverted hierarchy there are no earth matter effects in the μ^- events. On the other hand, for μ^+ earth matter effects appear for inverted hierarchy and are absent for the normal hierarchy. This is why charge separation is so crucial for mass hierarchy determination. If the μ^- and μ^+ events were to be added one would lose sensi-

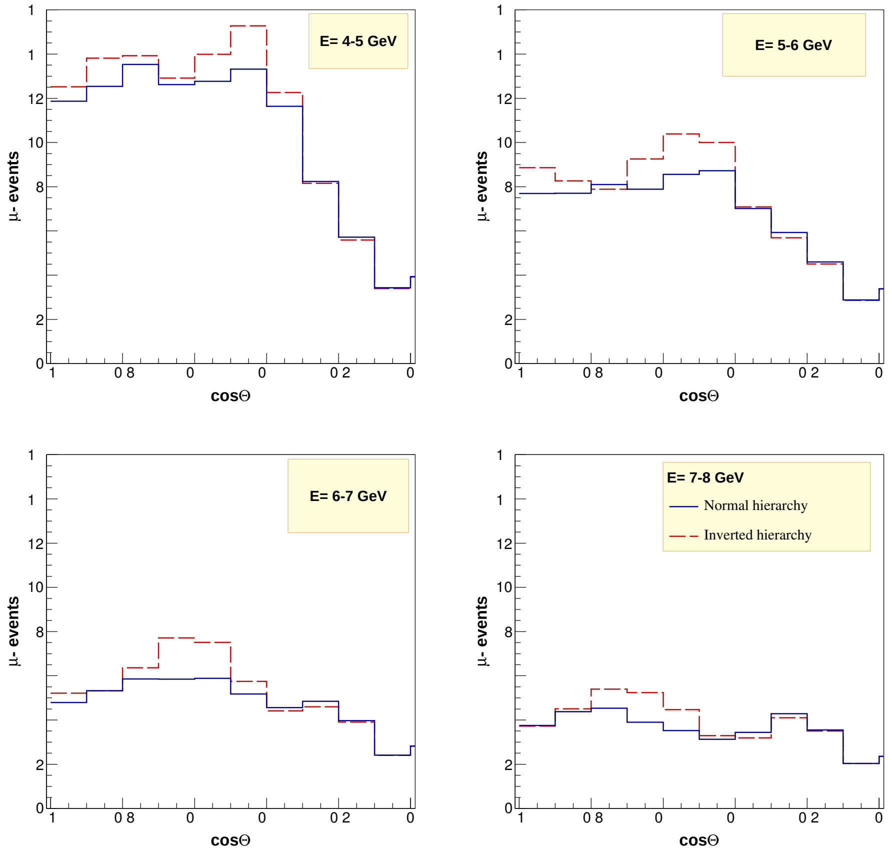

Figure 4.3: ICAL@INO μ^- event spectrum in zenith angle bins for four specific energy bins of $E = 4-5$ GeV (top left panel), $E = 5-6$ GeV (top right panel), $E = 6-7$ GeV (bottom left panel), and $E = 7-8$ GeV (bottom right panel) and for 10 years exposure. The solid blue lines correspond to $N_i'^{th}(\mu^-)$ for normal hierarchy while red-dashed lines are for inverted hierarchy.

tivity to earth matter effects and hence to neutrino mass hierarchy. ICAL@INO will have excellent charge identification capabilities and zenith angle resolution function as well as good energy resolution.

4.4 Statistical Analysis

In what follows, For the χ^2 analysis, we re-bin the data in some chosen energy bin $E = 0.8 - 10.8$ and $\cos\theta$-bins. For doing this statistical test we define a χ^2 for ICAL@INO data as

$$\chi^2_{ino}(\mu^-) = \min_{\{\xi_k\}} \sum_{i=1}^{N_i} \sum_{j=1}^{N_j} \left[2\left(N_{ij}^{th}(\mu^-) - N_{ij}^{ex}(\mu^-) \right) + 2N_{ij}^{ex}(\mu^-) ln \left(\frac{N_{ij}^{ex}(\mu^-)}{N_{ij}^{th}(\mu^-)} \right) \right] + \sum_{k=1}^{l} \xi_k^2 \quad (4.4)$$

where

$$N_{ij}^{th}(\mu^-) = N_{ij}^{\prime th}(\mu^-) \left(1 + \sum_{k=1}^{l} \pi_{ij}^k \xi_k \right) + \mathcal{O}(\xi_k^2) \,. \quad (4.5)$$

We have assumed Poissonian distribution for the errors in this definition of χ^2. The reason is that for the higher energy bins $E \simeq 5 - 10$ GeV where we expect to see the hierarchy sensitivity, the number of events fall sharply (cf. Fig. 4.3) and for small exposure times these bins could have very few events per bin. Since ICAL@INO will have separate data in μ^- and μ^+, we calculate this $\chi^2_{ino}(\mu^-)$ and $\chi^2_{ino}(\mu^+)$ separately for the μ^- sample and the μ^+ sample respectively and then add the two to get the χ^2_{ino} as

$$\chi^2_{ino} = \chi^2_{ino}(\mu^-) + \chi^2_{ino}(\mu^+) \,. \quad (4.6)$$

In the above equations, $N_{ij}^{ex}(\mu^-)$ and $N_{ij}^{ex}(\mu^+)$ are the observed number of μ^- and μ^+ events respectively in the i^{th} energy and j^{th} zenith angle bin and $N_{ij}^{\prime th}(\mu^-)$ and $N_{ij}^{\prime th}(\mu^+)$ are the corresponding theoretically predicted event spectrum given by Eq. (4.1). This predicted event spectrum could shift due to the systematic uncertainties and this shifted spectrum N_{ij}^{th} is given by Eq. (4.5). In the above π_{ij}^{k} is the k^{th} systematic uncertainty in the ij^{th} bin and ξ_k is the pull variable corresponding to the uncertainty π^k. The χ^2_{ino} is minimized over the full set of pull variables $\{\xi_k\}$. The index i runs from 1 to the total number of energy bins N_i and j runs from 1 to total number of zenith angle bins N_j. We will discuss in some detail the impact of binning on the mass hierarchy sensitivity and precision measurement of ICAL@INO in section 5.3. The index k in Eqs. (4.4) and (4.5) runs from 1 to l, where l is the total number of systematic uncertainties. We have included the following five systematic uncertainties in our analysis. An overall flux normalization error of 20% is taken. A 10% error is taken on the overall normalization of the cross-section. A 5% uncertainty on the zenith angle dependence of the fluxes is included. An energy dependent “tilt factor” is considered according to the following prescription. The event spectrum is calculated with the predicted atmospheric neutrino fluxes and then with the flux spectrum shifted according to

$$\Phi_\delta(E) = \Phi_0(E)\left(\frac{E}{E_0}\right)^{\delta} \simeq \Phi_0(E)\left(1+\delta\,\ln\frac{E}{E_0}\right), \tag{4.7}$$

where $E_0 = 2$ GeV and δ is the 1σ systematic error which we have taken as 5%. The difference between the predicted events rates for the two cases is then included in the statistical analysis. Finally, an over all 5% systematic uncertainty is included.

Following the numerical procedure discussed above, we show the sensitivity of ICAL in determining the mass hierarchy, how to improve the mass hierarchy sensitivity for ICAL and also the measurement of oscillation parameters precisely in the next chapters.

CHAPTER 5

MASS HIERARCHY SENSITIVITY OF ICAL@INO

In this chapter, we expound the reach of atmospheric neutrino measurements at ICAL@INO for the determination of the mass hierarchy. Most past works on the mass hierarchy determination with magnetized iron calorimeters performed the analysis in terms of the neutrino energy and zenith angle bins, with some assumed fixed values for the resolutions and efficiencies. In this work, we perform our analysis in terms of the muons, which are binned in reconstructed energy and zenith angle bins. The analysis procedure is described in the chapter 4. In particular, we study the reach of the experiment in pinning down the true neutrino mass hierarchy as a function of the number of years of running of the experiment. We quantitatively show how this sensitivity depends on the uncertainties in the measurement of the other oscillation parameters, especially $|\Delta m^2_{31}|$, θ_{23} and θ_{13}. Since all three of these are expected to be measured to a remarkable precision by the current reactor and accelerator-based long baseline experiments, we include in our analysis the simulated data from the full run of all of these experiments and show the joint sensitivity reach to the neutrino mass hierarchy. We find that while these reactor and accelerator-based neutrino oscillation experiments themselves have very limited sensitivity to the neutrino mass hierarchy, they still have a crucial role to play in this effort, since they constrain $|\Delta m^2_{31}|$, θ_{23} and θ_{13}, which in turn improves the statistical significance with which ICAL@INO can determine the neutrino mass hierarchy. We also show that the reach of ICAL@INO for the neutrino mass hierarchy is nearly independent of δ_{CP}, which at the moment is totally unknown and which is also the hardest amongst all oscillation parameters to be measured. The long baseline experiments, on the other hand are bogged down by the uncertainty in the true value of δ_{CP}, making it difficult to measure the neutrino mass hierarchy from these experiments alone [73]. We show that ICAL@INO will provide a remarkable complementarity in this direction.

This chapter is organized as follows. In section 5.1 we give the benchmark values of neutrino oscillation parameters at which we simulate the projected data used in our analysis. We give the ranges of these parameters over which they are allowed to vary in our statistical fits. In section 5.2 we describe the experimental specifications of the accelerator and reactor experiments Double Chooz, Daya Bay, RENO, T2K, and NOνA used in our analysis for each one of them. In section 5.3, we show the effect of binning on mass hierarchy sensitivity. Next, we present our main results. The impact of systematic uncertainties on the mass hierarchy sensitivity of ICAL@INO is discussed in section 5.5 and that of the true value of θ_{23} is studied in section 5.6. In section 5.7 we explore the effect of δ_{CP} value on the mass hierarchy sensitivity in ICAL@INO and NOνA.

5.1 Oscillation parameters

With neutrino physics entering the precision era, it has become very important to define what is meant by the atmospheric neutrino mass splitting when one is doing a three-

Parameter	True value used in data	3σ range used in fit
Δm^2_{21}	7.5×10^{-5} eV^2	$[7.0-8.0] \times 10^{-5}$ eV^2
$\sin^2\theta_{12}$	0.3	$[0.265-0.33]$
$\lvert\Delta m^2_{\rm eff}\rvert$	2.4×10^{-3} eV^2	$[2.1-2.6] \times 10^{-3}$ eV^2
δ_{CP}	0	$[0-2\pi]$
$\sin^2\theta_{23}$	0.4, 0.5, 0.6	$\sin^2\theta_{23}$(true)± 0.1
$\sin^2 2\theta_{13}$	0.08, 0.1, 0.12	$\sin^2 2\theta_{13}$(true)± 0.03

Table 5.1: Benchmark true values of oscillation parameters used in the simulations, unless otherwise stated. The range over which they are allowed to vary freely in the fit is also shown in the last column. For $\sin^2\theta_{23}$(true) and $\sin^2 2\theta_{13}$(true) we use three benchmark values for simulating the data.

generation fit. The subtlety involved is the following. The value of the best-fit for the atmospheric mass squared difference depends on the mass hierarchy and definition used. In particular, it could be rather misleading to use an inconsistent definition for this parameter when doing mass hierarchy studies. For instance, if Δm^2_{31} is called the atmospheric neutrino mass squared difference and $\Delta m^2_{31} > 0$ defined as normal hierarchy, then the absolute value of Δm^2_{32} changes when one changes the hierarchy from normal ($\Delta m^2_{31} > 0$) to inverted ($\Delta m^2_{31} < 0$). Since the three generation oscillation probability is sensitive to all oscillation frequencies, in this case one gets a rather large difference in the survival probability $P_{\nu_\mu\nu_\mu}$ between normal and inverted hierarchies even when θ_{13} is taken as zero and there are no θ_{13} driven earth matter effects. One needs to perform a careful marginalization over Δm^2_{31} in this case to get rid of the spurious difference in $P_{\nu_\mu\nu_\mu}$ coming from this effect [74]. Therefore, it is important to use a consistent definition for the mass squared difference in the analysis, especially in studies pertaining to observations of earth matter effects. In our study we use as the atmospheric mass squared difference, the quantity defined as [75]

$$\Delta m^2_{\rm eff} = \Delta m^2_{31} - (\cos^2\theta_{12} - \cos\delta_{CP}\sin\theta_{13}\sin 2\theta_{12}\tan\theta_{23})\Delta m^2_{21}\,, \qquad (5.1)$$

where the other parameters are defined according to the convention used by the PDG. The normal hierarchy is then defined as $\Delta m^2_{\text{eff}} > 0$ and the inverted hierarchy as $\Delta m^2_{\text{eff}} < 0$. Defining the mass squared difference by Eq. (5.1) is particularly convenient for mass hierarchy studies involving the probability $P_{\nu_\mu \nu_\mu}$ since it is almost same for $\Delta m^2_{\text{eff}} > 0$ (normal hierarchy) and $\Delta m^2_{\text{eff}} < 0$ (inverted hierarchy) for $\theta_{13} = 0$. This ensures that there is no spurious contribution to the mass hierarchy sensitivity coming from the difference between the oscillation frequencies for the normal and inverted hierarchies in experiments predominantly sensitive to the oscillation channel $P_{\nu_\mu \nu_\mu}$. However for this definition of the mass hierarchy, there is a difference between the frequencies involved in normal and inverted ordering for the other oscillation channels and marginalizing over Δm^2_{eff} then becomes very important for them. In our analysis we have paid special attention to the marginalizing procedure and have checked our mass hierarchy sensitivity to the definition used for the atmospheric mass squared difference and the mass hierarchy. We will quantify this issue later.

Our analysis in this paper uses the full three generation oscillation probabilities without any approximations. The data are simulated at a particular set of benchmark values chosen for the oscillation parameters, which we call “true value”. These are summarized in Table 5.1. The true values of Δm^2_{21}, $\sin^2\theta_{12}$ and $|\Delta m^2_{\text{eff}}|$ are kept fixed throughout the paper. These quantities are now fairly well determined by the current global neutrino data and we choose our benchmark true values for these parameters to be close to their current best-fits, as discussed above. We will show results for a range of plausible values of $\sin^2\theta_{23}$(true) and $\sin^2 2\theta_{13}$(true) since the earth matter effects are fairly sensitive to these parameters. While we have absolutely no knowledge on the value of δ_{CP}(true), the sensitivity of ICAL@INO does not depend much on the true value of this parameter. Therefore, δ_{CP}(true) is also kept fixed at zero, unless otherwise stated. Only in section 8, where we study the impact of δ_{CP}(true) on the mass hierarchy reach of the NOνA experiment, will we show results as a function of the δ_{CP}(true).

In our fit, we allow the oscillation parameters to vary freely within their current 3σ limits and the χ^2 is minimized (marginalized) over them. The range over which these parameters are varied in the fit is also shown in Table 5.1. Since the ICAL@INO sensitivity does not depend much on Δm^2_{21}, $\sin^2\theta_{12}$ and δ_{CP}, we keep these fixed at their true values in the fit for the analysis of the ICAL@INO data. However, the ICAL@INO sensitivity to the mass hierarchy does depend on $|\Delta m^2_{\rm eff}|$, $\sin^2\theta_{23}$ and $\sin^2 2\theta_{13}$ and hence the χ^2_{ino} is marginalized over the 3σ ranges of these parameters. The combined χ^2 for the accelerator and reactor experiments depends on all the oscillation parameters, and so for them we marginalize the χ^2 over the current 3σ range of all the oscillation parameters. Since the range of $|\Delta m^2_{\rm eff}|$, $\sin^2\theta_{23}$ and $\sin^2 2\theta_{13}$ will be severely constrained by the future accelerator and reactor data themselves, the best-fit for these in our global fits are mostly close to the true value taken for the data. However, none of the data sets included in our analysis has the potential to constrain Δm^2_{21} and $\sin^2\theta_{12}$. Therefore, in order to take into account the fact that not all values of Δm^2_{21} and $\sin^2\theta_{12}$ within their current 3σ range are allowed with equal probability by the solar and KamLAND data, we impose a “prior” according to the following definition:

$$\chi^2_{prior} = \sum_i \left(\frac{p_i^{fit} - p_i^{true}}{\sigma_{p_i}} \right)^2 , \tag{5.2}$$

where the parameter p_i is Δm^2_{21} and $\sin^2\theta_{12}$ for $i = 1$ and 2 respectively, with $\sigma_{\Delta m^2_{21}} = 3\%$ and $\sigma_{\sin^2\theta_{12}} = 4\%$. This χ^2_{prior} is added to the sum of the χ^2 obtained from the analysis of the ICAL@INO simulated data and the prospective accelerator and reactor data, and the combined χ^2 is then marginalized over all oscillation parameters.

5.2 Simulation of the current reactor and accelerator-based experiments

For simulation of the current reactor and accelerator-based experiments we use the GLoBES software [76]. We have closely followed [73] for the analysis of the future accelerator and reactor data. The experiments that we include in our study are namely Double Chooz, RENO, DayaBay as reactor experiments and T2K, NOνA as accelerator based experiments. The basic informations about these experiments have been given in chapter 1.

- **Double Chooz:** Following [73], we perform the analysis for an exposure of 3 years with both near and far detectors fully operational and with detector efficiency of 80% and reactor load factor of 78%. An uncorrelated systematic uncertainty of 0.6% is assumed.

- **RENO:** The first data set from this experiment was released in March 2012 [11] confirming that θ_{13} was indeed non-zero at 4.9σ C.L.. We consider in our analysis simulated data with 3 years of full run for the RENO experiment and include an uncorrelated systematic uncertainty of 0.5% which is the projected benchmark systematic uncertainty for RENO [46].

- **Daya Bay:** The experiment has been running with 6 detectors and so far produced outstanding results [10, 46]. We analyze simulated data corresponding to 3 years of full run for the Daya Bay experiment and consider an uncorrelated systematic uncertainty of 0.18% which is the projected systematic uncertainty for Daya Bay.

- **T2K:** The beam power used for the simulation of T2K experiment is taken to be 0.75 MW with 5 years of neutrino running.

- **NOνA:** The beam power used for the simulation of NOνA experiment is 0.7 MW with 3 years of running in the neutrino and 3 in the antineutrino mode.

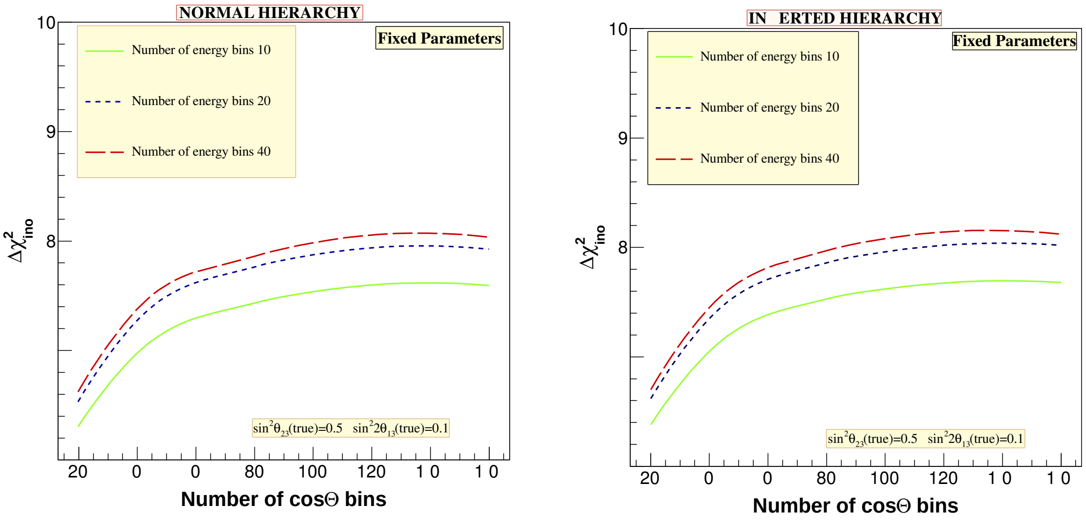

Figure 5.1: Effect of binning on the mass hierarchy reach of ICAL@INO with 10 years data.

5.3 Mass Hierarchy Sensitivity – Effect of Binning

The earth matter effect in atmospheric neutrinos is known to fluctuate rapidly with energy as well as zenith angle. Therefore, one would like to observe the difference in energy and zenith angle spectrum between the μ^- and μ^+ as accurately as possible. Since averaging of data in energy and/or zenith angle bins is expected to reduce the sensitivity of the experiment to earth matter effect and hence to the neutrino mass hierarchy, one would ideally like to perform an unbinned likelihood analysis of the ICAL@INO data. This will obviously be the approach once the real data of ICAL@INO is available. However, at this stage we can only perform a binned χ^2 analysis of the simulated ICAL@INO data. In the following, we begin by first analyzing the effect of bin size on the mass hierarchy sensitivity of ICAL@INO and choose the optimum bin sizes in energy and zenith angle of the muons.

In Fig. 5.1 we show the effect of bin size on the mass hierarchy sensitivity of ICAL@INO. The ICAL@INO data used in this figure corresponds to 10 years of running of the experiment and is generated at the benchmark values of the oscillation given in Table 5.1 and for $\sin^2 2\theta_{13} = 0.1$ and $\sin^2\theta_{23} = 0.5$. Since our main objective here is to look at the impact of bin size on the mass hierarchy sensitivity, we do not bring in the complication of marginalization over the oscillation parameters and keep all oscillation parameters fixed at their true values in the fit. We show the χ^2_{ino} obtained as a function of the number of bins in $\cos\Theta$, where the zenith angle $\cos\Theta$ ranges between -1 and $+1$. The left panel is for normal hierarchy taken as true while the right panel is for true inverted hierarchy. The three lines in each of the panels are for three different choice for the number of energy bins. The solid green lines are for 10 energy bins, the dashed blue lines for 20 energy bins while the long-dashed red lines correspond to 40 energy bins. The range of measured muon energy considered in each case is between 1 GeV and 11 GeV. We notice that the χ^2_{ino} increases as the number of $\cos\Theta$ bins is increased from 20 and eventually flattens out beyond 80. Likewise the sensitivity is seen to increase as we increase the number of energy bins. However, there is no substantial gain beyond the case for 20 energy bins. This trend agrees well with the ICAL@INO resolutions obtained in energy and $\cos\Theta$, a snapshot of which is reported in Fig. 4.1. The $\cos\Theta$ resolution $\sigma_{\cos\Theta} \sim 0.025$ which corresponds to 80 bins, while energy resolution at $E_\mu \simeq 5$ GeV is seen to be $\sigma_E \sim 0.1$ which is compatible with energy bin size of 0.5 GeV with 20 energy bins. Therefore, in the rest of the this paper, we work with 20 energy and 80 $\cos\Theta$ bins.

5.4 Mass Hierarchy Sensitivity – Main Results

In Fig. 5.2 we show the discovery potential of ICAL@INO alone for the neutrino mass hierarchy, as a function of the number of years of running of the experiment. The data is generated for the values of the oscillation parameters given in Table 6.1 and for $\sin^2\theta_{23}(\text{true}) = 0.5$. The three lines correspond to the different values of $\sin^2 2\theta_{13}(\text{true})$ shown in the legend boxes in the figure, which we have chosen around the best-fit and 2σ [1] range of the current

---

[1] Here the wrong hierarchy is excluded at a $\sqrt{\Delta\chi^2}\sigma$ level. However, Qian *et al.*, Ciuffoli *et al.*, have pointed out that, as the hierarchy is a discrete choice, $\Delta\chi^2$ does not obey a one degree of freedom χ^2 distribution and therefore it is not correct to use $\sqrt{\Delta\chi^2}$ to evaluate the confidence level. A detailed discussion can be found in the papers [47, 48, 49].

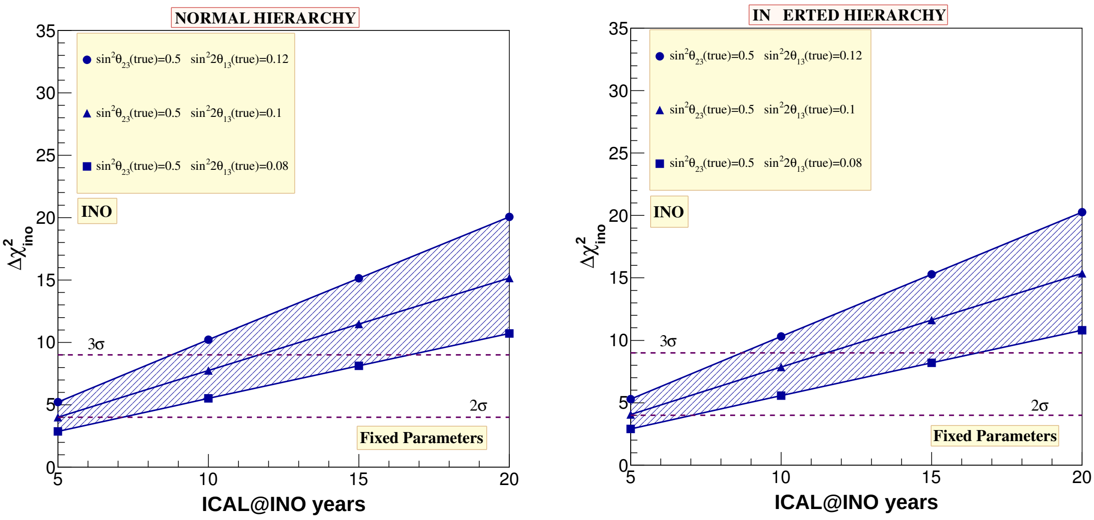

Figure 5.2: Left panel shows the $\Delta\chi^2_{ino}$ for the wrong hierarchy when normal hierarchy is taken to be true, while the right panel shows the corresponding reach when inverted hierarchy is taken as true. The three lines are for three different values of $\sin^2 2\theta_{13}(\text{true}) = 0.08$, 0.1 and 0.12 as shown in the legend box, while $\sin^2\theta_{23}(\text{true}) = 0.5$ for all cases. We take only ICAL@INO data into the analysis and in the fit keep all oscillation parameters fixed at their benchmark true values.

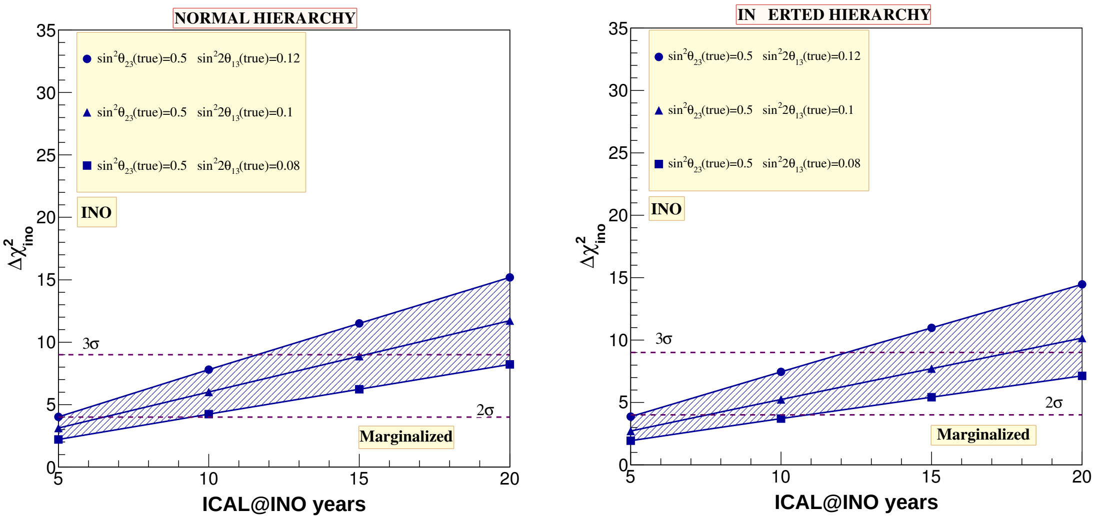

Figure 5.3: Same as Fig. 5.2 but here oscillation parameters $|\Delta m^2_{\text{eff}}|$, $\sin^2\theta_{23}$ and $\sin^2 2\theta_{13}$ are allowed to vary freely within their current 3σ ranges given in Table 6.1.

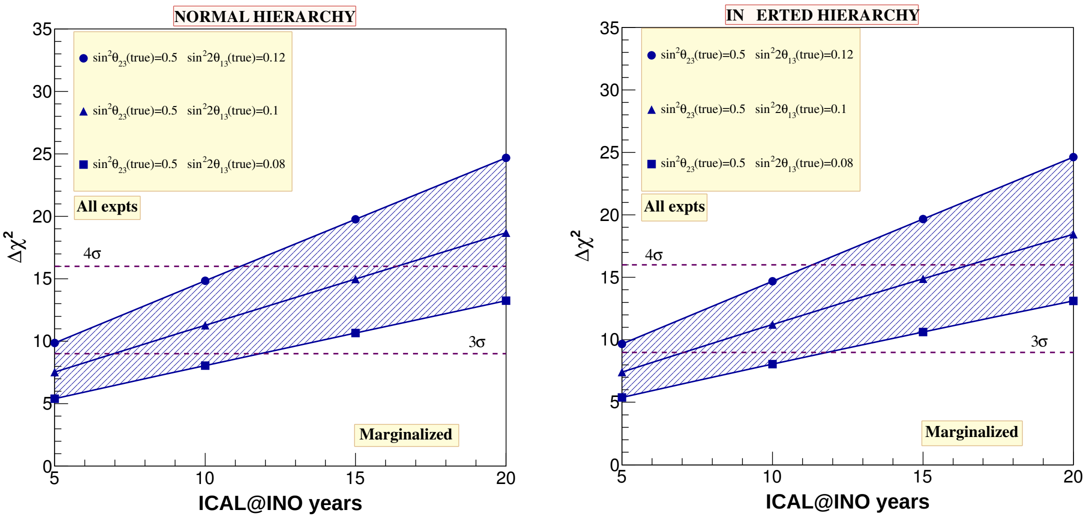

Figure 5.4: The $\Delta\chi^2$ for the wrong hierarchy obtained from a combined analysis of all experiments including ICAL@INO as well NOνA, T2K, Double Chooz, RENO and Daya Bay experiments. The left panel is for normal hierarchy taken as true in the data while the right panel is for inverted hierarchy as true. The three lines are for three different values of $\sin^2 2\theta_{13}(\text{true}) = 0.08$, 0.1 and 0.12 as shown in the legend box, while $\sin^2\theta_{23}(\text{true}) = 0.5$ for all cases. In the fit we allow all parameters to vary within their 3σ ranges as shown in Table 6.1.

best-fit. The left-hand panel is for true normal hierarchy while the right-hand panel is for true inverted hierarchy. These plots show the sensitivity reach of ICAL@INO when all oscillation parameters are kept fixed in the fit at the values at which the data was generated. For $\sin^2 2\theta_{13}(\text{true})$ around the current best-fit of 0.1, we can note from the these plots that with 5 years of ICAL@INO data alone, we will have a 2.0σ (2.0σ) signal for the wrong hierarchy if normal (inverted) hierarchy is true. After 10 years of ICAL@INO data, this will improve to 2.8σ (2.8σ) signal for the wrong hierarchy if normal (inverted) hierarchy is true. The sensitivity obviously increases with the true value of $\sin^2 2\theta_{13}(\text{true})$. The $\Delta\chi^2$ is seen to increase almost linearly with exposure. This is not hard to understand as the hierarchy sensitivity comes from the difference in the number of events between normal and inverted hierarchies due to earth matter effects. Since this is a small difference, the relevant statistics in this measurement is small. As a result the mass hierarchy analysis is statistics dominated and one can see from Eq. (4.6) that in the statistics dominated regime the $\Delta\chi^2_{ino}$

increases linearly with exposure.

The hierarchy sensitivity quoted above are for fixed values of the oscillation parameters. This effectively means that the values of all oscillation parameters are known with infinite precision. Since this is not the case, the sensitivity will go down once we take into account the uncertainty in the value of the oscillation parameters. The oscillation parameters which affect the mass hierarchy sensitivity of ICAL@INO the most are $|\Delta m^2_{\rm eff}|$, $\sin^2\theta_{23}$ and $\sin^2 2\theta_{13}$. In Fig. 5.3 we show the mass hierarchy sensitivity reach of ICAL@INO with full marginalization over the oscillation parameters $|\Delta m^2_{\rm eff}|$, $\sin^2\theta_{23}$ and $\sin^2 2\theta_{13}$, meaning these oscillation parameters are allowed to vary freely in the fit within their *current* 3σ ranges, and the minimum of the χ^2 taken from that. The CP phase δ_{CP} does not significantly impact the ICAL@INO mass hierarchy sensitivity. This will be discussed in some detail later. Therefore, we keep δ_{CP} fixed at 0 in the fit. The parameters Δm^2_{21} and $\sin^2\theta_{12}$ also do not affect χ^2_{ino} and hence are kept fixed at their true values given in Table 6.1. From the figure we see that for full marginalization within the *current* 3σ allowed range for $|\Delta m^2_{\rm eff}|$, $\sin^2\theta_{23}$ and $\sin^2 2\theta_{13}$, the sensitivity reach of ICAL@INO with 10 (5) years data would drop to 2.5σ (1.8σ) for $\sin^2\theta_{23}(\text{true}) = 0.5$ and $\sin^2 2\theta_{13}(\text{true}) = 0.1$, for true normal hierarchy. The impact for the inverted hierarchy case is seen to be more. However, this is not a fair way of assessing the sensitivity reach of the experiment since all values of the oscillation parameters are not allowed with equal C.L. by the current data. This implies that when they deviate from their current best-fit value in the fit, they should pick up a χ^2 from the data of the experiment(s) which constrains them. Therefore, one should do a global fit taking all relevant data into account to find the correct estimate of the reach of combined neutrino data to the neutrino mass hierarchy. One way to take this into account is by introducing priors on the parameters and adding the additional χ^2_{prior} in the fit, analogous to what we had explained in Eq. (5.2) and the related discussion for the priors on the solar parameters. Moreover, all oscillation parameters are expected to be measured with much better precision by the on-going and up-coming neutrino experiments. In fact, by the time

ICAL@INO is operational, all of the current accelerator-based and reactor experiments would have completed their scheduled run and hence we expect that by then significant improvements in the allowed ranges of the oscillation parameters would have been made. In particular, we expect improvement in the values of $\sin^2 2\theta_{13}$, $|\Delta m^2_{\rm eff}|$ and $\sin^2 2\theta_{23}$ from the data coming from current accelerator and reactor experiments. A projected combined sensitivity analysis of these experiments shows that the 1σ uncertainties on the values of $\sin^2 2\theta_{13}$, $|\Delta m^2_{\rm eff}|$ and $\sin^2 2\theta_{23}$ are expected to go down to 0.1%, 2% and 0.65%, respectively [73]. Since marginalization over these parameters makes a difference to χ^2_{ino} for the wrong hierarchy (cf. Figs. 5.2 and 5.3), better measurement on them from the current experiments will therefore improve the mass hierarchy sensitivity reach of ICAL@INO. As mentioned before, one could incorporate this information into the analysis by including "priors" on these parameters. The sensitivity reach of ICAL@INO with projected priors on $|\Delta m^2_{\rm eff}|$ and $\sin^2 2\theta_{23}$ keeping other parameters fixed can be found in [77]. In the plot presented in [77] 1σ prior of 2% on $|\Delta m^2_{\rm eff}|$ and 0.65% on $\sin^2 2\theta_{23}$ was assumed. Note however, that in that analysis only two systematic uncertainties were included in the fit, an overall flux normalization uncertainty of 20% and an overall cross-section uncertainty of 10%. We will discuss the impact of systematic uncertainties again in section 5.5. In this work we improve the analysis by performing a complete global fit of the atmospheric neutrino data at ICAL@INO combined with all relevant data which would be available at that time, *viz.*, data from the full run of the T2K, NOνA, Double Chooz, Daya Bay, and RENO experiments. The combined sensitivity to the neutrino mass hierarchy as a function of number of years of run of the ICAL@INO atmospheric neutrino experiment is shown in Fig. 5.4. For each set of oscillation parameters, the joint χ^2 from all experiments is given by

$$\chi^2 = \chi^2_{ino} + \sum_i \chi^2_i \tag{5.3}$$

where $\sum_i \chi_i^2$ is the contribution from the accelerator and reactor experiments and i runs over T2K, NOνA, Double Chooz, Daya Bay, and RENO experiments. This joint χ^2 is computed and marginalized over all oscillation parameters. The minimized joint $\Delta\chi^2$ is shown in Fig. 5.4. We reiterate that the $x-$axis in this figure shows the number of years of running of ICAL@INO only, while for all other experiments we have considered their complete run as planned in their letter of intent and/or Detailed Project Report, as mentioned in section 5.2. The left panel of the figure shows the sensitivity reach if normal hierarchy is true while the right panel shows the reach when the inverted hierarchy is the true hierarchy. As in Figs. 5.2 and 5.3 we generate the data at the values of the oscillation parameters given in Table 6.1 and with $\sin^2\theta_{23}(\text{true}) = 0.5$ and three different values of $\sin^2 2\theta_{13}(\text{true}) = 0.08$, 0.1, and 0.12. The figure shows that inclusion of the accelerator and reactor data increases the sensitivity such that with just 5 years of ICAL@INO data one would have more than 2σ evidence for the neutrino mass hierarchy even if $\sin^2 2\theta_{13}(\text{true}) = 0.08$. For the current best-fit of $\sin^2 2\theta_{13}(\text{true}) = 0.1$ we would rule out the wrong hierarchy at 2.7σ while for larger $\sin^2 2\theta_{13}(\text{true}) = 0.12$ mass hierarchy could be determined with about 3.1σ C.L.. With 10 years of ICAL@INO data the sensitivity would improve to 2.8σ for $\sin^2 2\theta_{13}(\text{true}) = 0.08$, 3.4σ for $\sin^2 2\theta_{13}(\text{true}) = 0.1$ and 3.9σ for $\sin^2 2\theta_{13}(\text{true}) = 0.12$.

The inclusion of the accelerator and reactor experiments into the analysis improves the sensitivity reach to the neutrino mass hierarchy in the following two ways. Firstly, inclusion of these data sets into the analysis effectively restricts the allowed ranges of oscillation parameters $|\Delta m^2_{\text{eff}}|$, $\sin^2\theta_{23}$ and $\sin^2 2\theta_{13}$ such that the statistical significance of the mass hierarchy determination from ICAL@INO alone goes up to what we were getting in Fig. 5.2 for fixed values of the oscillation parameters. In addition, we also get a contribution to the mass hierarchy sensitivity from the accelerator and reactor experiments themselves.

We show in Table 5.2 the separate contributions from the individual experiments to the statistical significance for the mass hierarchy sensitivity from the global fit. The data

Expts	NOvA	T2K	DB	RENO	DC	INO	ALL
$\Delta\chi^2_{\Delta m^2_{\mathrm{eff}}}$	2.59	0.26	0.53	0.12	0.02	7.76	11.28
$\Delta\chi^2_{\Delta m^2_{31}}$	2.49	0.31	0.63	0.14	0.02	7.95	11.53

Table 5.2: Contribution to the $\Delta\chi^2$ towards the wrong mass hierarchy at the global best-fit from the individual experiments. The normal hierarchy was taken as true and data was generated at the benchmark true values of the oscillation parameters given in Table 6.1 with $\sin^2\theta_{23}(\mathrm{true}) = 0.5$ and $\sin^2 2\theta_{13}(\mathrm{true}) = 0.1$. The first row ($\Delta\chi^2_{\Delta m^2_{\mathrm{eff}}}$) shows the individual contributions to the statistical significance when $\Delta m^2_{\mathrm{eff}}$ is used for defining the normal ($\Delta m^2_{\mathrm{eff}} > 0$) and inverted ($\Delta m^2_{\mathrm{eff}} < 0$) mass hierarchy, while the lower row ($\Delta\chi^2_{\Delta m^2_{31}}$) gives the corresponding contributions when $\Delta m^2_{31} > 0$ is taken as normal hierarchy and $\Delta m^2_{31} < 0$ as inverted hierarchy. Effect of choice of the definition for normal and inverted hierarchy will be discussed in the Appendix.

is generated for normal hierarchy and the benchmark true values of the oscillation parameters given in Table 6.1 with $\sin^2\theta_{23}(\mathrm{true}) = 0.5$ and $\sin^2 2\theta_{13}(\mathrm{true}) = 0.1$. The oscillation parameters are allowed to vary freely in the fit and the minimum global χ^2 selected. The Table 5.2 shows the individual $\Delta\chi^2$ contributions from each experiment at this global best-fit point for the oscillation parameters, as well as the combined $\Delta\chi^2$. The global best-fit for the inverted hierarchy corresponds to $\Delta m^2_{21} = 7.5\times10^{-5}$ eV^2, $\sin^2\theta_{12} = 0.31$, $\sin^2\theta_{23} = 0.5$, $\sin^2 2\theta_{13} = 0.1$, $\Delta m^2_{\mathrm{eff}} = -2.4\times10^{-3}$ eV^2 and $\delta_{CP} = 252^\circ$. Note that (cf. Eq. (5.1)) since Δm^2_{31} depends on the value of δ_{CP}, the change of δ_{CP} in the fit gives $|\Delta m^2_{31}| = 2.34\times10^{-3}$ eV^2 at the global best-fit for the inverted hierarchy ($\Delta m^2_{\mathrm{eff}} < 0$). However, the data was generated at $\Delta m^2_{\mathrm{eff}} = +2.4\times10^{-3}$ eV^2, which for $\delta_{CP}(\mathrm{true}) = 0^\circ$ gives $|\Delta m^2_{31}| = 2.44\times10^{-3}$ eV^2.

Table 5.2 shows that it is mainly ICAL@INO and NOνA which contribute to the $\Delta\chi^2$ since reactor experiments have no sensitivity to the neutrino mass hierarchy and the baseline for T2K is far too short to allow for any significant earth matter effect in the signal. The NOνA experiment on the other hand has a baseline of 810 km and a higher energy neutrino beam. This gives the experiment sizable earth matter effects which in turn brings in sensitivity to the neutrino mass hierarchy. The small $\Delta\chi^2$ contribution from the reactor experiments comes from the fact that the best-fit value of the oscillation parameters, and in particular $|\Delta m^2_{31}|$ which controls the spectral shape of these experiments is slightly different at the global best-fit for inverted hierarchy, as discussed above. The T2K experiment on the other hand returns a small contribution since the best-fit δ_{CP} is different from $\delta_{CP}(\text{true}) = 0$ taken in data.

The first row of Table 5.2 shows the χ^2 for the case used in this analysis where normal hierarchy is defined as $\Delta m^2_{\text{eff}} > 0$ and inverted hierarchy is defined as $\Delta m^2_{\text{eff}} < 0$. In this case the survival probability $P_{\nu_\mu\nu_\mu}$ is almost the same for the normal and inverted hierarchies so defined. However, this is not true for the channels $P_{\mu e}$ relevant for T2K and NOvA and P_{ee} relevant for the reactor experiments. Thus in the best-fit the value of Δm^2_{eff} has to be suitably adjusted so that the oscillation frequencies in these oscillation channels are closest to each other in the data and in the fit. This results in a small χ^2 from experiments that do not have any hierarchy sensitivity at all. We have checked indeed that the χ^2 for mass hierarchy is zero for all reactor experiments and T2K. Only when one performs a combined does this tension between choice of the oscillation frequencies crops up, returning a small contribution to the mass hierarchy from the reactor experiments and T2K.

In order to check the impact of our choice of $\Delta m^2_{\text{eff}} > 0$ ($\Delta m^2_{\text{eff}} < 0$) as normal (inverted) hierarchy, we repeated our global fit by taking $\Delta m^2_{31} > 0$ as the definition for normal hierarchy and $\Delta m^2_{31} < 0$ as the definition for inverted hierarchy. The results for this case is shown in the second row of Table 5.2. One can see that there is hardly any impact of the definition of mass hierarchy on our final results.

The results in this section including those shown in Table 5.2 are for $\delta_{CP}(\text{true})=0$. However, the accelerator-based long baseline experiments are sensitive to the $\nu_\mu \to \nu_e$ oscillation channel. The size of this $P_{\nu_\mu\nu_e}$ oscillation probability and the resultant sensitivity depends crucially on the CP phase δ_{CP}. Therefore, the contribution from NOvA to the statistical significance with which we can determine the neutrino mass hierarchy will depend

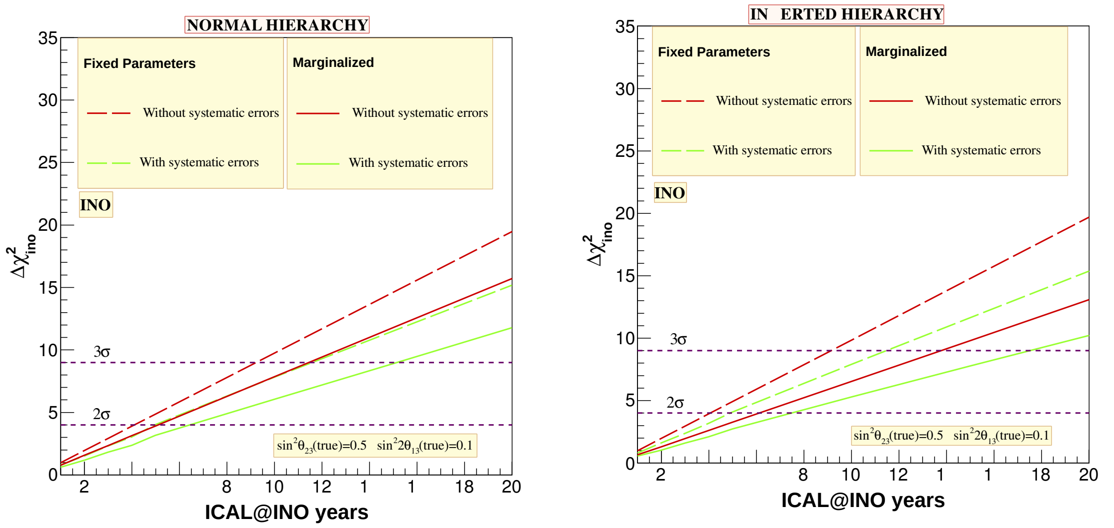

Figure 5.5: The impact of systematic uncertainties on mass hierarchy sensitivity. The red lines are obtained without taking systematic uncertainties in the ICAL@INO analysis, while the green lines are obtained when systematic uncertainties are included. Long-dashed lines are for fixed parameters in theory as in data, while solid lines are obtained by marginalizing over $|\Delta m^2_{\rm eff}|$, $\sin^2\theta_{23}$ and $\sin^2 2\theta_{13}$.

crucially on the value of δ_{CP}(true). We will discuss this in some detail in section 5.7.

5.5 Impact of systematic uncertainties

The atmospheric neutrino fluxes have large systematic uncertainties. In order to study the impact of these systematic uncertainties on the projected reach of ICAL@INO to the neutrino mass hierarchy, we show in Fig. 5.5 the mass hierarchy sensitivity with and without systematic uncertainties in the ICAL@INO analysis. The $\Delta\chi^2$ is shown as a function of the number of years of exposure of the experiment. The data was generated at the benchmark oscillation point. The red lines are obtained without taking systematic uncertainties in the ICAL@INO analysis, while the green lines are obtained when systematic uncertainties are included. The long-dashed lines are for fixed parameters in theory as in the data, while the solid lines are obtained by marginalizing over $|\Delta m^2_{\rm eff}|$, $\sin^2\theta_{23}$ and $\sin^2 2\theta_{13}$. The left panel is for true normal hierarchy while the right panel is for true inverted hierarchy. The effect of taking systematic uncertainties is to reduce the statistical significance of the analysis. We have checked that of the five systematic uncertainties, the uncertainty on overall normalization of the fluxes and the cross-section normalization uncertainty have minimal impact on the final results. The reason for that can be understood from the fact that the atmospheric neutrinos come from all zenith angles and over a wide range of energies. The overall normalization uncertainty is the same for all bins, while the mass hierarchy dependent earth matter effects, are important only in certain zenith angle bin and certain range of energies. Therefore, the effect of the overall normalization errors get cancelled between different bins. On the other hand, the tilt error could be used to modify the energy spectrum of the muons in the fit and the zenith angle error allows changes to the zenith angle distribution. Therefore, these errors do not cancel between the different bins and can dilute the significance of the data. In particular, we have checked that the effect of the zenith angle dependent systematic error on the atmospheric neutrino fluxes has the maximum effect on the lowering of the $\Delta\chi^2$ for the mass hierarchy sensitivity.

5.6 Impact of $\sin^2\theta_{23}$(true)

It is well known that the amount of earth matter effects increases with increase in both θ_{13} and θ_{23}. In the previous plots, we showed the mass hierarchy sensitivity for different allowed values of $\sin^2 2\theta_{13}$(true), while $\sin^2\theta_{23}$(true) was fixed at maximal mixing. In Figs. 5.6 and 5.7 we show the sensitivity to the neutrino mass hierarchy as a function of number of years of running of ICAL@INO for different values of $\sin^2 2\theta_{13}$(true) as well as $\sin^2\theta_{23}$(true). In Fig. 5.6 we show the $\Delta\chi^2$ corresponding to ICAL@INO alone and with oscillation parameters fixed in the fit at their true values. This figure corresponds to Fig. 5.2 of the previous section but now with two other values of $\sin^2\theta_{23}$(true). In Fig. 5.7 we give the combined sensitivity to mass hierarchy of all accelerator and reactor experiments combined with the data of ICAL@INO. We reiterate that the x-axis of the Fig. 5.7 shows

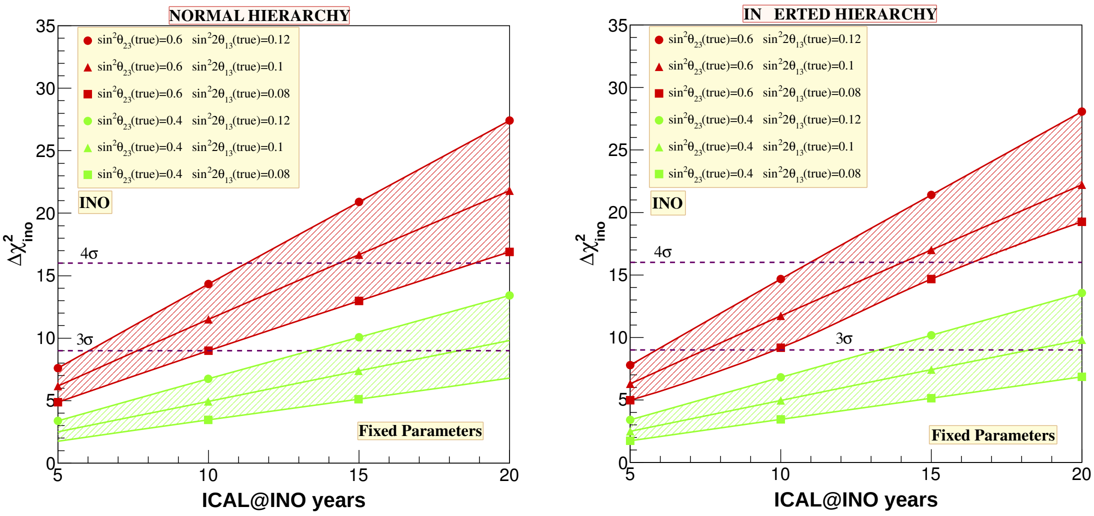

Figure 5.6: Same as Fig. 5.2 but for $\sin^2\theta_{23}(\text{true}) = 0.4$ (green band) and $\sin^2\theta_{23}(\text{true}) = 0.6$ (red band).

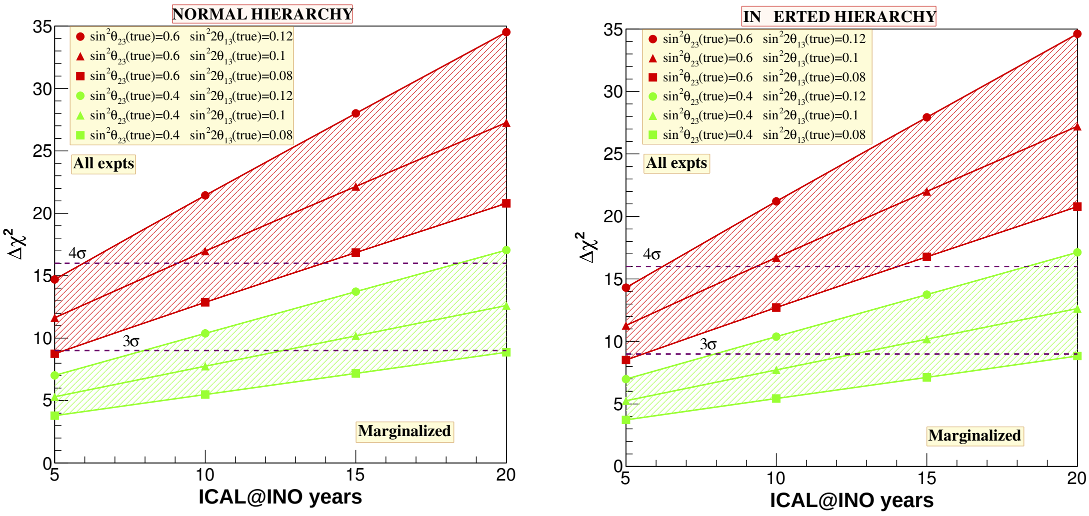

Figure 5.7: Same as Fig. 5.4 but for $\sin^2\theta_{23}(\text{true}) = 0.4$ (green band) and $\sin^2\theta_{23}(\text{true}) = 0.6$ (red band).

the exposure of ICAL@INO, while for all other experiments we have assumed the full run time as discussed in section 5.2. The red bands in Figs. 5.6 and 5.7 correspond to $\sin^2\theta_{23}(\text{true}) = 0.6$ while the green bands are for $\sin^2\theta_{23}(\text{true}) = 0.4$. The width of each of the bands is mapped by increasing the value of $\sin^2 2\theta_{13}$(true) from 0.08, through 0.1, and up to 0.12. As seen in the previous subsection, the $\Delta\chi^2$ for the wrong mass hierarchy increases with $\sin^2 2\theta_{13}$(true) for a given value of $\sin^2\theta_{23}$(true) and ICAL@INO exposure. A comparison of the $\Delta\chi^2$ for different values of $\sin^2\theta_{23}$(true) reveals that the $\Delta\chi^2$ also increases with $\sin^2\theta_{23}$(true).

From Fig. 5.7 one infers that for $\delta_{CP}(\text{true}) = 0$, a combined analysis of all relevant experimental data including 5 years of ICAL@INO exposure would give the neutrino mass hierarchy from anywhere between about 2σ to 3.8σ, depending on the values of $\sin^2\theta_{23}$(true) and $\sin^2 2\theta_{13}$(true). With 10 years of running of ICAL@INO this would improve to 2.3σ to 4.6σ, depending on what value of $\sin^2 2\theta_{13}$(true) and $\sin^2\theta_{23}$(true) have been chosen by mother Nature. Here we have allowed $\sin^2\theta_{23}$(true) to vary between $[0.4 - 0.6]$ and $\sin^2 2\theta_{13}$(true) between $[0.08 - 0.12]$. We next look at the impact of δ_{CP}(true) on the prospects of determining the neutrino mass hierarchy.

5.7 Impact of δ_{CP} and δ_{CP}(true)

So far we had taken δ_{CP}(true)=0 in the data and varied δ_{CP} in the fit only for the long baseline experiments. For the analysis of the ICAL@INO data, we had kept δ_{CP} fixed to zero in both the data and the theory. The reason was that while the χ^2 for T2K and NOνA are strongly dependent on δ_{CP}, the mass hierarchy χ^2 for ICAL@INO shows a very mild dependence on it. We show this dependence explicitly in Fig. 5.8 for 10 years exposure in ICAL@INO and compare it with the corresponding dependence of NOνA (see also [72])[2].

---

[2] This figure was shown in [72]. However, the analysis in [72] was in terms of neutrinos done with some assumed values of the detector resolutions and efficiencies. Since we do here the complete analysis of the ICAL@INO projected data in terms of the detected muons and with realistic detector resolutions and efficiencies obtained from ICAL simulations, we reproduce a similar plot for completeness.

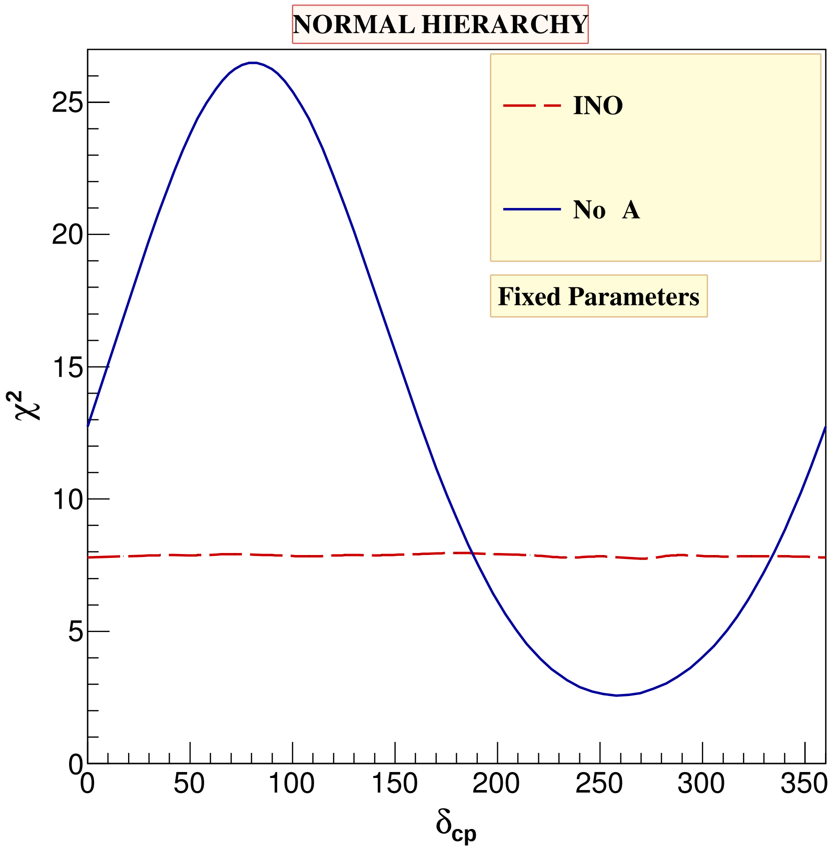

Figure 5.8: The change of $\Delta\chi^2$ for the wrong hierarchy as a function of the δ_{CP} chosen in the fit. The data was generated for normal hierarchy and δ_{CP}(true)=0. The other oscillation parameters in both data and theory are fixed at their benchmark values given in Table 6.1. The solid blue line shows the change in $\Delta\chi^2$ with δ_{CP} for NOνA, while the dashed red line shows the corresponding variation of $\Delta\chi^2$ for ICAL@INO. The ICAL@INO exposure was taken as 10 years.

We generate the data for normal hierarchy and at the benchmark values of the oscillation parameters from Table 6.1 and with $\sin^2\theta_{23}(\text{true}) = 0.5$ and $\sin^2 2\theta_{13}(\text{true}) = 0.1$. In the fit with inverted hierarchy, we keep all oscillation parameters fixed, except δ_{CP} which is varied over its full range $[0-2\pi]$. The corresponding $\Delta\chi^2$ is plotted in Fig. 5.8 as a function of the δ_{CP} in the fit. The red long-dashed line shows the δ_{CP} dependence of $\Delta\chi^2$ for ICAL@INO, while the blue solid line shows the wild fluctuation of $\Delta\chi^2$ expected for NOνA. Amongst the accelerator and reactor experiments we show only NOνA in this figure as the leading contribution to the mass hierarchy comes from this experiment. We reiterate that at each point we use the data generated at δ_{CP}(true)=0. The figure shows that when we fit the data with inverted hierarchy, the $\Delta\chi^2$ for NOνA changes from more that 26 for $\delta_{CP} \simeq 80^\circ$ to less than 3 for $\delta_{CP} \simeq 260^\circ$. When marginalized over δ_{CP} in the fit, obviously it will return the lowest value of the $\Delta\chi^2$, which in this case would be 2.59 [3]. When marginalized over all oscillation parameters, the sensitivity further reduces to $\Delta\chi^2 = 1.77$. The contribution from ICAL@INO on the other hand is seen to be almost independent of δ_{CP}. Note that such a figure was also shown in [77] for the ICAL@INO simulations. However, the analysis of the ICAL data has been improved since then and more types of systematic uncertainties introduced. This explains the change in the behavior of this plot with the dependence of the $\Delta\chi^2$ becoming flatter with δ_{CP}. From this study we conclude that one does not need to marginalize over δ_{CP} for the ICAL@INO data. However, for the long baseline experiments a fine marginalization over this parameter is absolutely crucial, especially for mass hierarchy studies.

We had seen in Fig. 5.8 (and as is well known) that the long baseline experiments are very sensitive to δ_{CP}. In that figure we were studying the impact of changing δ_{CP} in the fit for a particular δ_{CP}(true) in the data. In particular, we had taken δ_{CP}(true)=0. A pertinent question at this point is the following: what is the impact of δ_{CP}(true) on the sensitivity

---

[3] Note that here the other parameters are fixed and only NOνA data is being considered in the analysis, while the $\Delta\chi^2$s shown in Table 5.2 are for a global fit of all data with all oscillation parameters allowed to vary freely in the fit and the combined χ^2 marginalized over them.

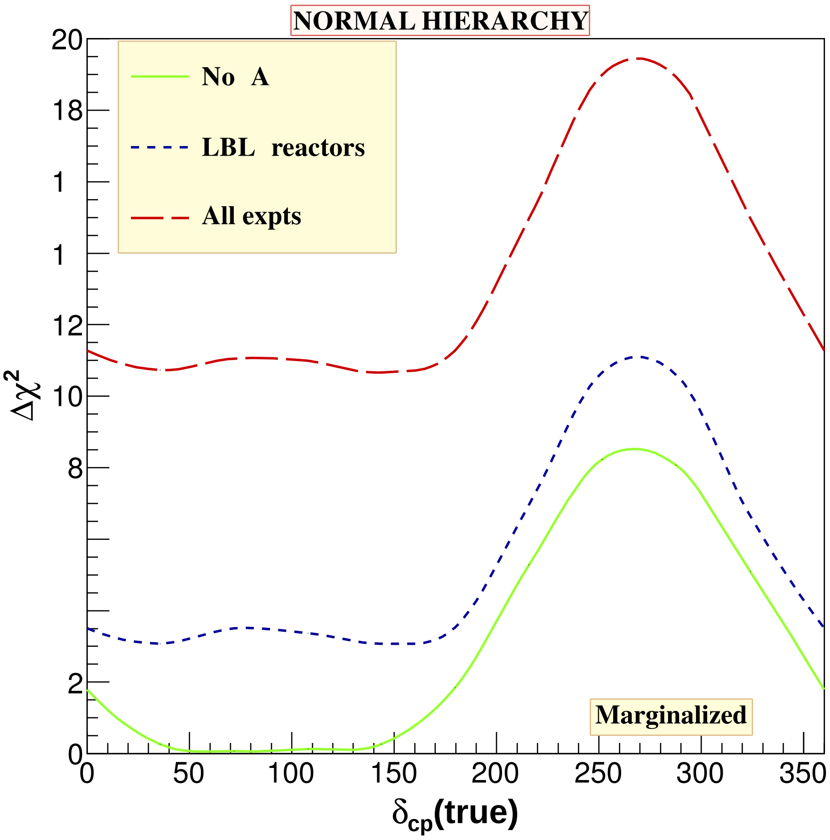

Figure 5.9: Impact of δ_{CP}(true) on the mass hierarchy sensitivity. The sensitivity change of NOνA due to δ_{CP}(true) is shown by the green solid line. The $\Delta\chi^2$ for the wrong mass hierarchy expected from the combined data from T2K, NOνA and the reactor experiments is shown by the short-dashed blue line. The global $\Delta\chi^2$ for the wrong mass hierarchy from the combined ICAL@INO plus the accelerator and reactor data is shown by the red long-dashed line. Data was generated for normal hierarchy and at the benchmark oscillation point from Table 6.1 with $\sin^2\theta_{23}(\text{true}) = 0.5$ and $\sin^2 2\theta_{13}(\text{true}) = 0.1$ and at each value of δ_{CP}(true) shown in the x-axis. The fit to the wrong inverted hierarchy was fully marginalized over all oscillation parameters. The ICAL@INO exposure was taken as 10 years.

of the experiments to the neutrino mass hierarchy? We present the answer to this question in Fig. 5.9, where we show the $\Delta\chi^2$ for the mass hierarchy sensitivity as a function of δ_{CP}(true). To obtain these curves, we generate data for normal hierarchy at each value of δ_{CP}(true) shown in the x-axis and then fit this data for inverted hierarchy by marginalizing over *all* oscillation parameters, including δ_{CP}. The data were generated for the benchmark oscillation point given in Table 6.1, $\sin^2\theta_{23}(\text{true}) = 0.5$ and $\sin^2 2\theta_{13}(\text{true}) = 0.1$. The exposure considered is 10 years of ICAL@INO and full run for all other experiments. The green solid line in this figure is for only NOνA, the blue short-dashed line is obtained when we combine NOνA, T2K and all the reactor data, while the red long-dashed line is what we get when the ICAL@INO data is also added to the long baseline and reactor data. As expected, the ICAL@INO data is almost completely independent of δ_{CP}(true) and so is its projected sensitivity to the neutrino mass hierarchy. On the other hand, the reach of the NOνA experiment for determining the neutrino mass hierarchy is seen to be extremely sensitive to the value of δ_{CP}(true). All our plots shown so far on the global mass hierarchy reach were done assuming $\delta_{CP}(\text{true}) = 0$. We can see from the figure that indeed the statistical significance with which we could rule out the inverted mass hierarchy in this case is 3.4σ, as discussed before. The $\Delta\chi^2$ for $\delta_{CP}(\text{true}) = 0$ for NOνA is 1.77. However, this quickly falls to almost zero for $\delta_{CP}(\text{true}) \simeq [50^\circ - 150^\circ]$. Thereafter, it rises sharply giving a $\Delta\chi^2 = 8.21$ around $\delta_{CP}(\text{true}) \simeq 270^\circ$, and then finally falls back to $\Delta\chi^2 = 1.77$ for $\delta_{CP}(\text{true}) = 360^\circ$. When T2K and all reactor data are added, there is an improvement to the combined sensitivity due to constraint coming from the mismatch between the best-fit for different experiments. This is specially relevant in the $\delta_{CP}(\text{true}) \simeq [50^\circ - 150^\circ]$ range where NOνA by itself gives no mass hierarchy sensitivity. However, once we add the T2K and reactor data to NOνA data, the $\Delta\chi^2$ of this combined fit in this region of δ_{CP}(true) increases to $\simeq 3.5$. The reason for this can be understood as follows. For the case where $\delta_{CP}(\text{true}) = 72^\circ$, the best-fit for NO$\nu$A alone was $\delta_{CP} = 234^\circ$, $\sin^2\theta_{23} = 0.5$ and $\sin^2 2\theta_{13} = 0.1$. For this δ_{CP}(true), T2K data taken alone gave $\Delta\chi^2 \simeq 0$ with best-fit at

$\delta_{CP} = 198^\circ$, $\sin^2\theta_{23} = 0.52$ and $\sin^2 2\theta_{13} = 0.08$. A combined fit with all accelerator and reactor data gave best-fit at $\delta_{CP} = 198^\circ$, $\sin^2\theta_{23} = 0.48$ and $\sin^2 2\theta_{13} = 0.1$. This results in a contribution to the mass hierarchy $\Delta\chi^2 = 0.92$ from NOνA, $\Delta\chi^2 = 1.41$ from T2K and $\Delta\chi^2 = 1.1$ from reactors. That the reactor data return a $\Delta\chi^2$ contribution to the mass hierarchy sensitivity might appear strange at the outset since the combined fit given above has a best-fit $\sin^2 2\theta_{13} = 0.1$, and one usually does not expect the reactor data to depend on sign of Δm^2_{31}, δ_{CP} and $\sin^2\theta_{23}$. However, note that the reactor data depend on $|\Delta m^2_{31}|$ and what we use in our fits is $\Delta m^2_{\rm eff}$ given by Eq. (5.1) which is related to δ_{CP}. Therefore, as discussed earlier in section 6, this subtlety regarding the choice of the definition of the neutrino mass hierarchy results in a small change in the best-fit $|\Delta m^2_{31}|$, which in turn results in a small $\Delta\chi^2$ contribution to the mass hierarchy from the reactor experiments. Finally, addition of the ICAL@INO data raises the $\Delta\chi^2$ by a constant amount for all values of δ_{CP}(true). Therefore, depending on δ_{CP}(true) the combined sensitivity to the neutrino mass hierarchy could range from 3.3σ (for $\delta_{CP}(\text{true}) = 144^\circ$) to 4.4σ (for $\delta_{CP}(\text{true}) \simeq 270^\circ$). These numbers are for $\sin^2\theta_{23}(\text{true}) = 0.5$ and $\sin^2 2\theta_{13}(\text{true}) = 0.1$ and will improve for larger values of these parameters.

In the next chapter , we discuss how to improve the potential of ICAL@INO in mass hierarchy measurement.

CHAPTER 6

MEASURING THE MASS HIERARCHY WITH MUON AND HADRON EVENTS IN ICAL@INO

In the previous chapter, we considered the sensitivity of the ICAL@INO experiment to the measurement of the neutrino mass hierarchy. We showed that when combined with expected data from all the current accelerator and reactor experiments, Daya Bay, RENO, Double Chooz, T2K and NOνA, 50×10 kton-year of data from ICAL@INO was shown to give a mass hierarchy sensitivity of $2.3\sigma - 5.7\sigma$, depending on the true value of $\sin^2 2\theta_{13}$, $\sin^2\theta_{23}$ and δ_{CP}. However, note that these analyzes were based on using only the muon sample of the simulated INO data. The full detector response to muons obtained from detailed Geant-based simulations of the ICAL detector were used in these studies and the sensitivity of the experiment to the neutrino oscillation parameters estimated. In particular, the muon energy resolution was seen to be around $\sigma_{E_\mu}/E_\mu = 10 - 15\%$, below what has been found from simulations of other similar detectors such as MINOS and MONOLITH [78]. However, the simulations of the ICAL detector is on-going and the results obtained on the detector response to muons is expected to evolve along with the improvement in the detector simulation code as well as the analysis. Amongst other things, the reconstruction algorithm is being improved upon, which would allow for better reconstruction of the muon track which could lead to better energy resolution of the muons. In addition, ICAL will also be somewhat sensitive to the associated hadron(s) which produce(s) a shower. The detector response to the hadron shower and in particular the hadron energy resolution was recently studied by the INO collaboration.

In this analysis we study how much the mass hierarchy sensitivity of the ICAL@INO, or any other similar experiment, could improve, by improving the energy and angle resolution of the detector, as well as its particle reconstruction efficiency. We start with the muon event analysis and study how much the mass hierarchy sensitivity would improve with the energy resolution of the muons. Since the angular resolution of the muons obtained from the recent simulation results by the INO collaboration is found to be extremely good, we fix the angular resolution to be $\sigma_{\Theta_\mu} = 0.01$ in $\cos\Theta_\mu$, a value that is consistent with the simulation results, and vary only the energy resolution. We also study the impact of increasing the reconstruction efficiency of the muons, though this is more mundane as the reconstruction efficiency merely increases the overall statistics of the muons.

We next include the hadron events in the study and present results of a statistical analysis where muon and hadron events are included separately in a combined χ^2 function. We propose a unique way of tagging the hadron events. We tag every hadron event with the zenith angle of the corresponding muon produced in the charged current interaction of the neutrino. We collect all such hadrons in every muon zenith angle bin. This hadron sample can then be further binned in hadron energy as well as hadron zenith angle. We include these hadron events in the statistical analysis along with the muons and show that the mass hierarchy sensitivity of the experiment improves reasonably with the inclusion of these events.

As mentioned previously, Most analyzes of the atmospheric neutrino experiments are in terms of the reconstructed neutrino energy and zenith angle. The neutrino energy and zenith angle can be reconstructed from the measured energy and zenith angle of the muon and hadron events. The dependence of the mass hierarchy sensitivity to the reconstructed neutrino energy and angle resolution functions has been studied in somewhat details in the literature [61, 65]. Reconstructing the neutrino energy in magnetized iron detectors can be done without too much difficulty by adding the measured muon energy with the measured hadron energy. While the final simulation results from the INO collaboration are still awaited, the MINOS simulations have yielded an energy resolution $\sigma_{E_\nu}/E_\nu \simeq 15\%$ while the MONOLITH proposal quotes $\sigma_{E_\nu}/E_\nu \simeq 20\%$ [78]. On the other hand, the neutrino zenith angle will have to be extracted either by reconstructing the neutrino momentum from combining the muon and hadron momenta, or from simulating the angle between the neutrino and muon direction. In this analysis, we will present results on the neutrino analysis for two cases. In first one we will bin the data in neutrino energy and neutrino zenith angle bins. We will use the zenith angle resolution function for the neutrinos quoted in the MONOLITH proposal [78], and show the mass hierarchy sensitivity results as a function of the neutrino energy resolution. For the next case we will bin the data in neutrino energy and muon zenith angle bins. For this case we will use a fixed muon zenith angle resolution function which agrees with the results of the INO muon simulations. We will compare the sensitivity results obtained from the two cases.

A discussion on marginalization of the χ^2 over all the oscillation parameters in the fit is in order. It is well known that marginalization over the oscillation parameters does reduce the mass hierarchy sensitivity when the atmospheric data is taken alone. However, we had shown in chapter 5 that when we do a combined fit of the atmospheric neutrino data along with the data from the other accelerator and reactor experiments, Daya Bay, RENO, Double Chooz, T2K and NOνA, then the $\Delta\chi^2$ remains the same as that obtained by keeping all parameters fixed at their assumed true values. Since data from these accelerator and reactor experiments will anyway be available by the time we get the atmospheric neutrino data from any magnetized iron detector, it is pertinent to always add them in the fit. This is what was done in chapter 5. In this analysis, since we wish to only study how to optimize the analysis of the atmospheric neutrino data for maximum mass hierarchy sensitivity, we do not explicitly include the accelerator and reactor data. However, since their major role in the global analysis is to keep best-fit $|\Delta m^2_{31}|$, $\sin^2\theta_{23}$ and $\sin^2 2\theta_{13}$ very close to their assumed true values, we incorporate this feature by keeping these parameters fixed in the fit. The main purpose for this simplification is to save computation time as the main physics impact is incorporated anyway. The accelerator experiment NOνA also gives a contribution to the neutrino mass hierarchy. But it was shown in chapter 5, [72] that this does not lead to any synergy between the atmospheric neutrino data and NOνA data. Therefore, the additional contribution from NOνA (as a function of the true value of δ_{CP}) can simply be added to the $\Delta\chi^2$ obtained from the atmospheric neutrino data.

This chapter is organized as follows. We start with a description of the earth matter effects in section 6.1. In section 3 we discuss the events in terms of the neutrino energy spectrum, muon energy spectrum and hadron energy spectrum. We begin our main results part in section 4 where we give the mass hierarchy sensitivity when only the muon data is included and show the effect of the muon energy resolution and reconstruction efficiency on the reach of the experiment in ruling out the wrong hierarchy. In section 5 we should how the mass hierarchy sensitivity improves when we include the independent hadron events in addition to the muon events in the analysis. Section 6 gives the comparative results when we do the analysis in terms of the neutrino energy and neutrino angle as well as in terms of neutrino energy and muon zenith angle.

6.1 Earth Matter Effects in Oscillation Probabilities

Atmospheric neutrinos (and antineutrinos) are produced in both ν_μ and ν_e (and $\bar{\nu}_\mu$ and $\bar{\nu}_e$) flavors, with a flavor ratio of roughly $\phi_{\nu_\mu}/\phi_{\nu_e} \sim 2$ at sub-GeV energies. This ratio increases with the neutrino energy. The neutrinos, on their way from their point of production in the atmosphere to the detector, undergo flavor oscillations. On arrival at the detector, they produce the corresponding charged lepton through charged current interaction on nucleons. Since the oscillated atmospheric neutrino "beam" is a combination of all three flavors, they produce electrons, muons, as well as tau leptons in the detector. Magnetized iron calorimeters such ICAL@INO can only efficiently detect the muons, and are hence sensitive to only muon type neutrinos. However, being magnetized, this kind of detector will be able to identify the charge of the muon and hence will be able to separate the ν_μ signal from the $\bar{\nu}_\mu$ signal very efficiently.

Since the oscillated muon type neutrinos arriving at the detector are a combination of the survived ν_μ produced in the atmosphere and the flavor oscillated ν_μ coming from ν_e produced in the atmosphere, the oscillation probability channels relevant for atmospheric muon neutrinos are the survival probability $P_{\mu\mu}$ and transition probability $P_{e\mu}$. If for the sake of simplicity of discussion we take $\Delta m^2_{21} = 0$, then for the oscillation probabilities can be written as

$$
\begin{aligned}
P_{\mu\mu}^{approx} = 1 \; & -\sin^2\theta_{13}^M \sin^2 2\theta_{23} \sin^2 \frac{[(\Delta m_{31}^2 + A) - (\Delta m_{31}^2)^M]L}{8E_\nu} \\
& -\cos^2\theta_{13}^M \sin^2 2\theta_{23} \sin^2 \frac{[(\Delta m_{31}^2 + A) + (\Delta m_{31}^2)^M]L}{8E_\nu} \\
& -\sin^2 2\theta_{13}^M \sin^4\theta_{23} \sin^2 \frac{(\Delta m_{31}^2)^M L}{4E_\nu}, \qquad (6.1)
\end{aligned}
$$

and

$$
P_{e\mu}^{approx} = \sin^2 2\theta_{13}^M \sin^2\theta_{23} \sin^2 \frac{(\Delta m_{31}^2)^M L}{4E_\nu}, \qquad (6.2)
$$

where $A = 2\sqrt{2}G_F N_e E_\nu$ is the matter potential in earth, N_e being the electron density inside earth and E_ν the neutrino energy. The quantities $(\Delta m_{31}^2)^M$ and θ_{13}^M are the mass squared difference and mixing angle in constant density matter and are given as

$$
(\Delta m_{31}^2)^M = \left((\Delta m_{31}^2 \cos 2\theta_{13} - A)^2 + \Delta m_{31}^2 \sin^2 2\theta_{13} \right)^{1/2}, \qquad (6.3)
$$

$$
\sin^2 2\theta_{13}^M = \frac{\Delta m_{31}^2 \sin^2 2\theta_{13}}{\left((\Delta m_{31}^2 \cos 2\theta_{13} - A)^2 + \Delta m_{31}^2 \sin^2 2\theta_{13} \right)}. \qquad (6.4)
$$

We can see the role of θ_{13}-driven earth matter effects and the neutrino mass hierarchy through these expressions. For $\theta_{13} = 0$, we get $(\Delta m_{31}^2)^M = (\Delta m_{31}^2 - A)$ and $\theta_{13}^M = 0$ from Eqs. (6.3) and (6.4). Plugging these values in Eqs. (6.1) and (6.2) we find that we would have no earth matter effects in neutrino oscillations for $\theta_{13} = 0$. In particular, we can see that $P_{e\mu}^{approx} = 0$ and $P_{\mu\mu}^{approx}$ is the same for both normal ($\Delta m_{31}^2 > 0$) as well as inverted hierarchy ($\Delta m_{31}^2 < 0$). However, for non-zero θ_{13} we get a difference in $P_{e\mu}^{approx}$ as well as $P_{\mu\mu}^{approx}$ between $\Delta m_{31}^2 > 0$ and $\Delta m_{31}^2 < 0$ due the earth matter effects. This difference can be used to distinguish between the normal and inverted neutrino mass hierarchy.

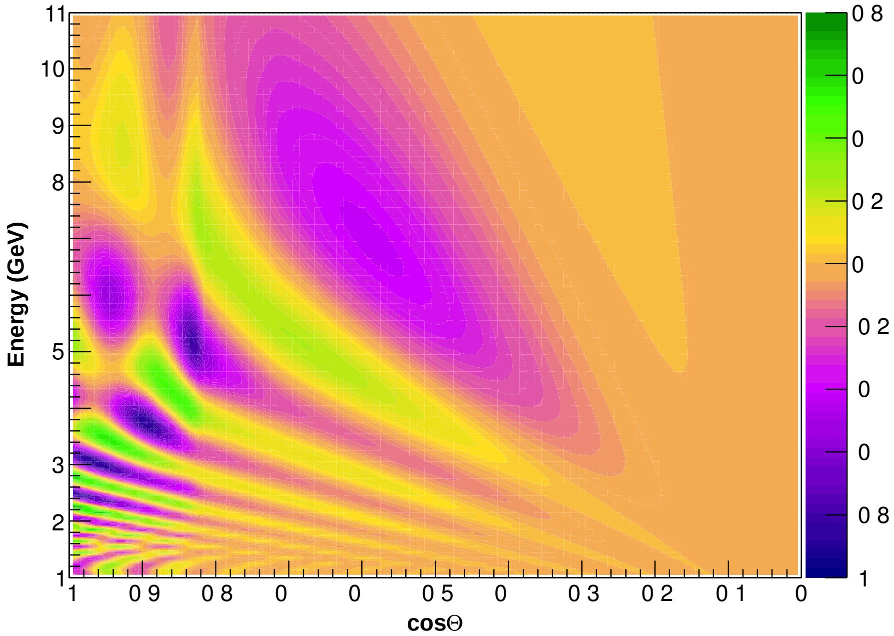

Figure 6.1: Oscillogram showing the difference in the muon neutrino survival probability for normal and inverted hierarchy, $\Delta P_{\mu\mu}$, in the neutrino energy and zenith angle plane.

In the discussion above we had put $\Delta m^2_{21} = 0$ and used a constant density for the matter for simplicity of the discussion. In all numerical results presented in this analysis we use the full three-generation oscillation probability calculated using the 24 layer PREM profile for the earth matter density [27]. Following the chapter 5, we will continue to use the definition normal hierarchy as $\Delta m^2_{\rm eff} > 0$ and inverted hierarchy as $\Delta m^2_{\rm eff} < 0$ where $meff$ is defined by Eq. 5.1 We will show through our numerical results in section 4, that fixing the $|\Delta m^2_{\rm eff}|$ (and similarly other oscillation parameters) in the fit for inverted hierarchy ($\Delta m^2_{\rm eff} < 0$) does not make any difference to our final results when the T2K, NOνA, Daya Bay, RENO and Double Chooz results are included.

The oscillogram in Fig. 6.1 shows the difference between the survival probability predicted for the normal ($P^{NH}_{\mu\mu}$ defined as $\Delta m^2_{\rm eff} > 0$) and inverted ($P^{IH}_{\mu\mu}$ defined as $\Delta m^2_{\rm eff} < 0$)

Parameter	True value used in data
Δm^2_{21}	7.5×10^{-5} eV^2
$\sin^2\theta_{12}$	0.3
$\lvert\Delta m^2_{\rm eff}\rvert$	2.4×10^{-3} eV^2
δ_{CP}	0
$\sin^2\theta_{23}$	0.5
$\sin^2 2\theta_{13}$	0.1

Table 6.1: Benchmark true values of oscillation parameters used in the simulations.

hierarchy. This figure has been generated by calculating the full three generation survival probability $P_{\mu\mu}$ at the benchmark oscillation parameter values given in Table 6.1 and for the 24 layer PREM profile of the earth [27]. We show the difference

$$\Delta P_{\mu\mu} = P^{NH}_{\mu\mu} - P^{IH}_{\mu\mu}, \tag{6.5}$$

as oscillograms in the neutrino zenith angle and neutrino energy plane. We notice that $\Delta P_{\mu\mu}$ fluctuates and changes sign as we change both the neutrino energy as well as the neutrino zenith angle. The sign of $\Delta P_{\mu\mu}$ is crucial, as it tells us whether earth matter effects increase or decrease the survival probability. Since $\Delta P_{\mu\mu}$ oscillates from positive to negative with energy and zenith angle, averaging it over either or both of these quantities will severely deplete and wash out the net earth matter effects in the ν_μ signal at the detector. Therefore, observation of earth matter effects in ν_μ is best performed with detectors having good energy as well as zenith angle resolution.

The fluctuations in $\Delta P_{\mu\mu}$ are seen to be faster for lower energies and longer baselines. In particular, for the zenith angles when the neutrinos cross the core of the earth ($\cos\Theta < -0.84$), $\Delta P_{\mu\mu}$ is seen to be much more complicated. One can notice that for $E_\nu \sim 2-4$ GeV, earth matter effects are significantly stronger for these cases. This sharp increase in $|\Delta P_{\mu\mu}|$ is due to the so-called parametric enhancement of earth matter effects [79], also known as oscillation length resonance effects [80]. While the matter effects are large here, the Fig. 6.1 reveals that that the sign of $\Delta P_{\mu\mu}$ fluctuates very fast between being positive and negative, in this regime. This rapid fluctuation, as we will see later, will make the observation of earth matter effects extremely difficult at these energies and zenith angles. One would need extremely good reconstruction of the neutrino energy and angle for the observation of these parametric resonance effects.

Even for mantle crossing trajectories and/or higher neutrino energies, $\Delta P_{\mu\mu}$ fluctuates sign between positive and negative. However, the fluctuations are slower. Indeed from Fig. 6.1 we note that for a large range of only mantle crossing baselines, $\Delta P_{\mu\mu}$ stays predominantly negative for neutrino energies $E_\nu \gtrsim 4-5$ GeV. In particular, we can see that $\Delta P_{\mu\mu} \simeq -0.4$ for a wide range of E_ν and $\cos\Theta_\nu$. In these cases the earth matter effects come mainly from the standard MSW [26] enhancement of the oscillation probability.

The corresponding oscillation probabilities for the muon antineutrinos is same with the matter term A replaced with $-A$ everywhere. Therefore, for the antineutrinos the effect of earth matter will be exactly opposite to what we see for the neutrinos. In particular, the antineutrino signal would see earth matter effects for the inverted hierarchy. If the antineutrino flux and cross-sections were same as the ones for the neutrinos, then adding up the data from neutrinos with those from the antineutrinos would completely wash out the earth matter effects between the normal and inverted hierarchy. However, in reality the antineutrino fluxes and cross-sections are smaller than those for the neutrinos, and hence a resultant mass hierarchy effect would survive even on adding the neutrino and antineutrino data. However, the magnetized iron calorimeters such as ICAL@INO, have excellent charge identification capabilities and hence can distinguish the neutrinos from the antineutrinos. Therefore, these detectors can observe earth matter effects separately in both the neutrino as well as the antineutrino channels. Therefore, instead of partially washing the net earth matter effects, the antineutrino channel in these detectors add to the mass hierarchy sensitivity.

6.2 Earth Matter Effects in Event Rates

We discussed the energy and zenith angle dependence of the earth matter effects in the muon neutrino survival probability $P_{\mu\mu}$ in the previous section. However, what arrives at the detector has impact from a combination of the survival probability $P_{\mu\mu}$ and the conversion probability $P_{e\mu}$. Though the survival probability $P_{\mu\mu}$ dominates, the conversion probability $P_{e\mu}$ has the effect of washing out partially the effect of earth matter and hence the mass hierarchy. In addition, the neutrinos interact with the detector nucleons through a charged current interaction to produce the corresponding muon and final state hadron(s). What is measured in the detector is the energy and zenith angle of the final state particles, *viz.*, the muon and, if possible, the hadron(s). A neutrino of energy E_ν could produce muons with any energy $E_\mu \leq E_\nu$. The same argument hold for the the zenith angle dependence as well. We had seen in the previous section that the net hierarchy effect in $P_{\mu\mu}$ oscillates between being positive and negative, both with energy as well as zenith angle. Therefore, in going from the neutrino energy to the muon energy through the interaction cross-section, what we effectively get is a smearing of the hierarchy dependent earth matter effects. This results in loss in the sensitivity of the experiment to the neutrino mass hierarchy. The finite detector resolutions for the energy and angle measurements further deteriorates the sensitivity. The only way to regain the sensitivity will be to simultaneously measure the energy and zenith angle of both the muon and the corresponding hadron, in order to reconstruct the neutrino energy and zenith angle. However, since the muon, and particularly the hadron, energy and angle cannot be measured very accurately in the iron calorimeter detector, the reconstruction ability of the experiment suffers. In this section we will show how the neutrino mass hierarchy sensitivity in the event spectrum changes with:

- going from measuring the events in terms of neutrino energy and zenith angle to muon and hadron energy and zenith angle,
- inclusion of the appearance channel $P_{e\mu}$,
- inclusion of the finite detector resolutions.

We show the dependence of mass hierarchy sensitivity on these issues first in the muon event spectrum, then in the hadron event spectrum and finally in the neutrino event spectrum.

6.2.1 Earth Matter effects in Muon Events

This analysis is based on the numerical simulation discussed in chapter 4. in this analysis we will use flat projected values for the detector response such as angle resolution, energy resolution, charge identification efficiency and reconstruction efficiency. This is justified as the results presented here are for the sake of illustration only to show the dependence of the neutrino mass hierarchy to the different ways of treating the data and their corresponding detector response functions. Since the first set of simulation results performed by the INO collaboration have shown extremely good muon zenith angle resolution, we will fix $\sigma_{\Theta_\mu} = 0.01$ for all muon energies and zenith angles, throughout this analysis. The charge identification efficiency is also fixed at flat 99% everywhere. The muon energy resolution and the reconstruction efficiencies are allowed to vary. We will mention this as and when applicable. All detector response functions are taken to be the same for the μ^- and μ^+ events.

As discussed before, for normal (inverted) hierarchy we expect earth matter effects in the μ^- (μ^+) events, while for inverted (normal) hierarchy there will be no earth matter

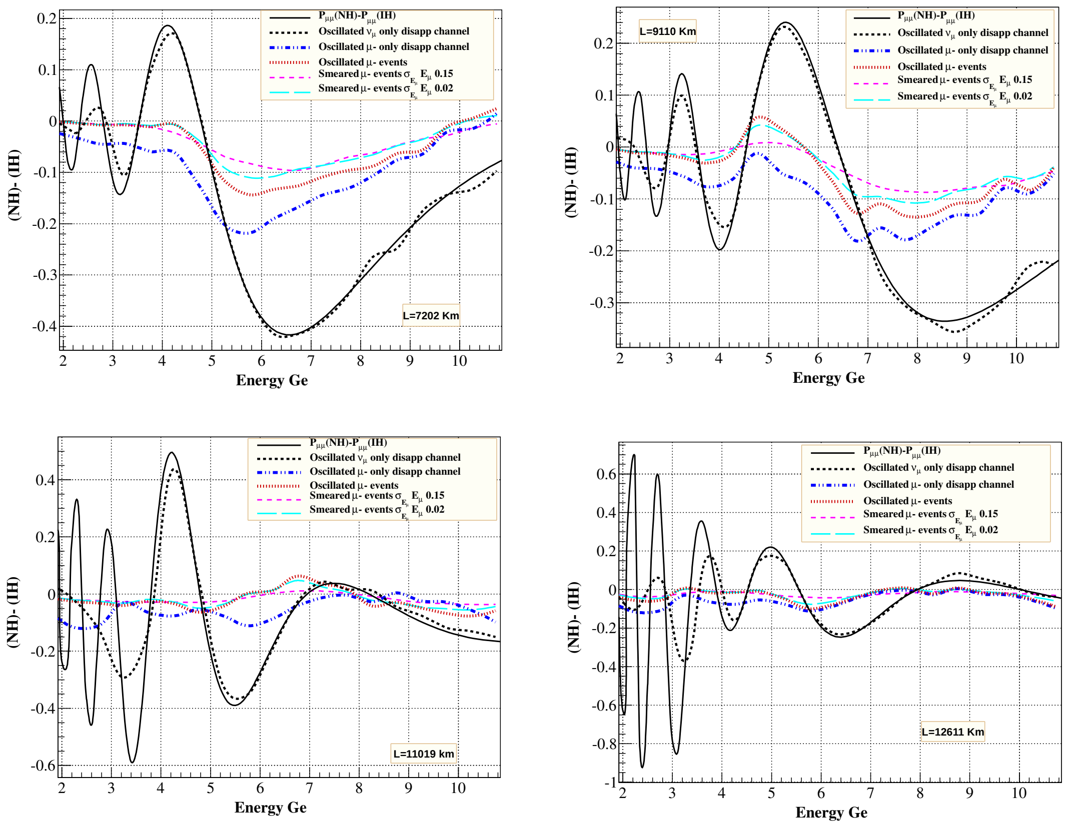

Figure 6.2: The difference in the predicted muon event rates for normal and inverted hierarchy, normalized to the no-oscillation muon event rate, shown as a function of energy. The four panels show the event spectrum generated in four zenith angle bins, marked by the path-length traversed at the mid-point of the bin. The solid black lines show the $\Delta P_{\mu\mu}$ at the probability level only. The black dashed lines give the difference between the predicted rate for normal and inverted hierarchy when only the $P_{\mu\mu}$ (disappearance) channel is taken and data binned in neutrino energy. The blue dot-dashed lines show the corresponding difference when only the $P_{\mu\mu}$ channel is taken and data binned in muon energy. The red dotted lines are obtained when we add the $P_{e\mu}$ (appearance) channel and bin the data in muon energy. The pink dashed and cyan long dashed lines are obtained when we apply on the red dotted lines the muon energy resolution functions with widths $\sigma_{E_\mu}/E_\mu = 0.15\%$ and 2%, respectively.

effects in the μ^- (μ^+) channel. To quantify the mass hierarchy sensitivity of the experiment, we simulate the μ^- and μ^+ data separately for the normal mass hierarchy and fit this data with the inverted mass hierarchy. Therefore for this example case, there will be earth matter effects in the μ^- events in the data, while no earth matter effects in the theoretical fit. On the other hand, for the μ^+ channel, there will be no earth matter effects in the data sample, but the theoretical prediction for the event spectrum will have earth matter effects. Because the magnetized iron calorimeter such as ICAL@INO will have excellent charge identification capabilities, it can distinguish the μ^- signal from the μ^+ one. What is relevant for mass hierarchy studies will then be the difference between the predicted events for normal and inverted mass hierarchies, separately in the μ^- and μ^+ channels.

We present this difference for μ^- events in Fig. 6.2. A similar figure can be drawn for the μ^+ events, but we will not repeat it here. The four panels of this figure are for four different zenith angles, and hence, four different path lengths of the neutrino in earth, $L = 7202$ km, 9110 km, 11019 km and 12611 km. The different lines in this figure are as follows. The black solid lines give $\Delta P_{\mu\mu} = P_{\mu\mu}^{NH} - P_{\mu\mu}^{IH}$, (cf. Eq. 6.5) as a function of the *neutrino energy* E_ν, and have been given here to show the impact of the interaction cross-section on the mass hierarchy sensitivity in going from the neutrino energy to the muon energy. All other lines in this figure show the difference between the predicted events for normal and inverted hierarchies, normalized to the unoscillated events. Each muon event output from Nuance is characterized in terms of the incoming true neutrino angle and energy and outgoing true muon angle and energy. Therefore, we can bin the data in either the neutrino energy or the muon energy. The black dashed lines show this difference when the data is binned in true neutrino energy and angle bins and only the muon neutrino survival probability $P_{\mu\mu}$ is taken into account. The x-axis for these lines are therefore the true neutrino energy E_ν. We can see that the the black dashed lines follow the black solid lines to reasonable accuracy. This is expected since we have used only $P_{\mu\mu}$ for the event difference shown by the black dashed lines, and since it is binned in terms of the neutrino energy and angle, it has a one-to-one correspondence with the difference $\Delta P_{\mu\mu}$ shown by the back solid lines. The small difference between the two sets of curves comes mainly due to the Monte Carlo fluctuations in the NUANCE output.

Next we use the same data set where only the survival probability $P_{\mu\mu}$ is considered and bin the data in terms of the *true muon energy* E_μ. This is shown by the blue dot-dashed curves in Fig. 6.2. The x-axis for these lines are therefore the true muon energy E_μ. Notice now that the event spectrum now gets degraded in energy. For example for $L = 7202$ km case, while the maximum difference due to earth matter effects were coming at $E_\nu \sim 6-7$ GeV in terms of the true neutrino energy, it appears at $E \sim 5-6$ GeV in terms of the true muon energy. Notice also that the net earth matter effect is also substantially reduced in going from neutrino energy to muon energy. This mainly comes due to the kinematic averaging effect of the neutrino-nucleon cross-sections wherein a neutrino with a given neutrino energy E_ν could produce a muon with any energy between E_ν and zero. This results in the smearing out of the oscillation effects of $\Delta P_{\mu\mu}$ and since the $\Delta P_{\mu\mu}$ fluctuates between being positive and negative, the averaging brings about a net cancellation of the earth matter effects. However, despite this kinematic smearing of the signal, some residual earth matter effects remain with $\Delta X = X(NH) - X(IH) < 0$ predominantly. In particular, for the mantle-crossing bins shown in upper panels for $L = 7202$ km and 9110 km in Fig. 6.2, the $\Delta X < 0$ for all muon energies and we get $\Delta X \simeq -0.2$ at $E_\mu \simeq 5-6$ GeV and $6-8$ GeV, respectively. Since the oscillations in the net earth matter effects are larger for the core-crossing bins shown in the lower panels for $L = 11019$ km and 12611 km in Fig. 6.2, the smearing is more pronounced for these zenith angles. As a result, even though the actual earth matter effects in the neutrinos are much larger for these zenith angles, in the muon sample the averaged ΔX for these bins are significantly lower. Still there is some residual earth matter effects with $\Delta X \simeq -0.1$ predominantly, for most muon energies.

The blue dot-dashed lines that we discussed above have contribution from only the survival probability channel $P_{\mu\mu}$. However, since both ν_μ and ν_e are produced in the earth's atmosphere, some of the ν_μ arriving at the detector will be the ones produced as ν_e and which have oscillated into ν_μ through the $P_{e\mu}$ conversion probability. These "appearance events" have to be added to the ones we had obtained using the survival probability $P_{\mu\mu}$, to obtain the final muon event spectrum which will be observed in magnetized iron detectors such as ICAL@INO. These are shown by the red dotted lines in Fig. 6.2. A comparison of the red dotted lines with the blue dot-dashed lines reveals the impact of the $P_{e\mu}$ channel on the net earth matter effects and hence the mass hierarchy sensitivity of atmospheric neutrino experiments. The effect of $P_{e\mu}$ is to reduce $|\Delta X|$ for all energies and all zenith angles. The reason for this can be seen from comparing the simplified expressions given in Eqs. (6.1) and (6.2). We can see that one can write

$$\begin{aligned} P_{\mu\mu}^{approx} = 1 \; & - \sin^2\theta_{13}^M \sin^2 2\theta_{23} \sin^2 \frac{[(\Delta m_{31}^2 + A) - (\Delta m_{31}^2)^M]L}{8E_\nu} && (6.6) \\ & - \cos^2\theta_{13}^M \sin^2 2\theta_{23} \sin^2 \frac{[(\Delta m_{31}^2 + A) + (\Delta m_{31}^2)^M]L}{8E_\nu} \\ & - \sin^2\theta_{23} P_{e\mu}^{approx} \,. && (6.7) \end{aligned}$$

We note that $P_{e\mu}$ appears with a negative sign in the approximate expression for $P_{\mu\mu}$. Since the resultant muon flux at the detector is a *sum* of the $P_{\mu\mu}$ and $P_{e\mu}$ probabilities multiplied by the corresponding atmospheric neutrino fluxes, the contribution to earth matter effects coming from $P_{\mu\mu}$ get partially cancelled with that coming from $P_{e\mu}$. In Fig. 6.2 this is reflected in the reduction of $|\Delta X|$ when going from the toy case where only $P_{\mu\mu}$ driven events were considered (blue dot-dashed lines) to the realistic case where both $P_{\mu\mu}$ and $P_{e\mu}$ are taken (red dotted lines) into account. In particular, for the $L = 7202$ km case, the ΔX changes from -0.2 to -0.1 at $E_\mu \simeq 5-6$ GeV. From the figure one can see the reduction in mass hierarchy sensitivity for other baselines as well.

Finally, we impose the muon energy resolution on the event sample. This, as expected, brings about a further smearing of the energy spectrum. We use a Gaussian energy resolution function for the muons as given by Eq. (4.2). We show the impact of this smearing in Fig. 6.2 by the cyan long-dashed lines ($\sigma_{E_\mu} = 0.02E_\mu$) and the pink short-dashed lines ($\sigma_{E_\mu} = 0.15E_\mu$). The effect of putting the muon energy resolution function is obviously to further smear the energy spectrum and the higher the σ_{E_μ}/E_μ, the higher will be the smearing, as seen in the figure. Nevertheless, we can see that even after imposing the energy resolution we have a residual ΔX which can be used to distinguish the normal from the inverted hierarchy. It is this final residual ΔX which translates into the $\Delta\chi^2$ for the wrong neutrino mass hierarchy in our statistical analysis.

6.2.2 Earth Matter Effects in Hadron Events

The charge current interaction of ν_μ in the detector produces a hadron (or a bunch of hadrons) in addition to the muon. While the muon moves over long distances making long tracks in the detector, the hadron(s) produce(s) a shower. The INO collaboration has performed their first set of simulations studying the response of the ICAL detector to hadrons. The results showing the calibration of the detector to hadron energy and the corresponding hadron energy resolution have been presented in [41]. The study of the hadron response of the MONOLITH detector proposal was made in detail, both in computer simulations as well as by putting the prototype in a test beam [81, 82]. The energy and angle resolution of the hadron shower has also been studied extensively by the MINOS collaboration. In all works so far, the information from the hadrons have been used to reconstruct the neutrino energy and angle. However, we propose a different method of treating the hadron data. We will take the hadron data at par with the muon data and add their contribution to the statistical analysis of the mass hierarchy sensitivity of the magnetized iron detector.

In order to add the hadron contribution to the mass hierarchy sensitivity, we first need to bin the hadron data in a suitable way. In this analysis we treat the hadron event sample of magnetized iron detectors as follows. Since every hadron shower is associated with a corresponding muon coming from the same charged current interaction vertex of the neutrino, we use the muon as a tag for the hadron event. Since the muon zenith angle is reconstructed extremely well, we tag the hadron with the zenith angle of the corresponding muon. This means that for every muon in a given muon zenith angle bin, we group together all the corresponding hadrons. We next bin this group in terms of the hadron energy. Note that the most obviously way to calculate the true energy in the hadrons would be by adding up the energy of the hadrons in the final state for each event. When handling real data, this is what will be done. However, in our analysis we do not have real data. We only use the output of the event generator as our simulated data. Here a complication arises due to the fact that the final state provided by NUANCE has a large number of additional hadrons, which come from the breaking of the iron nucleus. Hence, adding them all up does not directly help in finding the energy released in the hadron due to the charged current interaction. Therefore instead of doing that, we calculate $E_H = E_\nu - E_\mu$, where E_ν is the true energy of the incoming neutrino and E_μ is the true energy of the muon, provided by the event generator. We call E_H the true energy in the hadrons. Having calculated the energy of all the associated hadrons in a given muon zenith angle bin, we redistribute these events in hadron energy bins, starting from 0.5 GeV to 10.5 GeV.

Following this methodology for hadron binning, the number of hadron events in each hadron energy bin can be written as

$$H_i^{\prime th}(\mu^-) = \mathscr{N} \sum_i \int_{E_H^{min}}^{E_H^{max}} dE'_H \int_{\cos\Theta_\mu^{min}}^{\cos\Theta_\mu^{max}} d\cos\Theta'_\mu \; R_{E_H} R_\Theta \, \mathscr{E}_i^H \left(\mathscr{E}_i \mathscr{C}_i \, h_i(\mu^-) + \overline{\mathscr{E}}_i (1 - \overline{\mathscr{C}_i}) \, h_i(\mu^+) \right) \tag{6.8}$$

Since we use the muon events as a tag and calculate the hadron energy binned data for every muon zenith angle bin, we calculate the hadron events corresponding to the μ^- events (denoted as $h_i(\mu^-)$ in Eq. (6.8)) as well as the ones associated with the μ^+ mis-identified as μ^- (denoted as $h_i(\mu^+)$ in Eq. (6.8)). The quantities $\mathscr{C}_i$ and $\overline{\mathscr{C}_i}$ are the charge identification efficiencies of μ^- and μ^+ events, respectively, as defined in Eq. (4.1). The reconstruction efficiency of the hadron shower is given by $\mathscr{E}^H$, and in this analysis it is taken to be the same for hadrons associated with both μ^- and μ^+. In the way we are handling the hadron events, we also multiply our events with $\mathscr{E}_i$ and $\overline{\mathscr{E}}_i$ for the μ^- and μ^+ events respectively, since we first look at events which already have a muon track reconstructed. From this set of events we find the subset for which even the hadron shower can be reconstructed. R_{E_H} is the energy resolution function of the hadrons, for which we use a Gaussian function similar to Eq. (4.2)

$$R_{E_H} = \frac{1}{\sqrt{2\pi}\sigma_{E_H}} \exp\left(\frac{-(E'_H - E_H)^2}{2\sigma_{E_H}^2}\right), \tag{6.9}$$

where E_H and E'_H correspond to the true energy and measured energy of the hadrons respectively. We need to put R_Θ which is the muon zenith angle resolution given by Eq. (4.3) in the above since the hadrons are binned inside the muon zenith angle bin. Note that the Eq. (6.8) gives the data binned in hadron energy only. When we bin the data in both the hadron energy as well as zenith angle, we will have to introduce the integral for the measured hadron angle bin and the corresponding hadron angle resolution function. We will discuss this later in section 6.4.2.

In Fig. 6.3 we show this binned data for the hadrons for four muon zenith angle bins corresponding to path lengths of $L = 7202$ km (top left panel), $L = 9110$ km (top right panel), $L = 11019$ km (bottom left panel), and $L = 12611$ km (bottom right panel). The hadron energy spectrum, without putting any energy resolution is shown by the blue dot-

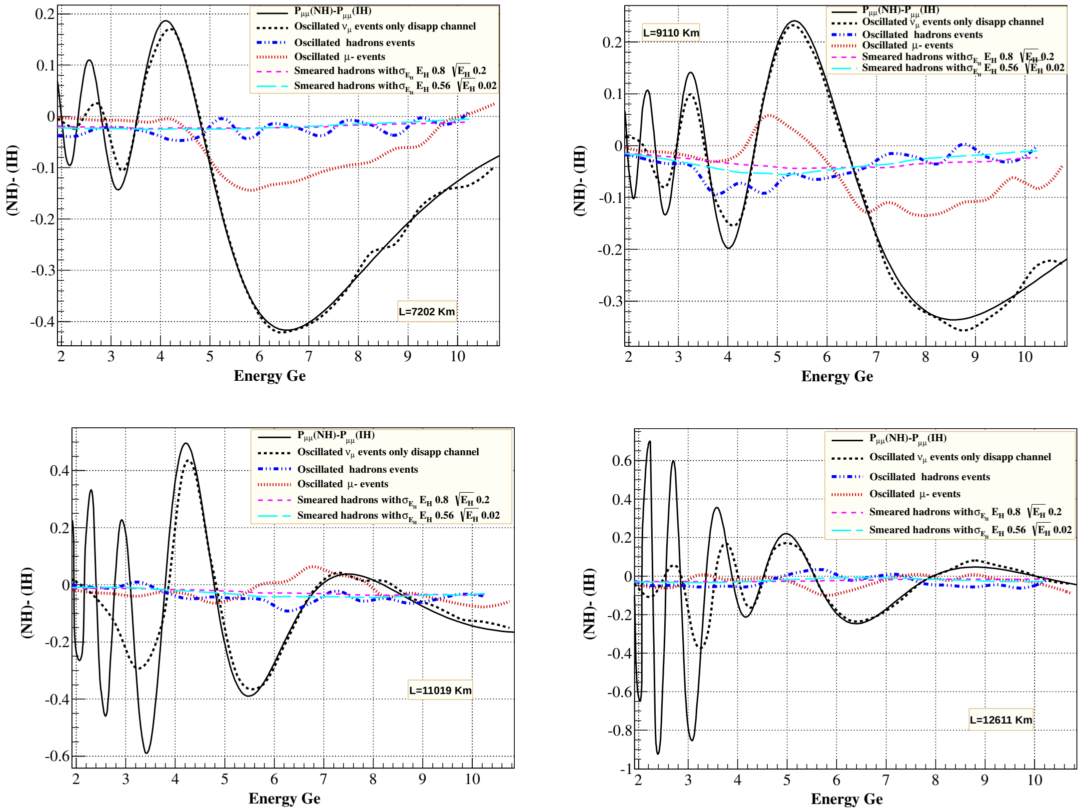

Figure 6.3: The difference in the predicted hadron event rates for normal and inverted hierarchy, normalized to the no-oscillation hadron event rate, shown as a function of energy. The four panels show the event spectrum generated in four zenith angle bins, marked by the path-length traversed at the mid-point of the bin. The solid black lines, black dashed lines and red dotted lines show the things as in Fig. 6.2. The black dashed lines give the difference between the predicted rate for normal and inverted hierarchy when only the $P_{\mu\mu}$ (disappearance) channel is taken and data binned in neutrino energy. The blue dot-dashed lines show the corresponding difference when only the $P_{\mu\mu}$ channel is taken and data binned in muon energy. The red dotted lines are obtained when we add the $P_{e\mu}$ (appearance) channel and bin the data in muon energy. The pink dashed and cyan long dashed lines are obtained when we apply on the red dotted lines the muon energy resolution functions with widths $\sigma_{E_\mu}/E_\mu = 0.15\%$ and 2%, respectively.

dashed lines in Fig. 6.3. We can see that even for the hadrons $\Delta X < 0$ predominantly, for all hadron energies. In fact, we can see that $\Delta X \simeq -0.05$ for a wide range of hadron energies, for all muon zenith angle bins. The pink short-dashed and the cyan long-dashed lines show the hadron spectrum smeared by $\sigma_{E_H}/E_H = 0.8/\sqrt{E_H} + 0.2$ and $\sigma_{E_H}/E_H = 0.56/\sqrt{E_H} + 0.02$, respectively. Since the shape of the hadron energy spectrum shown by the blue dot-dashed lines was anyway almost flat, the further smearing of spectrum due to the finite energy resolution of the detector does not bring about any drastic change in the spectral shape. Indeed the spectra for $\sigma_{E_H}/E_H = 0.8/\sqrt{E_H} + 0.2$ and $\sigma_{E_H}/E_H = 0.56/\sqrt{E_H} + 0.02$ look almost identical to each other. As in Fig. 6.2, the black solid lines in all the panels show the $\Delta P_{\mu\mu}$ at the probability level. Likewise, the black dashed lines correspond to difference in the event spectrum between normal and inverted hierarchies in terms of the neutrino energy with only the disappearance channel. The red dotted lines in all the panels show the event spectrum in terms of the true muon energy, where we have included events from both the disappearance as well as appearance channels but have not incorporated the muon energy resolutions. These lines again are the same as the red dotted lines in Fig. 6.2. Therefore, the black solid lines, black dashed lines and the red dotted lines and have been shown here again for comparison of the hadron spectrum with the corresponding neutrino and the muon spectra.

6.2.3 Earth Matter Effects in Neutrino Events

If the data is classified in terms of the neutrino energy and zenith angle, then the event spectrum is given as

$$N_i^{\prime th}(\nu) = \mathcal{N} \sum_i \int_{E_\nu^{min}}^{E_\nu^{max}} dE'_\nu \int_{\cos\Theta_\nu^{min}}^{\cos\Theta_\nu^{max}} d\cos\Theta'_\nu \; R_{E_\nu} R_{\Theta_\nu} \left(\mathcal{E}_i^\nu \mathcal{C}_i n_i(\nu) + \overline{\mathcal{E}}_i^\nu (1 - \overline{\mathcal{C}_i}) n_i(\nu) \right) \tag{6.10}$$

where all quantities are similar to those defined for the μ^- events in Eq. (6.10) with the only difference that they now correspond to the neutrinos rather than to the muons. The

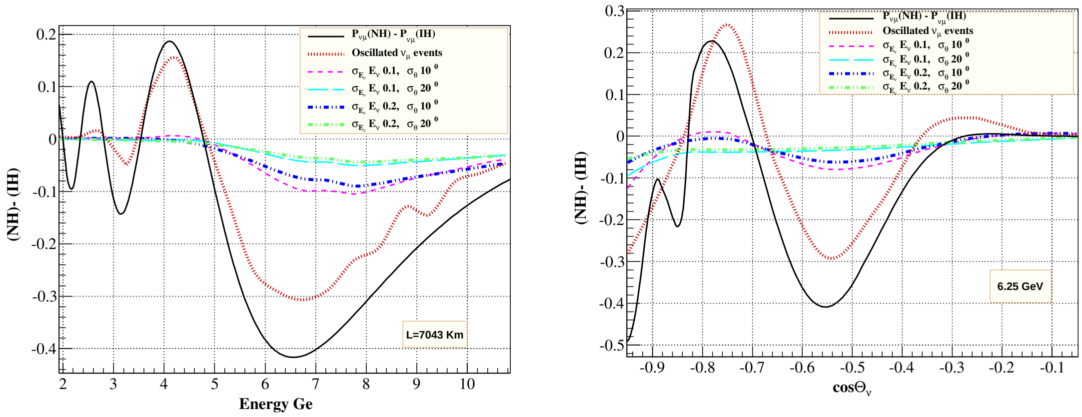

Figure 6.4: The difference in the predicted neutrino event rates for normal and inverted hierarchy, normalized to the no-oscillation neutrino event rate, shown as a function of energy. The left panels shows the energy dependence of the hierarchy sensitivity, where the events are generated in the zenith angle bin marked by the path-length traversed at the mid-point of the bin. The right panel shows the corresponding plot as a function of the neutrino zenith angle in the energy bin corresponding to neutrino energy of 6.25 GeV. The solid black lines show the $\Delta P_{\mu\mu}$ as in Fig. 6.2. The red dotted lines show the difference in the neutrino energy spectrum when no detector resolutions are added. The pink dashed, cyan long-dashed, blue dot-dashed and green dot-dashed lines show how the hierarchy sensitivity in the the neutrino spectrum changes as we include the detector resolutions in neutrino energy and neutrino zenith angle.

charge identification efficiency is the only one which will be identical in the two cases. The resolution functions R_{E_ν} and R_{Θ_ν} are also taken as Gaussian and their expression same as given for the muons but with the energy and angle resolution widths replaced by the corresponding ones for the neutrinos. A similar expression for the antineutrino events can also be written.

The difference in the neutrino event spectrum between the normal and inverted hierarchy normalized to the no-oscillation event rate is presented in Fig. 6.4. The left panel of the figure shows the difference $\Delta X = X(NH) - X(IH)$ between the neutrino events for normal and inverted hierarchies as a function of the neutrino energy in the zenith angle bin corresponding to $\cos\Theta_\nu = -0.55$. The right panel shows the ΔX as a function of the neutrino zenith angle for the energy bin corresponding to 6.25 GeV. The black lines in the figure show the $\Delta P_{\mu\mu}$, as before. The red dotted line is the observed neutrino event spectrum obtained when we take both the disappearance ($P_{\mu\mu}$) as well as appearance ($P_{e\mu}$) channels into account. Note that as in the case of the muons, the inclusion of the appearance channel spoils the extent of hierarchy sensitivity in the neutrino spectrum. Yet, it is evident from a comparison of the Figs. 6.2 and 6.4 that the net hierarchy sensitivity at this stage is greater in the neutrino case. The reason is because in the case of the muons there was a smearing of the spectral shape due to the kinematic averaging of the oscillation effects due to the interaction cross-section. However, the muon events have an advantage that the zenith angle of the muons can be very accurately reconstructed. Hence any further deterioration in the sensitivity comes mainly from the energy resolution of the muons. In the case of the neutrinos, both the energy as well as the zenith angle dependence of the signal gets smeared due to the finite detector resolutions. We show the impact of the resolution functions for four benchmark cases, $\sigma_{E_\nu}/E_\nu = 10\%,\ \sigma_{\Theta_\nu} = 10^\circ$ (pink dashed lines), $\sigma_{E_\nu}/E_\nu = 10\%,\ \sigma_{\Theta_\nu} = 20^\circ$ (cyan long-dashed lines), $\sigma_{E_\nu}/E_\nu = 20\%,\ \sigma_{\Theta_\nu} = 10^\circ$ (blue dot-dashed lines), and $\sigma_{E_\nu}/E_\nu = 20\%,\ \sigma_{\Theta_\nu} = 20^\circ$ (green dot-dashed lines). The figure shows that the impact of the resolution functions on the net hierarchy dependence is sharp. While both the energy as well as the angular resolutions result in reducing the hierarchy effect, the role of the angle resolution can be seen to be greater. It should be mentioned here that the benchmark resolution functions used here for illustration, range from being realistic to rather optimistic. Once we include these resolution functions, the $\Delta X \simeq -0.05$ to -0.1, depending on the values of the widths of the resolution functions. Comparison with the Fig. 6.2 reveals that the ΔX which we are getting with the neutrino spectrum are in general of the same order or even lower than what we had obtained using the events binned in muon energy and zenith angle. Therefore, as we will see also from the χ^2 analysis later, that the analysis of the neutrino data fails to give a $\Delta\chi^2$ for the wrong hierarchy better than that obtained from the muon analysis, unless one assumes extremely optimistic resolution functions for the neutrino.

6.3 Mass Hierarchy Sensitivity with only Muon Events

We begin with the analysis of only the muon event sample of the experiment. The mass hierarchy sensitivity of ICAL@INO using muon events was studied in detail by the INO collaboration and discussed in chapter 5. The detector specification used in that work was the ones obtained from detailed simulations of the ICAL detector using Geant-based detector simulation codes. These are however the first set of simulation results coming from dedicated studies of the ICAL detector performance. The study of the ICAL detector response to muons is still on-going. Therefore, it is expected that these results will be further refined and improved upon. Hence it is pertinent at this point to study how much the mass hierarchy sensitivity of ICAL@INO or any other similar detector could be improve with the improvement in the detector response to muons.

The muon reconstruction efficiency, charge identification efficiency, energy and angle resolutions were seen to be a function of both the muon energy as well as zenith angle (4). A snap-shot of the detector response to muons was shown Fig. 1 of 5. One can see from these plots that the reconstruction efficiency of the muons is roughly in the ballpark of 80-90% over most of the energy and zenith angle range of the muons, while the charge identification range is mostly around 99%. The zenith angle resolution of the muons is seen to be around 0.01 in $\cos\Theta_\mu$ from these plots, while the the energy resolution is seen to be around 10%-15%. While the zenith angle resolution of the detector found from the first set of simulations is seen to be extremely good, the energy resolution could be improved upon.

Since it appears that the energy resolution of the muons might have room for improvement in the future, in what follows we will study the improvement expected in the mass hierarchy sensitivity of magnetized detector such as ICAL@INO, as we improve the muon energy resolution. To clearly show the impact of better muon energy resolution on the mass hierarchy, we assume all other detector performance parameters fixed at a plausible value. In particular, we take muon charge identification efficiency $\mathscr{C} = 99\%$ and muon zenith angle resolution in $\cos\Theta_\mu$ of $\sigma_{\Theta_\mu} = 0.01$. These values more-or-less agree with the values obtained by the INO collaboration from detailed simulations, however we take them to be flat over all muon energy and zenith angle bins. The muon reconstruction efficiency could change depending on the cuts imposed on the data to improve the muon energy resolution. Hence, we also work with different muon reconstruction efficiency. The muon reconstruction efficiency and the muon energy resolution is also taken to be flat over all bins. We also take all detector specifications to be the same for μ^- and μ^+ events.

To see how well the mass hierarchy can be determined at this experiment we simulate the data for normal mass hierarchy at the values of the oscillation parameters given in Table 6.1. This data is then fitted with the wrong inverted hierarchy using a binned χ^2 analysis.

The χ^2 function and the systematic uncertainties are already defined in chapter 4. All results presented in this analysis are for 50×10 kton-yrs of exposure of the experiment. The difference $\Delta\chi^2 = \chi^2(IH) - \chi^2(NH)$ is used as a measure of the mass hierarchy sensitivity of the experiment.

A discussion on the number of muon bins N_b^μ is in order. In chapter 5 it was shown that for the excellent zenith angle resolution of the ICAL@INO detector, it makes sense to use 80 $\cos\Theta'_\mu$ bins of width 0.025, which is somewhat congruent with the width of the resolution function. In this work, since we have used a zenith angle resolution for the muons of 0.01 which is in the same ballpark as that obtained in the INO simulations, we continue to bin the muon zenith angle in 80 bins. Likewise, the energy bins should also correspond to the width of the energy resolution function. For the energy resolution obtained by the INO collaboration, 20 energy bins of width 0.5 GeV was seen to be optimal in chapter 5. However, in this work we work with varying muon energy resolution. In particular, we vary σ_{E_μ}/E_μ between 2% and 20%. In order to see the full impact of the improved energy resolution of 2%, we bin the energy spectrum into 80 bins as well. We realize that binning the atmospheric neutrino events with 50×10 kton-year exposure in 80×80 bins will reduce the number of events drastically in each bin. However, first, we use the Poissonian definition for the χ^2 function which can consistently calculate the χ^2 even for very small event rates. Second, we take a purely phenomenological stance in this analysis that if needed one could suitably increase the exposure of the experiment to compensate for the increased number of bins. And last but not the least, the experimental collaboration would perform an unbinned likelihood analysis of the data and in that case their statistical significance would roughly match with ours. Therefore, in this section we keep the number of energy bins fixed at 80 between 1 GeV and 11 GeV. However, in the next section when we combine the χ^2 corresponding to the hadron data with that of the muon data, then we present results for both 80 bins as well as 20 bins between 1 GeV and 11 GeV.

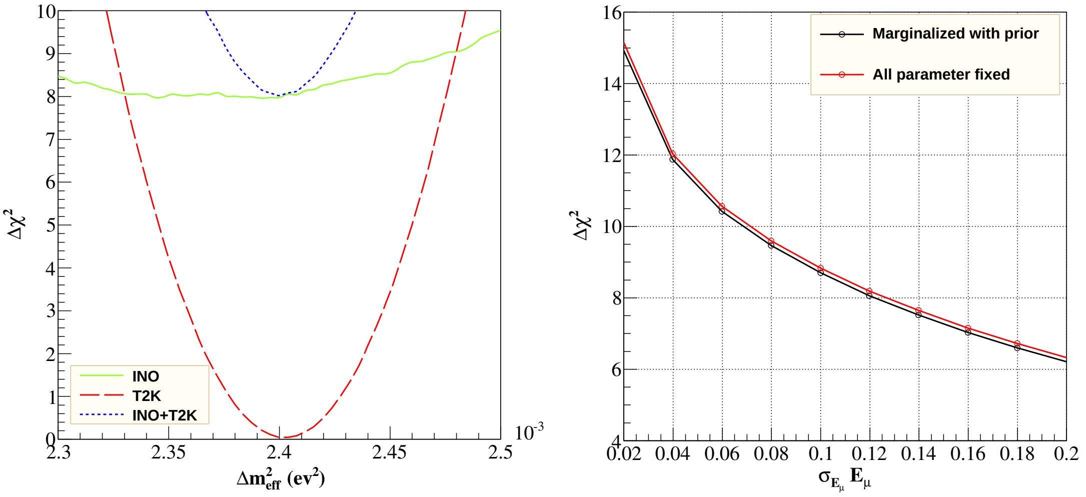

Figure 6.5: Left panel shows the $\Delta\chi^2$ for inverted hierarchy as a function of $|\Delta m^2_{\rm eff}|$ in the fit. This $\Delta\chi^2$ is marginalized over $\sin^2\theta_{13}$ and $\sin^2\theta_{23}$ as explained in the text. The green solid line shows the dependence of $\Delta\chi^2$ for the ICAL@INO like experiment, the red dotted line shows the corresponding dependence for T2K, while the blue dashed line shows the behavior coming from the combined fit of T2K and ICAL@INO like experiment. The data for all cases was generated for the values given in Table 6.1 and for normal hierarchy. Right panel shows the marginalized $\Delta\chi^2$ for inverted hierarchy as a function of σ_{E_μ}/E_μ. The black solid line shows the $\Delta\chi^2$ marginalized over $|\Delta m^2_{\rm eff}|$, $\sin^2\theta_{13}$ and $\sin^2\theta_{23}$ while the red solid line shows the $\Delta\chi^2$ for fixed parameters.

In the left panel of Fig. 6.5 we show $\Delta\chi^2$ as a function of the test $|\Delta m^2_{\rm eff}|$ for the inverted hierarchy. The green solid line shows the dependence of $\Delta\chi^2$ for the ICAL@INO like experiment, the red dotted line shows the corresponding dependence for T2K, while the blue dashed line shows the behavior coming from the combined fit of T2K and ICAL@INO like experiment. The data for all cases was generated for the values of oscillation parameters given in Table 6.1 and for normal hierarchy. In particular, the true value of $\Delta m^2_{\rm eff} = 2.4\times10^{-3}$ eV^2. For ICAL@INO like experiment we take 12% energy resolution and 80% reconstruction efficiency for this figure. For T2K we use the standard configuration and the GLoBES [76] software for generating the events. As expected, the T2K data alone has almost no mass hierarchy sensitivity. However, it plays a major role in fixing the value of the best-fit $|\Delta m^2_{\rm eff}|$ in the fit. Notice that for T2K the best-fit $|\Delta m^2_{\rm eff}|$ comes at 2.4×10^{-3} eV^2, since by definition $\Delta m^2_{\rm eff}$ is the value of the mass squared difference such that $P_{\mu\mu}$ calculated for $\Delta m^2_{\rm eff} > 0$ (NH) and $\Delta m^2_{\rm eff} < 0$ (IH) are almost the same, in the absence of earth matter effects. Since T2K has almost no earth matter effects, we find that the true $|\Delta m^2_{\rm eff}|$ and the best-fit $|\Delta m^2_{\rm eff}|$ are almost the same of T2K. However, for the ICAL@INO like experiment, best-fit $|\Delta m^2_{\rm eff}|$ comes at a slightly lower shifted value, mainly due to earth matter effects. In principle, this mismatch between different sets of experiments that could potentially measure the atmospheric mass squared difference can be used to determine the neutrino mass hierarchy [83]. In particular, if the combined analysis of different data sets results in a best-fit $|\Delta m^2_{\rm eff}|$ which is different from the best-fit $|\Delta m^2_{\rm eff}|$ preferred by the individual experiments, then the $\Delta\chi^2$ for mass hierarchy obtained from each of the experiments will be higher than what one got when analyzing them separately. This synergy could lead to an enhanced sensitivity to the neutrino mass hierarchy, as shown very recently in the context of PINGU data combined with that from JUNO [83]. However, unlike PINGU which has very good sensitivity to the absolute value of the mass squared difference, ICAL@INO has much poorer sensitivity to this parameter due to lower statistics. As a result the combined analysis of ICAL@INO with the long baseline experiment T2K gives a best-fit $|\Delta m^2_{\rm eff}|$ which is governed by the best-fit obtained for T2K. This can be seen in the left panel of Fig. 6.5, where even though the ICAL@INO data alone shows a preference for a slightly lower $|\Delta m^2_{\rm eff}|$ in the inverted hierarchy fit, the combined analysis of ICAL@INO data with the T2K data returns a best-fit $|\Delta m^2_{\rm eff}| \simeq 2.4 \times 10^{-3}$ eV^2. This value coincides with the true value adopted for generating the data as well as the best-fit value of $|\Delta m^2_{\rm eff}|$ for the T2K data alone. Therefore, as in the case of only T2K analysis, the $\Delta\chi^2$ contribution from T2K is almost zero even now. On the other hand, since the best-fit $|\Delta m^2_{\rm eff}|$ from the combined fit is slightly different from the best-fit $|\Delta m^2_{\rm eff}|$ from ICAL@INO analysis alone, one in principle expects an increase in the $\Delta\chi^2$ contribution from ICAL@INO. However, if we look at the only ICAL@INO line in the left panel of Fig. 6.5, we see that the difference between the $\Delta\chi^2$ at the best-fit $|\Delta m^2_{\rm eff}|$ from ICAL@INO alone and the best-fit

$|\Delta m^2_{\text{eff}}|$ from the combined analysis is almost negligible. Therefore, this change in the best-fit $|\Delta m^2_{\text{eff}}|$ brings no additional contribution to the mass hierarchy sensitivity in the context of an experiment like ICAL@INO. Hence in order to save computational time, in the rest of the paper we will keep the $|\Delta m^2_{\text{eff}}|$ fixed in the fit for ICAL@INO, since as we have seen in this figure that once the T2K data is included, the best-fit $|\Delta m^2_{\text{eff}}|$ will coincide with the true value of $|\Delta m^2_{\text{eff}}|$ assumed. Since the $\Delta\chi^2$ from ICAL@INO is insensitive to this small change in $|\Delta m^2_{\text{eff}}|$ from where the best-fit from ICAL@INO alone would be, we do not expect any noticeable correction to the mass hierarchy sensitivity. However, we stress that this is true only for a low statistics atmospheric neutrino experiment like ICAL@INO. For an atmospheric experiment like PINGU, this reasoning will not be true.

In order to further justify our choice of keeping the oscillation parameters fixed in the fit, we show in the right-hand panel of Fig. 6.5 a comparison of the $\Delta\chi^2$ obtained from ICAL@INO data, with and without keeping the parameters fixed in the fit. The red solid line corresponds to the $\Delta\chi^2$ obtained for fixed parameters analysis while the black solid corresponds to the $\Delta\chi^2$ obtained when the test values of $|\Delta m^2_{\text{eff}}|$, $\sin^2\theta_{23}$ and $\sin^2\theta_{13}$ are allowed to vary in the fit and the $\Delta\chi^2$ is marginalized over them. To obtain the black curve we impose projected priors on $|\Delta m^2_{\text{eff}}|$, $\sin^2 2\theta_{23}$ and $\sin^2\theta_{13}$, expected from the T2K, NOνA, Daya Bay, RENO and Double Chooz experiments. We take 1σ errors of 2%, 0.0065 and 0.005 on $|\Delta m^2_{\text{eff}}|$, $\sin^2 2\theta_{23}$ and $\sin^2\theta_{13}$, respectively. The $\Delta\chi^2$ obtained for the two cases are shown as a function of the muon energy resolution σ_{E_μ}/E_μ. We can see that for all values of σ_{E_μ}/E_μ, the $\Delta\chi^2$ obtained after marginalization over the oscillation parameters is almost the same as that obtained when we keep the oscillation parameters fixed in the fit. Therefore, our final $\Delta\chi^2$ is independent of whether we marginalize over the oscillation parameters or keep it fixed. And so, henceforth in the rest of the paper we keep the oscillation parameters fixed in the fit for inverted hierarchy.

The dependence of the mass hierarchy sensitivity to the muon energy resolution and

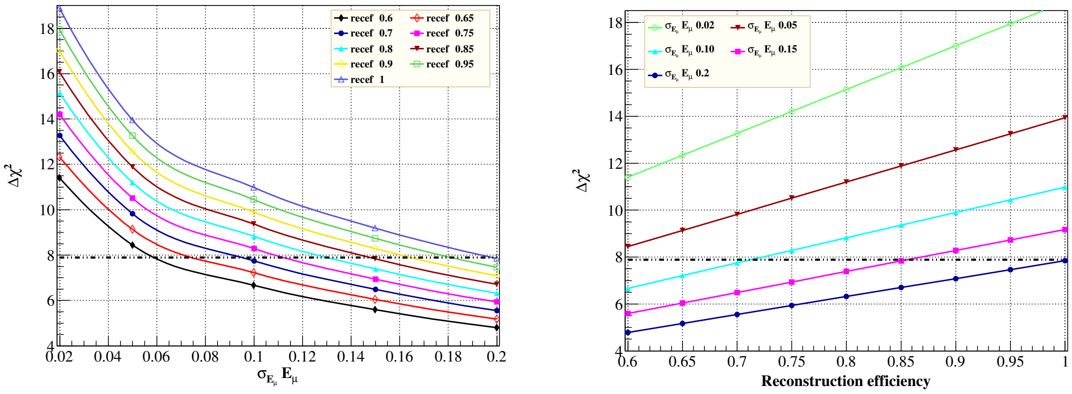

Figure 6.6: The $\Delta\chi^2$ corresponding to the mass hierarchy sensitivity as a function of the width of the muon resolution function (left panel) and muon reconstruction efficiency (right panel). We show this dependence for different fixed values of the reconstruction efficiency in the left panel and different fixed values of the width of the muon resolution function (right panel). The black dot-dashed lines in the figure show the $\Delta\chi^2$ obtained from the muon analysis performed in chapter 5, using the detector response to muons obtained by the INO collaboration.

muon reconstruction efficiency are shown in Figs. 6.6. In the left panel on Fig. 6.6 we show the $\Delta\chi^2$ as a function of the muon energy resolution σ_{E_μ}/E_μ, for different values of the muon reconstruction efficiency ε. We vary σ_{E_μ}/E_μ continuously between 20% and 2% and repeat this for $\varepsilon = 60\%$ to 100%. For a given ε, we see that the $\Delta\chi^2$ falls sharply as the σ_{E_μ}/E_μ is increased from 2% to about 6%. Thereafter, the rate of fall of $\Delta\chi^2$ reduces, and it falls steadily as σ_{E_μ}/E_μ worsens. As expected, $\Delta\chi^2$ is seen to increase with the reconstruction efficiency ε. For comparison, we show by the black dot-dashed lines in the figure, the $\Delta\chi^2$ obtained in chapter 5 using the full detector simulation results for the muon analysis.

In the right panel of Fig. 6.6 we show the $\Delta\chi^2$ as a function of the reconstruction efficiency ε, for different values of the muon energy resolution σ_{E_μ}/E_μ. The $\Delta\chi^2$ is seen to increase linearly with ε. This is not surprising as in the way we have included it in our analysis, ε linearly increases the statistics of the experiment. Since the mass hierarchy signal in an ICAL@INO like experiment for a 50×10 kton-yrs exposure is still in the statistics

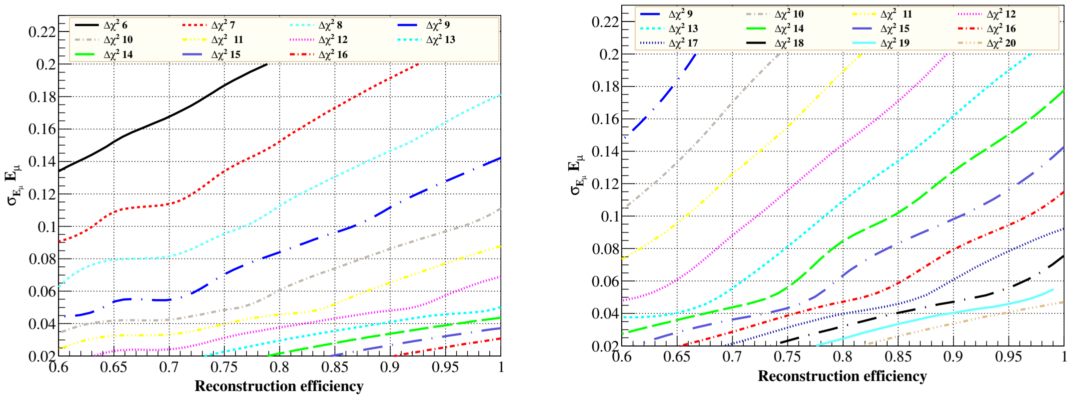

Figure 6.7: Constant $\Delta\chi^2$ contours in the reconstruction efficiency and energy resolution plane. The left panels shows the contours from the analysis which uses only the muon data from the experiments. The right panels shows the contours for the analysis in which both the muon and hadron data were included in the combined statistical analysis.

dominated regime, the $\Delta\chi^2$ grows linear with more data.

Finally, in the left panel of Fig. 6.7, we show contours of constant $\Delta\chi^2$ obtained in the reconstruction efficiency and energy resolution plane, from the analysis of the muon events in the detector. We show the contours for $\Delta\chi^2 = 6$ to 16. The figure shows that for energy resolution in the range of 2% to 3% and reconstruction efficiency above 90%, one would get a 4σ signal for the neutrino mass hierarchy from the analysis of the muon data alone. We reiterate the the reconstruction efficiency can be compensated by adjusting the exposure of the experiment. On the other hand, a 3σ measurement of the mass hierarchy from the muon analysis alone seems to be extremely plausible for reasonable range of values for the muon energy resolution and reconstruction efficiency.

6.4 Mass Hierarchy Sensitivity with Muon Plus Hadron Events

We had seen in Fig. 6.3 that the hadron events also exhibit a difference between the event rates expected for the normal and inverted hierarchy and hence carry mass hierarchy sensitivity to some extent. In this section, we quantify the improvement in the sensitivity expected in the mass hierarchy sensitivity of magnetized iron detectors if the hadron events were also added in the statistical analysis of the data. The total χ^2 function associated with the μ^- is then given by

$$\begin{aligned}\chi^2(\mu^- + hadron^-) &= \min_{\{\xi_j\}} \left[\sum_{i=1}^{N_b^\mu} \left\{ 2\left(N_i^{th}(\mu^-) - N_i^{ex}(\mu^-)\right) + 2N_i^{ex}(\mu^-)\ln\left(\frac{N_i^{ex}(\mu^-)}{N_i^{th}(\mu^-)}\right) \right\} \right. \\ &+ \left. \sum_{i=1}^{N_b^H} \left\{ 2\left(H_i^{th}(\mu^-) - H_i^{ex}(\mu^-)\right) + 2H_i^{ex}(\mu^-)\ln\left(\frac{H_i^{ex}(\mu^-)}{H_i^{th}(\mu^-)}\right) \right\} \right] + \sum_{j=1}^{k} \xi_j^2 , \end{aligned} \tag{6.11}$$

where N_b^μ and N_b^H are the total number of μ^- and hadron bins, respectively, $N_i^{ex}(\mu^-)$ and $H_i^{ex}(\mu^-)$ are the data in the μ^- and the associated hadrons, respectively, while the theoretical predictions are given as

$$H_i^{th}(\mu^-) = H_i^{\prime th}(\mu^-)\left(1 + \sum_{j=1}^{k} \eta_i^j \xi_j\right) + \mathcal{O}(\xi_k^2), \tag{6.12}$$

where $H_i^{\prime th}(\mu^-)$ is given by Eq. (6.8) and all other quantities are as defined in the previous section. Since the hadrons are tagged with their corresponding muon from the respective charged current interaction, we can distinguish between the hadrons associated with the μ^- from the ones associated with the μ^+. The $-$ sign as superscript in *hadron*$^-$ in Eq. (6.12) signifies that the hadrons implied there are ones associated with the μ^- events. Therefore, the combined χ^2 using all data is given by

$$\Delta\chi^2(\mu + hadron) = \Delta\chi^2(\mu^- + hadron^-) + \Delta\chi^2(\mu^+ + hadron^+) . \tag{6.13}$$

$N_{bin}^{E_\mu}$	σ_{E_μ}/E_μ	Muon Rec Eff	$\Delta\chi^2(\mu)$	$\Delta\chi^2(\mu + hadron)$		
				$\frac{\sigma_H}{E_H} = \frac{0.8}{\sqrt{E_H}} + 0.2$	$\frac{\sigma_H}{E_H} = \frac{0.68}{\sqrt{E_H}} + 0.02$	$\frac{\sigma_H}{E_H} = \frac{0.56}{\sqrt{E_H}} + 0.02$
20	0.12	70%	7.0	9.0	9.5	9.7
20	0.12	80%	8.0	10.3	10.8	11.0
20	0.12	90%	9.0	11.6	12.1	12.4
20	0.02	70%	10.2	12.2	12.6	12.8
20	0.02	80%	11.6	13.9	14.4	14.6
20	0.02	90%	13.0	15.6	16.2	16.4
80	0.02	70%	13.3	15.3	15.7	15.9
80	0.02	80%	15.1	17.5	18.0	18.2
80	0.02	90%	17.0	19.6	20.2	20.4

Table 6.2: The $\Delta\chi^2$ obtained for ruling out the wrong mass hierarchy obtained by combining the hadron data with the muon data, where we bin the hadron data in 10 equal hadron energy bins between $E_H = 0.5$ GeV and 10.5 GeV (1 GeV bins). The muons are binned in 80 zenith angle bins of width $\Delta\cos\Theta_\mu = 0.025$, while the energy bins for the muons are varied, and shown in the first column. The second column shows the muon energy resolution, third column gives the reconstruction efficiency, the fourth column the $\Delta\chi^2$ obtained using only the muon data, while the fifth, sixth and seventh columns give the $\Delta\chi^2$ from the combined analysis of the muon and the hadron data.

The hadron data is binned in the way described earlier in connection with the Fig. 6.3. We first present the results of the statistical analysis where the hadrons are binned in energy only (cf. Eq. (6.8). We then introduce the zenith angle resolution function of the hadron as well and further bins the data into hadron angles.

6.4.1 Hadron Data Binned in Energy Only

We present in Table 6.2 the improvement in $\Delta\chi^2$ we obtain by including the hadron energy binned data into our χ^2 analysis, where we bin the hadron data in 10 equal hadron energy bins between $E_H = 0.5$ GeV and 10.5 GeV (1 GeV bins). The combined $\Delta\chi^2(\mu + hadron)$ is shown in Table 6.2 for different cases of muon energy resolutions and reconstruction efficiencies, as well for different hadron energy resolutions. We show the sensitivity for three benchmark values of the muon reconstruction efficiency of 70%, 80% and 90%. The current ICAL@INO reconstruction efficiency corresponds to roughly 80-90%. The muon energy resolution is varied between 12%, the value obtained in the current simulations being performed by the INO collaboration, and 2%, which is the projected ambitious goal for this detector parameter. For 12% energy resolution we work with 20 muon energy bins between muon energy of 1 GeV and 11 GeV, which corresponds well with this value of the energy resolution. However, for the 2% energy resolution case we show the results for two choices of energy bins – 20 muon energy bins and 80 muon energy bins between muon energies of 1 GeV and 11 GeV. The choice of $N_{bin}^{E_\mu} = 80$ is commensurate with the very good energy resolution of 2% and should be the logical one to be used. However, we also show the results for the more conservative choice of $N_{bin}^{E_\mu} = 20$. For the hadron energy resolution we repeat our analysis for three benchmark choices :-

1. $\frac{\sigma_{E_H}}{E_H} = \frac{0.8}{\sqrt{E_H(GeV)}} + 0.2$. This is roughly the kind of hadron energy resolution that has been obtained by the INO collaboration through the Geant-based simulation of their detector response to hadrons.

2. $\frac{\sigma_{E_H}}{E_H} = \frac{0.68}{\sqrt{E_H(GeV)}} + 0.02$. This is the the hadron energy resolution obtained by testing an 8 ton prototype magnetized iron calorimetric detector equipped with 23 m^2 of glass Resistive Plate Chambers (RPC) with the T7-PS beam at CERN by the the MONOLITH collaboration [81].

3. $\frac{\sigma_{E_H}}{E_H} = \frac{0.56}{\sqrt{E_H(GeV)}} + 0.02$. This is the hadron energy resolution reported by the MINOS collaboration.

The results for these three different σ_{E_H}/E_H are presented in the last three columns of Table 6.2. A comparison of the $\Delta\chi^2(\mu)$ obtained from using only the muon data in the analysis (given in the fourth column of Table 6.2) with the $\Delta\chi^2(\mu + hadron)$ obtained by adding the corresponding hadron data to the muon data (given in the last three columns of Table 6.2) shows the increase in the mass hierarchy sensitivity of the experiment due to the contribution of the hadron data. For instance, we can see that with 80% muon reconstruction efficiency and 12% energy resolution, one gets $\Delta\chi^2(\mu) = 8.0$. On adding the hadron data this increases to $\Delta\chi^2(\mu + hadron) = 10.3 - 11.0$, depending on the hadron energy resolution of the detector. Therefore, we get a contribution of about 2-3 to the $\Delta\chi^2$ from just the hadron events in the detector. Since the hadron events are tagged with the muon events, an increase in the muon reconstruction efficiency brings about a corresponding increase in the statistics of the hadron events and hence an increase in the contribution of the hadron events to the mass hierarchy sensitivity. For 90% reconstruction efficiency, we see that hadron data gives a contribution of about 2.5-3.5 to the $\Delta\chi^2$. For 80% muon reconstruction efficiency, if we improve the muon energy resolution σ_{E_μ}/E_μ to 2%, the corresponding $\Delta\chi^2(\mu)$ increases to 11.6 for $N_b^{E_\mu} = 20$ bins and further to 15.1 for $N_b^{E_\mu} = 80$. On addition of the hadron events to the muon sample, the corresponding sensitivity reach numbers stand as 13.9-14.6 and 17.5-18.2, respectively. An increase of muon reconstruction efficiency to 90% will give $\Delta\chi^2(\mu) = 17$ and $\Delta\chi^2(\mu + hadron) = 19.6 - 20.4$ in the most optimistic cases of the muon resolutions of 2% with 80 muon energy bins. On the other hand, if we compare the increase in the $\Delta\chi^2$ as we change the hadron energy resolution σ_{E_H}/E_H, we find that the change is marginal. Indeed the Table 6.2 shows that in going from $\sigma_{E_H}/E_H = 0.8/\sqrt{E_H} + 0.2$ to $\sigma_{E_H}/E_H = 0.56/\sqrt{E_H} + 0.02$ the $\Delta\chi^2(\mu + hadron)$ changes by less than ~ 1.

6.4.2 Hadron Data Binned in Energy and Zenith Angle

The magnetized iron calorimeter is capable of measuring the angle of the hadron shower. In order to use the full energy and angle information on the hadrons in the analysis, we bin the data in both hadron energy as well as zenith angle. For every muon zenith angle bin, we bin the hadrons into 5 energy bins between $E_H = 0.5$ and 10.5 GeV of bin width 2 GeV and 5 zenith angle bins of bin width 36°. We smear the zenith angle binned data by the Gaussian smearing function R_{Θ_H} in addition to the smearing functions for the muon zenith angle resolution and hadron energy resolution shown in Eq. (6.8). The simulation results for the angular resolution of the hadron shower in ICAL are yet to be made public by the

$N_{bin}^{E_\mu}$	σ_{E_μ}/E_μ	σ_{Θ_H}	$\Delta\chi^2(\mu)$	$\Delta\chi^2(\mu+hadron)$		
				$\frac{\sigma_{E_H}}{E_H}=\frac{0.8}{\sqrt{E_H}}+0.2$	$\frac{\sigma_{E_H}}{E_H}=\frac{0.68}{\sqrt{E_H}}+0.02$	$\frac{\sigma_{E_H}}{E_H}=\frac{0.56}{\sqrt{E_H}}+0.02$
20	0.12	$\frac{16.67}{\sqrt{E_H}}+\frac{12.12}{E_H}$	8.0	11.3	12.1	12.5
20	0.12	$\frac{10.4}{\sqrt{E_H}}+\frac{10.1}{E_H}$	8.0	11.6	12.5	12.9
20	0.02	$\frac{16.67}{\sqrt{E_H}}+\frac{12.12}{E_H}$	11.6	14.9	15.7	15.4
20	0.02	$\frac{10.4}{\sqrt{E_H}}+\frac{10.1}{E_H}$	11.6	15.2	16.1	16.6
80	0.02	$\frac{16.67}{\sqrt{E_H}}+\frac{12.12}{E_H}$	15.1	18.8	19.3	18.9
80	0.02	$\frac{10.4}{\sqrt{E_H}}+\frac{10.1}{E_H}$	15.1	18.5	19.7	20.12

Table 6.3: The $\Delta\chi^2$ obtained for ruling out the wrong mass hierarchy obtained by combining the hadron data with the muon data, where we bin the hadron data in five equal hadron energy bins between $E_H = 0.5$ GeV and 10.5 GeV (2 GeV bins) and 5 equal hadron zenith angle bins between $\Theta_H = 0^\circ$ and 180° (36° bins). The muons are binned in 80 zenith angle bins of width $\Delta\cos\Theta_\mu = 0.025$, while the energy bins for the muons are varied, and shown in the first column. We have take the reconstruction efficiency as 80% for all cases in this Table. The second column shows the muon energy resolution, the third column the $\Delta\chi^2$ obtained using only the muon data, while the fourth, fifth and sixth columns give the $\Delta\chi^2$ from the combined analysis of the muon and the hadron data.

INO collaboration. Therefore, in what follows we will use the following two cases for the zenith angle resolution for the hadron shower:

1. $\sigma_{\Theta_H} = \frac{16.67}{\sqrt{E_H}} + \frac{12.12}{E_H}$, taken from the MINOS proposal.
2. $\sigma_{\Theta_H} = \frac{10.4}{\sqrt{E_H}} + \frac{10.1}{E_H}$, taken from the analysis of the MONOLITH prototype data in the T7-PS beam at CERN [82].

The results obtained by including the full energy as well as angle binned hadron data along with the muon data in the statistical analysis, are shown in Table 6.3. We find that the binning in hadron zenith angle brings in a further mild increase in the total $\Delta\chi^2$. The increase in the $\Delta\chi^2$ due to the introduction of the hadron events into the analysis is seen to be improving it by $\simeq 5$. With a 80% reconstruction efficiency and muon energy resolution of 2% one could get a total $\Delta\chi^2 \simeq 20$ (16) if one choose to work with 80 (20) muon energy bins.

The constant $\Delta\chi^2$ contours for the full data set in the reconstruction efficiency and muon energy resolution plane is shown in the right panel of Fig. 6.7. Here we have included the energy and zenith angle binned hadron data into the analysis with $\sigma_{E_H}/E_H = 0.68/\sqrt{E_H} + 0.02$ [81] and $\sigma_{\Theta_H} = 10.4/\sqrt{E_H} + 10.1/E_H$ [82]. The contours are shown $\Delta\chi^2 = 9$ to 20. We can see that getting a 3σ signal for the mass hierarchy becomes very easy for most values of the reconstruction efficiency and muon energy resolution once the hadron data is added. For muon energy resolution in the range of 2% to 10% and reconstruction efficiency greater than 65%, we should get 4σ sensitivity to the mass hierarchy. If the muon energy resolution is in the range of 2% to 4% and reconstruction efficiency above 80%, one would get a 4.5σ signal for the neutrino mass hierarchy from the analysis of the combined data.

6.5 Mass Hierarchy Sensitivity with Neutrino Events

As discussed before, the measured energy and angle of the muon, as well as the energy and angle of the hadron, can be combined to reconstruct the energy and zenith angle of the neutrino. The width of the corresponding energy and angle resolution was seen to be crucial when we presented the neutrino event spectrum in section 6.2.3. Here we show the statistical significance with which the wrong hierarchy can be ruled out by the neutrino analysis. The χ^2 is defined similar to what we had for the muon analysis (cf. Eq. (4.4)), with just the muon bins replaced by the neutrino bins. We show the results of our analysis in Fig. 6.8. The black solid line shows the $\Delta\chi^2$ obtained for the wrong hierarchy when we bin the data in 20 neutrino energy bins between 1 GeV and 11 GeV, and 20 zenith angle bins between -1 and $+1$. We have taken the neutrino reconstruction efficiency of 80% and charge identification efficiency of 99% in this figure. The neutrino energy resolution σ_{E_ν}/E_ν is taken as flat over all bins and is varied in the x-axis. The neutrino zenith angle

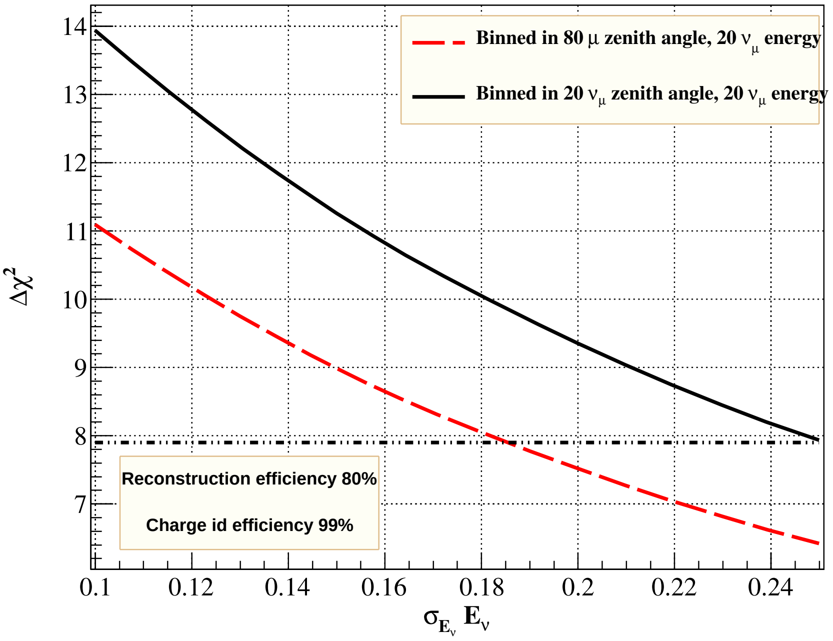

Figure 6.8: The $\Delta\chi^2$ corresponding to the mass hierarchy sensitivity as a function of the width of the neutrino resolution function. The black line shows the expected sensitivity when we use the binning in neutrino zenith angles with the neutrino zenith angle resolution function taken from the MONOLITH proposal [78]. The red dashed line shows the expected sensitivity when we use the binning in muon zenith angles with the muon zenith angle resolution width of 0.01 in $\cos\Theta_\mu$. The black dot-dashed lines in the figure show the $\Delta\chi^2$ obtained from the muon analysis performed in chapter 5, using the detector response to muons obtained by the INO collaboration.

resolution adopted in this figure has been taken from Fig. 4.7 of the MONOLITH proposal [78]. While the average of neutrino zenith angle resolution is around 11°, in the energy range of interest, the zenith angle resolution is seen to be around $5-7^\circ$. The neutrino energy resolution in this proposal is quoted as being around 20%. We can see from the figure that at 20% energy resolution $\Delta\chi^2 \simeq 9.4$ from this analysis. [1] This is comparable to the sensitivity obtained with just the muon data with 80% efficiency and energy resolution of 12%. If the hadron data is added to the muon data, then even with these modest detector response for the muons, we would get $\Delta\chi^2 \simeq 12-13$ (cf. Table 6.3). If the muon energy resolution was improved to 2%, then we would have a more than 4σ sensitivity to the mass hierarchy from the muon-plus-hadron analysis. Whereas, from the Fig. 6.4 we can see that the sensitivity from the neutrino analysis can never match these numbers, even for extremely optimistic energy resolution of 10%. The reason can be traced to the event rates plots shown in Figs. 6.2, 6.3 and 6.4. The effect of the detector resolutions on the neutrino spectrum make it comparable, and sometimes even worse than the muon spectrum. If we add the hadron spectral data to the muon spectral analysis, we get an additional contribution to the hierarchy sensitivity which cannot be matched by the neutrino analysis.

For comparison, in Fig. 6.8 we also show the $\Delta\chi^2$ obtained when we bin the data in neutrino energy and muon zenith angle bins. We keep the reconstruction efficiency at 80% and charge identification efficiency at 99%. The muon zenith angle resolution function is taken with width 0.01. We see that the $\Delta\chi^2$ obtained in this case is even worse than what we had obtained with the neutrino zenith angle analysis using the MONOLITH zenith angle resolution function.

In next chapter, we show the sensitivity of ICAL@INO in measuring the mixing angle θ_{23} and atmospheric mass squre difference Δm^2 precisely.

---

[1] For a flat 10% neutrino energy resolution and 10° zenith angle resolution function, we obtain $\Delta\chi^2 = 10.4$ from the neutrino analysis.

CHAPTER 7

THE REACH OF INO FOR ATMOSPHERIC NEUTRINO OSCILLATION PARAMETERS

In this chapter, we explore in detail the potential for measuring the neutrino parameters θ_{23} and $|\Delta m^2_{eff}|$ (defined in chapter 5) in the ICAL@INO experiment using atmospheric neutrinos. The precision on both these parameters is expected to improve from data coming from the currently operating and soon-to-start experiments using accelerator-based neutrino beams (MINOS, T2K and NOνA) as well as atmospheric neutrinos (at Super-Kamiokande and IceCube Deep Core). This analysis is based on the numerical procedure discussed in chapter 4 and we have used muon events where the range of muon zenith angle is from -1 to +1 with binwidth 0.025 and the range of muon energy is 0.8GeV to 10.8 GeV with binwidth is 0.5 GeV.

We use the oscillation parameters described in Table 7.1 and take the exposure to be 50 kt

× 10 years.

Since in this analysis we are mainly interested in constraining θ_{23} and $|\Delta m^2_{eff}|$, and the variation of θ_{12} or $|\Delta m^2_{21}|$ within the current error bars is observed not to affect the results, we take the value of these two parameters to be fixed to those given in Table 7.1. On the parameter $\sin^2 2\theta_{13}$, we impose a prior to allow for the uncertainty in its current measurement :

$$\chi^2 = \chi^2_{\rm ino} + \left(\frac{\sin^2 2\theta_{13}(\rm true) - \sin^2 2\theta_{13}}{\sigma_{\sin^2 2\theta_{13}}} \right)^2 , \tag{7.1}$$

where $\sigma_{\sin^2 2\theta_{13}}$ is the current 1σ error on $\sin^2 2\theta_{13}$, and is taken as 0.013 in our analysis. Of course, during the operation of INO, the error $\sigma_{\sin^2 2\theta_{13}}$ will decrease, and within a few years, $\sin^2 2\theta_{13}$ may be considered to be a fixed parameter.

Parameter	$\sin^2 2\theta_{12}$	$\sin^2 2\theta_{23}$	$\sin^2 2\theta_{13}$	Δm^2_{21} (eV^2)	$\lvert\Delta m^2_{eff}\rvert$ (eV^2)	$\delta_{\rm CP}$	Hierarchy
True Value	0.86	1.0	0.1	7.5×10^{-5}	2.4×10^{-3}	0.0	Normal

Table 7.1: True values of the neutrino oscillation parameters used in this analysis

7.1 Precision Measurement of $\sin^2\theta_{23}$ and $|\Delta m^2_{eff}|$

We start by presenting the reach of the ICAL for the parameters $\sin^2\theta_{23}$ and $|\Delta m^2_{32}|$ separately. The true values of all parameters are given in Table 7.1. Note that we use the parameter Δm^2_{eff} (defined in chapter 5) instead of $|\Delta m^2_{31}|$. The χ^2 values as functions of $\sin^2\theta_{23}$ and $|\Delta m^2_{eff}|$ are shown in figs. 7.1 and 7.1, respectively. Note that the minimum value of χ^2 vanishes, since MC fluctuations in the observed data have been reduced due to the scaling from an exposure of 50 kt × 1000 years. The precision on these parameters may be quantified by

$$\text{precision} = \frac{p_{max} - p_{min}}{p_{max} + p_{min}} , \tag{7.2}$$

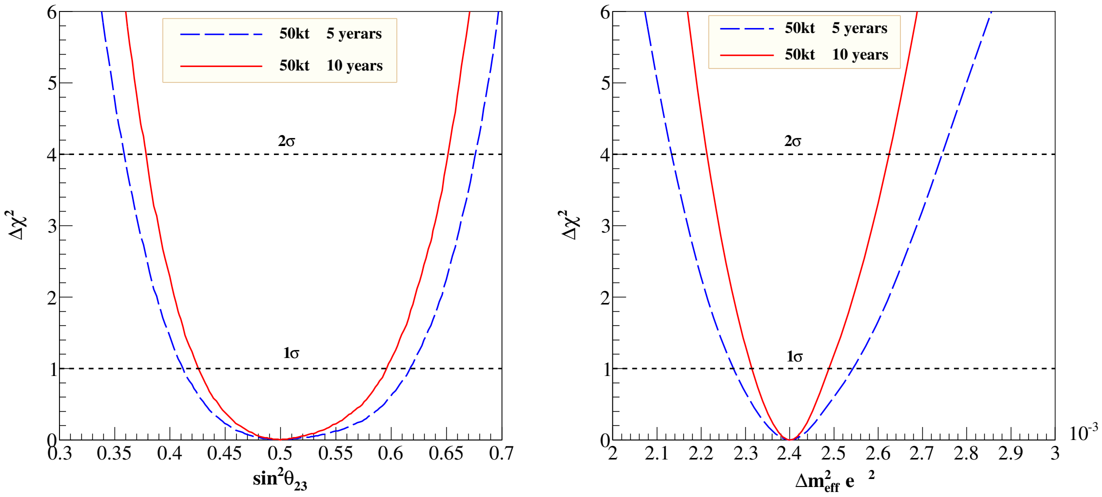

Figure 7.1: The panel (a) shows the χ^2 as a function of $\sin^2\theta_{23}$ for $|\Delta m^2_{eff}| = 2.4 \times 10^{-3}$ eV^2 and $\sin^2\theta_{23}(\text{true}) = 0.5$. The panel (b) shows the χ^2 as a function of $|\Delta m^2_{eff}|$ for $\sin^2\theta_{23} = 0.5$ and $|\Delta m^2_{eff}|(\text{true}) = 2.4 \times 10^{-3}$ eV^2

where p_{max} and p_{min} are the largest and smallest value of the concerned oscillation parameters determined at the given C.L. from the atmospheric neutrino measurements at ICAL for a given exposure. We find that after 5 years of running of this experiment, ICAL would be able to measure $\sin^2\theta_{23}$ to a precision of 20% and $|\Delta m^2_{eff}|$ to 5.4% at 1σ. With 10 years exposure, these numbers improve to 16% and 2.9% for $\sin^2\theta_{23}$ and $|\Delta m^2_{eff}|$, respectively. The precision on $\sin^2\theta_{23}$ is mainly governed by the muon reconstruction efficiency and is expected to improve with it. It will also improve as the systematic errors are reduced. On the other hand, the precision on $|\Delta m^2_{eff}|$ is governed by the ability of the detector to determine the value of L/E for individual events accurately. This depends on the energy- and $\cos\theta$- resolution of the detector.

A few more detailed observations may be made from the χ^2 plots in fig. 7.1. From fig. 7.1 one can notice that the precision on θ_{23} when it is in the first octant ($\sin^2\theta_{23} < 0.5$) is slightly better than when it is in the second octant ($\sin^2\theta_{23} > 0.5$), even though the muon neutrino survival probability depends on $\sin^2 2\theta_{23}$ at the leading order. This asymmetry about $\sin^2\theta_{23} = 0.5$ stems mainly from the full three flavour analysis that we

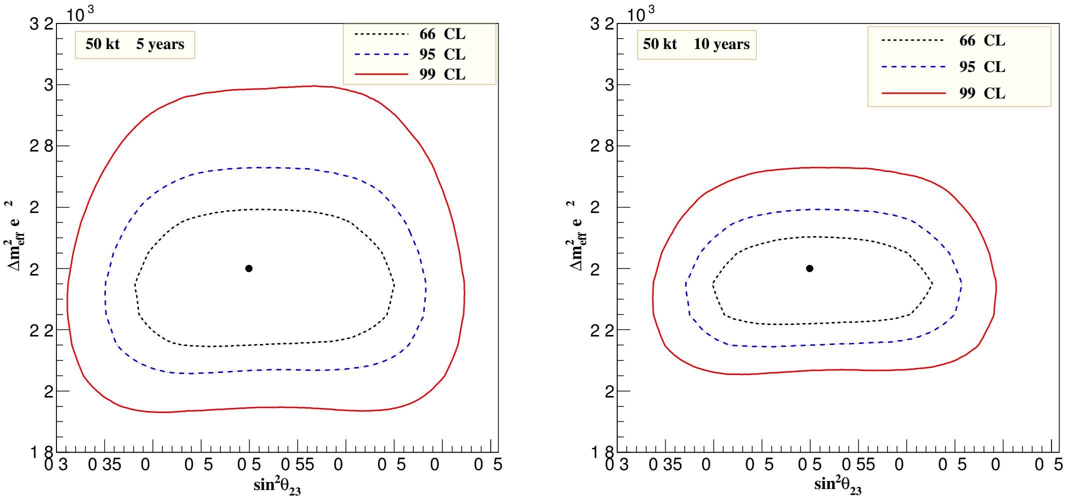

Figure 7.2: The precision reach expected at ICAL in the $\sin^2\theta_{23} - |\Delta m^2_{eff}|$ plane at various confidence levels. The black(broken), blue(dotted) and red(solid) lines show 68%, 90% and 99% C.L contours. The true values of $\sin^2\theta_{eff}$ and $|\Delta m^2_{eff}|$ used for generating data are shown by the black dots. The true values of other parameters used are given in Table 7.1. Panel (a) is for five-year running of the 50 kt detector while (b) is for ten years exposure.

have performed in this study. In particular, we have checked that the non-zero value of θ_{13} is responsible for the asymmetry observed in this figure. On the other hand, χ^2 asymmetry about the true value of $|\Delta m^2_{eff}|$ observed in Fig. 7.1 is an effect that is present even with a two flavour analysis.

The precisions obtainable at the ICAL for $\sin^2\theta_{23}$ and $|\Delta m^2_{eff}|$ are expected to be correlated. We therefore present the correlated reach of ICAL for these parameters in figs. 7.1 and 7.1. These are the main results of our analysis. As noted above, our three-neutrino analysis should be sensitive to the octant of θ_{23}. Therefore we choose to present our results in terms of $\sin^2\theta_{23}$ instead of $\sin^2 2\theta_{23}$. Though the constant-χ^2 contours still look rather symmetric about $\sin^2\theta_{23} = 0.5$, that is mainly due to the true value of $\sin^2\theta_{23}$ being taken to be 0.5. The values of $\sin^2\theta_{23}$ away from 0.5 would make the contours asymmetric and would give rise to some sensitivity to the octant of θ_{23}.

CHAPTER 8

SUMMARY AND CONCLUSION

In this thesis, we have discussed the simulation of ICAL detector for hadron shower reconstruction and analyzed in details the physics potential of INO using atmospheric neutrino as a source where we showed the expected sensitivity of ICAL in determining the mass hierarchy of neutrino and measurement of mixing angle θ_{23} and atmospheric mass square difference precisely.

Firstly, we described the proposed configuration of ICAL detector and then talked about the simulation of the detector using GEANT4 as a simulation tool. We calibrated the energy of hadron shower using fixed energy pions since the hadrons consist mainly of pions (about 85% of events on the average) along with other particles. The total number of events generated for each input pion energy is 10000 with randomized vertex position and directions. Hit distribution for each input energy was fitted with Gaussian function. Assuming linear dependence between pion energy and corresponding number of hits, we found the pion energy resolution as $\sqrt{\left(\frac{0.97}{\sqrt{E}}\right)^2 + (0.22)^2}$ in the energy range 1 - 15 GeV. It was seen that the fits to both π^- and π^+ yield virtually identical values for the fit parameters. It was also observed that the Gaussian distribution is not a good approximation at low energies, while, it approximates the hit distribution well at higher energies.

Next we described the simulation framework to study the physics potential of ICAL@INO using final state muon events. The atmospheric muon neutrino events before oscillations were simulated using the NUANCE based generator developed for ICAL@INO. To reduce Monte Carlo fluctuations, 1000 years of exposure was used for generating the events. Since it takes very long for the generator to produce such a large event sample, we simulated the atmospheric events using the generator just once for no oscillations and used a reweighting algorithm to obtain the oscillated event sample for any set of oscillation parameters. The oscillated muon event spectrum was then folded with the muon reconstruction efficiencies, charge identification efficiencies, energy resolution and the zenith angle resolution functions obtained from ICAL simulations performed by the INO collaboration. to obtain the reconstructed muon event spectrum in the detector. As ICAL is a magnetized calorimetric detector allowing an identification of μ^- and μ^+ events, it has an edge over rival atmospheric neutrino experiments. We defined a χ^2 function for Poissonian distribution for the errors in the ICAL@INO experiment taking into account systematic uncertainties expected in the experiment.

Next, we looked in detail at the prospects of determining the neutrino mass hierarchy with the data collected in the atmospheric neutrino experiment ICAL@INO. The data was generated for benchmark true values for the oscillation parameters and a given neutrino mass hierarchy and fitted with the wrong hierarchy. We showed the mass hierarchy sensitivity results with only ICAL@INO data for the analysis with fixed values of the oscillation parameters in the fit, as well as that obtained after marginalization over $|\Delta m^2_{\rm eff}|$, $\sin^2\theta_{23}$ and $\sin^2 2\theta_{13}$ in their current 3σ ranges. We showed these results as a function of the exposure in ICAL@INO. From a comparison of the two results, we showed that the mass hierarchy sensitivity with ICAL@INO data deteriorates with the uncertainty in the measured value of $|\Delta m^2_{\rm eff}|$, $\sin^2\theta_{23}$ and $\sin^2 2\theta_{13}$. These parameters will be rather accurately determined by the T2K, NOνA, Double Chooz, RENO and Daya Bay experiments. Since INO is expected to start operation after these have finished their full projected run, it is meaningful to include their effect in a combined statistical analysis for the neutrino mass hierarchy. In order to take that into account, we simulated the data for these experiments using GLoBES with the experimental specifications mentioned in their respective Letter Of Intent and/or Detailed Project Report. The results on mass hierarchy sensitivity from the combined analysis of data from ICAL@INO along with that from T2K, NOνA, Double Chooz, RENO and Daya Bay was shown for benchmark values of the oscillation parameters and full marginalization over all oscillation parameters in the fit for the wrong mass hierarchy. We showed that marginalization over δ_{CP} is practically unessential for the ICAL@INO data. However, for the accelerator data it is absolutely crucial to marginalize over δ_{CP} due to the very strong dependence of the hierarchy sensitivity on this parameter in these experiments. We then generated the data at all values of δ_{CP}(true) and showed that the mass hierarchy sensitivity of ICAL@INO was independent of δ_{CP}(true), however, the sensitivity of the combined NOνA, T2K and the reactor experiments depends very strongly on what δ_{CP}(true) has been chosen by Nature. For $\sin^2\theta_{23}(\text{true}) = 0.5$ and $\sin^2 2\theta_{13}(\text{true}) = 0.1$ the combined data of 10 years exposure in ICAL@INO along with T2K, NOνA and reactor experiments could rule out the wrong hierarchy with a statistical significance of 3σ to 4.2σ, depending on the chosen value of δ_{CP}(true). We also studied the effect of $\sin^2 2\theta_{13}$(true) and $\sin^2\theta_{23}$(true) on the reach of these combined projected data sets to determining the neutrino mass hierarchy. For $\delta_{CP}(\text{true}) = 0$, we showed that the statistical significance with which the wrong hierarchy could be ruled out by the global data set comprising of 10 years exposure in ICAL@INO along with T2K, NOνA and reactor experiments, could be anywhere between 2.13σ to 4.5σ depending on $\sin^2\theta_{23}$(true) and $\sin^2 2\theta_{13}$, where we allowed $\sin^2\theta_{23}$(true) to vary between $[0.4-0.6]$ and $\sin^2 2\theta_{13}$(true) between $[0.08-0.12]$. For the most favorable choice of δ_{CP}(true) $\simeq 270^\circ$ the sensitivity could go up to greater than 5σ with 10 years of ICAL@INO combined with data from T2K, NOνA and reactor experiments.

Next, we concentrated on improving the potential of atmospheric experiment in mass hierarchy measurement. We optimized the mass hierarchy sensitivity of the experiment with respect to the detector response functions and showed how using the hadron data as an independent input along with the muon data is most likely to give the best sensitivity to the neutrino mass hierarchy. We began with first discussing the earth matter effects in the muon neutrino survival probabilities which leads to the neutrino mass hierarchy sensitivity in this kind of experiment. We next showed how this sensitivity gets watered down when we consider the event rates in the detector (i) due to the inclusion of the appearance channel, (ii) due to the averaging effect of the charged current interaction which produces muons with any energy and angle allowed by the process, and (iii) with inclusion of detector resolutions. We showed how the mass hierarchy effect in the muon event sample, hadron event sample as well as the neutrino event sample decreases as we include these factors one by one. In the case of the muon and hadron spectrum, the major smearing of the earth matter effects come from the cross-section effect. The energy resolution brings about a further reduction in the signal, however the effect is mild. We showed that despite this reduction in the earth matter effects, both the muons as well as the hadrons event spectra have mass hierarchy sensitivity, which survives even after including all the resolution functions. The neutrino analysis is affected only due to the appearance channel and the detector resolutions. However, the neutrino events turned out to be very sensitive to the detector energy and zenith angle resolution. It was shown that the hierarchy effects reduce sharply as we switch on the neutrino energy and angle resolutions, such that the net earth matter effect present in the neutrino spectrum becomes comparable to that in the muon spectrum.

We performed a χ^2 analysis to quantify the reach of the experiment to measuring the neutrino mass hierarchy. We showed results for three different analysis.

- We started with the analysis of only the muon events using a treatment similar to that in chapter 4 but with flat efficiencies and resolution functions. Since the zenith angle resolution obtained from the simulations performed by the INO collaboration, is already very good, we fixed the zenith angle resolution for the muons at $\sigma_{\Theta_\mu} = 0.01$ in $\cos\Theta_\mu$ and showed how the mass hierarchy sensitivity could be improved by improving the muon energy resolution and muon reconstruction efficiency. If the muon energy resolution could be improved to 2%, we could get a more than 4σ measurement of the mass hierarchy from the 50×10 kton-year of muon data alone.

- We next included the hadron events as an additional input in the analysis along with the muon data. Since the detector is not expected to measure the hadron energy and angle as well as it can do for the muon and since we wanted to keep track of the particles coming from a given neutrino energy and angle, we tagged the hadron with their corresponding muon from the charged current interaction. Since the muon zenith angle is the best measured quantity we collect all hadrons in a given muon zenith angle bin. These hadrons are then binned in their energy and zenith angle. We defined a χ^2 function for the combined analysis of the hadron and muon events with the so-binned muon and hadron data. The results showed that the hadron events bring in a noticeable improvement in the final sensitivity of the experiment to the neutrino mass hierarchy by increasing the $\Delta\chi^2$ by up to 5. The combined muon and hadron analysis is projected to give a 4.5σ sensitivity from a 50×10 kton-year exposure, if one could achieve 2% energy resolution and 80% reconstruction efficiency in the muons.

- Finally we showed the mass hierarchy sensitivity expected from the analysis of the data in terms of the neutrino energy and angle. For the zenith angle resolution obtained by the MONOLITH collaboration, we showed the $\Delta\chi^2$ expected from the neutrino analysis as a function of the neutrino energy resolution. For the 20% energy resolution quoted by the MONOLITH collaboration, one would get a little over 3σ signal for the neutrino mass hierarchy, which is lower than what we got from the combined muon and hadron analysis. We argued that this happens because the neutrino channel is very sensitive to the detector resolution functions. Once the detector resolution functions are imposed, the net earth matter effects in the neutrino channel becomes equal to, or sometimes even less than, the residual earth matter effects in the muon spectrum. When we add the hadron spectrum to the muon data, the total χ^2 overshoots that expected from the neutrino analysis.

In conclusion, the neutrino mass hierarchy can be measured rather well from the observation of atmospheric neutrinos in magnetized iron calorimeters. The sensitivity can be significantly increased by improving the muon energy resolution of the detector. The addition of the hadron data into the analysis will improve the results even further, and return sensitivity reach which is better than what can be achieved from the neutrino analysis at these detectors. For $\sin^2 2\theta_{13} = 0.1$, $\sin^2\theta_{23} = 0.5$, a muon energy resolution of 2%, reconstruction efficiency of 80% and exposure of 50×10 kton-year, we could get up to 4.5σ signal for the mass hierarchy from combining the muon and hadron data. The signal will go up when the atmospheric data is combined with data from other existing experiments, particularly NOνA.

Next, we calculate the projected reach of the ICAL experiment at INO for precise determination of the atmospheric neutrino parameters. We present uncorrelated as well as correlated constraints on the value of $\sin^2\theta_{23}$ and $|\Delta m^2_{eff}|$ expected to be obtained after 5 years and 10 years of running of the 50 kt ICAL. We find that after 5 years of running of this experiment, the values of $\sin^2\theta_{23}$ and $|\Delta m^2_{eff}|$ may be determined at an accuracy of 20% and $|\Delta m^2_{eff}|$ to 5.4% at 1σ. With 10 years exposure, these numbers improve to 16% and 2.9% for $\sin^2\theta_{23}$ and $|\Delta m^2_{eff}|$, respectively. The sensitivities with the data at ICAL only are not expected to be better than what we already have, indeed some of the other experiments in the next decade may do much better. However the measurement at ICAL will be complementary and may be expected to contribute significantly towards the precision of parameters in a global fit.

This is the first study on the reach of ICAL@INO for precision of atmospheric neutrino parameters, using the complete detector simulation. Note that in this analysis we have used only the information on muon events. However, the ICAL atmospheric neutrino experiment will also record and measure the hadrons associated with the charged current interaction of the muon-type neutrinos. Inclusion of this data-set into the analysis is expected to provide energy and angle reconstruction of the neutrino. This could lead to an improved sensitivity of the detector to the oscillation parameters. The analysis including the hadrons along with the muons is a part of the ongoing effort of the INO-ICAL collaboration. In addition, the updates and improvements in the muon momentum reconstruction algorithm as well as the optimization of our analysis procedure are likely to improve the results presented in this thesis.

BIBLIOGRAPHY

[1] B. Pontecorvo, J.Exptl. Theoret. Phys. 33 (1957) 549 [Sov. Phys. JETP 6 (1958) 429].

[2] B. Pontecorvo, J.Exptl. Theoret. Phys. 34 (1958) 247 [Sov. Phys. JETP 7 (1958) 172].

[3] B. Cleveland, *et al.*, Astrophys. J. 496 (1998) 505

[4] V. Gavrin, *Results from the Russian American Gallium Experiment (SAGE)*, VIIIth International Conference on Topics in Astroparticle and Underground Physics (TAUP 2003), Seattle, September 5–9, 2003;
J.N. Abdurashitov *et al.*, J. Exp. Theoret. Phys. 95 (2002) 181;
the latest SAGE results were presented by C. Cattadori, *Results from Radiochemical Solar Neutrino Experiments*, XXIst International Conference on Neutrino Physics and Astrophysics (Neutrino 2004), Paris, June 14–19, 2004.

[5] E. Bellotti, *The Gallium Neutrino Observatory (GNO)*, VIIIth International Conference on Topics in Astroparticle and Underground Physics (TAUP 2003), Seattle, September 5–9, 2003;
M. Altmann *et al.*, Phys. Lett. B **490** (2000) 16;
W. Hampel *et al.*, Phys. Lett. B **447** (1999) 127

[6] Y. Ashie, *et al.*, Phys. Rev. D **71** 112005 (2005) ;
Y. Fukuda, *et al.*, Phys. Rev. Lett **81** (1998) 1562-1567

[7] Q.R. Ahmad *et al.*, Phys. Rev. Lett **87** (2001) 071301;
Q.R. Ahmad *et al.*, Phys. Rev. Lett **89** (2002) 011301;
S.N. Ahmed *et al.*, Phys. Rev. Lett **92** (2004) 181301;

[8] M. Apollonio *et al.* [CHOOZ Collaboration], Eur. Phys. J. C **27**, 331 (2003) [hep-ex/0301017].

[9] S. Abe *et al.* [KamLAND Collaboration], Phys. Rev. Lett. **100**, 221803 (2008) [arXiv:0801.4589 [hep-ex]].

[10] F. P. An *et al.* [DAYA-BAY Collaboration], Phys. Rev. Lett. **108**, 171803 (2012) [arXiv:1203.1669 [hep-ex]].

[11] J. K. Ahn *et al.* [RENO Collaboration], Phys. Rev. Lett. **108**, 191802 (2012) [arXiv:1204.0626 [hep-ex]].

[12] Y. Abe *et al.* [Double Chooz Collaboration], Phys. Rev. D **86**, 052008 (2012) [arXiv:1207.6632 [hep-ex]].

[13] M. H. Ahn *et al.* [K2K Collaboration], Phys. Rev. D **74**, 072003 (2006) [hep-ex/0606032].

[14] R. Wendell *et al.* [Super-Kamiokande Collaboration], Phys. Rev. D **81**, 092004 (2010) [arXiv:1002.3471 [hep-ex]].

[15] P. Adamson *et al.* [MINOS Collaboration], Phys. Rev. D **86**, 052007 (2012) [arXiv:1208.2915 [hep-ex]].

[16] K. Abe *et al.* [T2K Collaboration], Nucl. Instrum. Meth. A **659**, 106 (2011) [arXiv:1106.1238 [physics.ins-det]].

[17] Y. Fukuda *et al.* (Super-Kamiokande Collaboration), Nucl. Instrum. Meth. **A501** (2003) 418-462.

[18] Ambats, I. *et al.* [MINOS Collaboration], NUMI-L-337, FERMILAB-DESIGN-1998-02

[19] Y. Itow *et al.* [T2K Collaboration], hep-ex/0106019.

[20] D. S. Ayres *et al.* [NOvA Collaboration], hep-ex/0503053.

[21] F. Ardellier, I. Barabanov, J. C. Barriere, M. Bauer, L. B. Bezrukov, C. .Buck, C. Cattadori and B. Courty *et al.*, hep-ex/0405032.

[22] J. K. Ahn *et al.* [RENO Collaboration], arXiv:1003.1391 [hep-ex].

[23] X. Guo *et al.* [Daya-Bay Collaboration], hep-ex/0701029.

[24] B. Pontecorvo, Sov. Phys. JETP **26**, 984 (1968) [Zh. Eksp. Teor. Fiz. **53**, 1717 (1967)].

[25] Z. Maki, M. Nakagawa and S. Sakata, Prog. Theor. Phys. **28**, 870 (1962).

[26] L. Wolfenstein, Phys. Rev. D **17**, 2369 (1978); S. P. Mikheev and A. Y. Smirnov, Sov. J. Nucl. Phys. **42**, 913 (1985) [Yad. Fiz. **42**, 1441 (1985)]; S. P. Mikheev and A. Y. Smirnov, Nuovo Cim. C **9**, 17 (1986); V. D. Barger, K. Whisnant, S. Pakvasa and R. J. N. Phillips, Phys. Rev. D **22**, 2718 (1980).

[27] A. M. Dziewonski and D. L. Anderson, Phys. Earth Planet. Interiors **25**, 297 (1981); S. V. Panasyuk, Reference Earth Model (REM) webpage, http://cfauves5.harvrd.edu/lana/rem/index.html.

[28] G. L. Fogli, E. Lisi, A. Marrone, D. Montanino, A. Palazzo and A. M. Rotunno, Phys. Rev. D **86**, 013012 (2012) [arXiv:1205.5254 [hep-ph]].

[29] D. V. Forero, M. Tortola and J. W. F. Valle, Phys. Rev. D **86**, 073012 (2012) [arXiv:1205.4018 [hep-ph]].

[30] M. C. Gonzalez-Garcia, M. Maltoni, J. Salvado and T. Schwetz, arXiv:1209.3023 [hep-ph].

[31] G. L. Fogli, E. Lisi, A. Marrone, D. Montanino, A. Palazzo and A. M. Rotunno, Phys. Rev. D **86**, 013012 (2012) [arXiv:1205.5254 [hep-ph]].

[32] M. Yamaga et al., (BELLE collaboration), Nucl. Inst. and Meth. A456, 109 (2000).

[33] T. Tabarelli de Fatis [MONOLITH Collaboration], hep-ph/0106252; see also, N. Y. Agafonova *et al.* [MONOLITH Collaboration], “MONOLITH: A massive magnetized iron detector for neutrino oscillation studies,” LNGS-P26-2000.

[34] M. S. Athar *et al.* [INO Collaboration], “India-based Neutrino Observatory: Project Report. Volume I.,” INO-2006-01.

[35] Y. Abe *et al.* [DOUBLE-CHOOZ Collaboration], “Indication for the disappearance of reactor electron antineutrinos in the Double Chooz experiment,” Phys. Rev. Lett. **108**, 131801 (2012) [arXiv:1112.6353 [hep-ex]].

[36] See http://www.hecr.tifr.res.in/$\sim$ samuel/html/vice.html.

[37] S. Agostinelli *et al.* [GEANT4 Collaboration], “GEANT4: A Simulation toolkit,” Nucl. Instrum. Meth. A **506**, 250 (2003), http://geant4.cern.ch/.

[38] R. Brun, F. Rademakers and S. Panacek, “ROOT, an object oriented data analysis framework,” For updates and latest version, see http://root.cern.ch/.

[39] J. Allison, K. Amako, J. Apostolakis, H. Araujo, P. A. Dubois, M. Asai, G. Barrand and R. Capra *et al.*, IEEE Trans. Nucl. Sci. **53**, 270 (2006).

[40] V. M. Datar, S. Jena, S. D. Kalmani, N. K. Mondal, P. Nagaraj, L. V. Reddy, M. Saraf and B. Satyanarayana *et al.*, “Development of glass resistive plate chambers for INO experiment,” Nucl. Instrum. Meth. A **602**, 744 (2009).

[41] M. M. Devi, A. Ghosh, D. Kaur, L. S. Mohan, S. Choubey, A. Dighe, D. Indumathi and S. Kumar *et al.*, arXiv:1304.5115 [physics.ins-det].

[42] D. Casper, webpage: nuint.ps.uci.edu/nuance/default.htm

[43] D. Casper, Nucl. Phys. Proc. Suppl. **112**, 161 (2002) [hep-ph/0208030].

[44] M. Honda, T. Kajita, K. Kasahara and S. Midorikawa, Phys. Rev. D **70**, 043008 (2004) [astro-ph/0404457].

[45] M. S. Athar, M. Honda, T. Kajita, K. Kasahara and S. Midorikawa, arXiv:1210.5154 [hep-ph].

[46] D. Ishitsuka [for the Double Chooz Collaboration]; D. Dwyer [for the Daya Bay Collaboration]; S. B. Kim [for the RENO Collaboration]; Talks at *Neutrino 2012*, the XXV International Conference on Neutrino Physics and Astrophysics (Kyoto, Japan, 2012), website: neu2012.kek.jp

[47] Thomas Schwetz *et. al*, arXiv:1311.1822 [hep-ph]

[48] X. Qian *et. al*, arXiv:1210.3651 [hep-ph]

[49] Emilio Ciuffoli *et. al*, arXiv:1305.5150 [hep-ph]

[50] D. V. Forero, M. Tortola and J. W. F. Valle, arXiv:1205.4018 [hep-ph].

[51] H. Minakata, arXiv:1209.1690 [hep-ph].

[52] E. Fernandez-Martinez, talk at "What is ν?, INVISIBLES 12 and Alexei Smirnov Fest", GGI, Firenze, June, 2012.

[53] J. Bernabeu, S. Palomares-Ruiz, A. Perez and S. T. Petcov, Phys. Lett. B **531**, 90 (2002) [hep-ph/0110071].

[54] M. C. Gonzalez-Garcia and M. Maltoni, Eur. Phys. J. C **26**, 417 (2003) [hep-ph/0202218].

[55] J. Bernabeu, S. Palomares Ruiz and S. T. Petcov, Nucl. Phys. B **669**, 255 (2003) [hep-ph/0305152].

[56] O. L. G. Peres and A. Y. .Smirnov, Nucl. Phys. B **680**, 479 (2004) [hep-ph/0309312].

[57] S. Palomares-Ruiz and S. T. Petcov, Nucl. Phys. B **712**, 392 (2005) [hep-ph/0406096].

[58] D. Indumathi and M. V. N. Murthy, Phys. Rev. D **71**, 013001 (2005) [hep-ph/0407336].

[59] R. Gandhi, P. Ghoshal, S. Goswami, P. Mehta and S. U. Sankar, Phys. Rev. D **73**, 053001 (2006) [hep-ph/0411252].

[60] S. Choubey and P. Roy, Phys. Rev. D **73**, 013006 (2006) [hep-ph/0509197].

[61] S. T. Petcov and T. Schwetz, Nucl. Phys. B **740**, 1 (2006) [hep-ph/0511277].

[62] D. Indumathi, M. V. N. Murthy, G. Rajasekaran and N. Sinha, Phys. Rev. D **74**, 053004 (2006) [hep-ph/0603264].

[63] S. Choubey, Nucl. Phys. Proc. Suppl. **221**, 46 (2011) [hep-ph/0609182].

[64] E. K. Akhmedov, M. Maltoni and A. Y. .Smirnov, JHEP **0705**, 077 (2007) [hep-ph/0612285].

[65] R. Gandhi, P. Ghoshal, S. Goswami, P. Mehta, S. U. Sankar and S. Shalgar, Phys. Rev. D **76**, 073012 (2007) [arXiv:0707.1723 [hep-ph]].

[66] E. K. .Akhmedov, M. Maltoni and A. Y. .Smirnov, JHEP **0806**, 072 (2008) [arXiv:0804.1466 [hep-ph]].

[67] R. Gandhi, P. Ghoshal, S. Goswami and S. U. Sankar, Phys. Rev. D **78**, 073001 (2008) [arXiv:0807.2759 [hep-ph]].

[68] A. Samanta, Phys. Rev. D **81**, 037302 (2010) [arXiv:0907.3540 [hep-ph]].

[69] A. Samanta and A. Y. .Smirnov, JHEP **1107**, 048 (2011) [arXiv:1012.0360 [hep-ph]].

[70] M. C. Gonzalez-Garcia, M. Maltoni and J. Salvado, JHEP **1105**, 075 (2011) [arXiv:1103.4365 [hep-ph]].

[71] V. Barger, R. Gandhi, P. Ghoshal, S. Goswami, D. Marfatia, S. Prakash, S. K. Raut and S U. Sankar, Phys. Rev. Lett. **109**, 091801 (2012) [arXiv:1203.6012 [hep-ph]].

[72] M. Blennow and T. Schwetz, JHEP **1208**, 058 (2012) [arXiv:1203.3388 [hep-ph]].

[73] P. Huber, M. Lindner, T. Schwetz and W. Winter, JHEP **0911**, 044 (2009) [arXiv:0907.1896 [hep-ph]].

[74] R. Gandhi, P. Ghoshal, S. Goswami and S U. Sankar, Mod. Phys. Lett. A **25** (2010) 2255 [arXiv:0905.2382 [hep-ph]].

[75] H. Nunokawa, S. J. Parke and R. Zukanovich Funchal, Phys. Rev. D **72**, 013009 (2005) [hep-ph/0503283].

[76] P. Huber, J. Kopp, M. Lindner, M. Rolinec and W. Winter, Comput. Phys. Commun. **177**, 432 (2007) [hep-ph/0701187]; P. Huber, M. Lindner and W. Winter, Comput. Phys. Commun. **167**, 195 (2005) [hep-ph/0407333].

[77] S. Choubey, Talk at *Neutrino 2012*, the XXV International Conference on Neutrino Physics and Astrophysics (Kyoto, Japan, 2012), website: neu2012.kek.jp ; A. Dighe, Talk at *NuFact 2012* 14th International Workshop on Neutrino Factories, Super Beams and Beta Beams (Williamsburg, Virginia, USA, 2012), website: www.jlab.org/indico/conferenceDisplay.py?confId=0 ; S. Goswami, Talk at

NOW 2012 Neutrino Oscillation Workshop (Otranto, Lecce, Italy, 2012), website: www.ba.infn.it/ now/now2012/web-content/index.html

[78] MONOLITH Proposal, LNGS P26/2000, CERN/SPSC 2000-031, August 15, 2000.

[79] Q. Y. Liu and A. Y. .Smirnov, Nucl. Phys. B **524**, 505 (1998) [hep-ph/9712493]; Q. Y. Liu, S. P. Mikheyev and A. Y. .Smirnov, Phys. Lett. B **440**, 319 (1998) [hep-ph/9803415]; E. K. Akhmedov, Nucl. Phys. B **538**, 25 (1999) [hep-ph/9805272] E. K. Akhmedov, A. Dighe, P. Lipari and A. Y. Smirnov, Nucl. Phys. B **542**, 3 (1999) [hep-ph/9808270].

[80] M. Maris and S. T. Petcov, Phys. Rev. D **56**, 7444 (1997) [hep-ph/9705392]; Q. Y. Liu, M. Maris and S. T. Petcov, Phys. Rev. D **56**, 5991 (1997) [hep-ph/9702361]; S. T. Petcov, Phys. Lett. B **434**, 321 (1998) [hep-ph/9805262]; M. Chizhov, M. Maris and S. T. Petcov, hep-ph/9810501.

[81] M. Ambrosio, G. Bari, G. Bencivenni, A. Candela, A. Chiarini, F. Chignoli, M. De Deo and M. D'Incecco *et al.*, Nucl. Instrum. Meth. A **456**, 67 (2000).

[82] G. Bari, A. Candela, M. De Deo, M. D'Incecco, M. Garbini, P. Giusti, C. Gustavino and M. Lindozzi *et al.*, Nucl. Instrum. Meth. A **508**, 170 (2003).

[83] M. Blennow and T. Schwetz, arXiv:1306.3988 [hep-ph].

[84] V. D. Barger, K. Whisnant, S. Pakvasa and R. J. N. Phillips, Phys. Rev. D **22**, 2718 (1980).

[85] M. C. Gonzalez-Garcia and M. Maltoni, Phys. Rev. D **70**, 033010 (2004) [hep-ph/0404085].